CALCULATIONS OF TURBULENT REACTING FLOWS USING PDF METHODS

A Dissertation

Presented to the Faculty of the Graduate School

of Cornell University

in Partial Fulfillment of the Requirements for the Degree of

Doctor of Philosophy

by

David Henry Rowinski

January 2013

CALCULATIONS OF TURBULENT REACTING FLOWS USING PDF METHODS

David Henry Rowinski, Ph.D.

Cornell University 2013

This work presents applications of the probability density function (PDF) method to several recently-developed turbulent flows, and the implementation and assessment of several sub-models. A series of lean piloted premixed jet flames (in order of lowest to highest jet bulk velocity: PM1-50, PM1-100, PM1-150, and PM1-200) is first studied using a Reynolds-Averaged Navier-Stokes (RANS) based PDF method. These calculations use diagnostic testing and thorough parametric studies of models to show that the standard models overpredict the reaction rate in the flames PM1-150 and PM1-200. The nature of the combustion in these flames is examined through comparison to simpler combustion models, and it is found to be similar to laminar non-premixed flames. These same flames are then investigated further using both RANS-PDF and the recently developed Large Eddy Simulation (LES) PDF method. Simple models for molecular diffusion and combustion are tested and implemented in the RANS-PDF calculations. In the LES-PDF calculations, the effects of differential diffusion and the mixing model constant, C_M, are both examined, and the calculations are found to be very sensitive to the value of C_M. This study yields substantially improved calculations of all the flames. In particular, the study of C_M shows strong evidence that larger values of C_M are necessary for flames PM1-150 and PM1-200. The modeling of molecular mixing is investigated further through a study of a non-reacting turbulent jet flow with three inflowing

streams. This study presents the unique opportunity to compare the scalar dissipation rate and conditional diffusion from the calculations to experimental data. In the RANS-PDF calculations of this flow, three classic mixing models are evaluated. The joint scalar PDF's are very sensitive to the choice of mixing model and show a wide variability from the measurements. Only the Euclidean Minimum Spanning Tree (EMST) produces compositions which lie very close to the slow manifold identified in the experimental work. LES calculations of the same flow are performed, and the dissipation rate and conditional diffusion are calculated. The resolved scalar dissipation rate is found to be in good agreement with the experimental data, but depends strongly on the resolution; the total dissipation rate from the RANS-PDF and LES calculations indicates significantly larger scalar dissipation rates than those measured experimentally. Lastly, LES-PDF calculations of the same flow yield joint-PDF's in very good agreement with the experimental data, and are far-improved from those of any mixing model studied with RANS-PDF. The *attenuation of variance production* model is introduced for LES-PDF and tested in this flow. This new model results in an additional dissipation of scalar variance and yields calculations of improved accuracy on coarse grids.

BIOGRAPHICAL SKETCH

David Henry Rowinski was born in 1985 in Garfield Heights, Ohio. He attended the University of Notre Dame in Notre Dame, Indiana, on the Larkin Memorial Scholarship from 2003 to 2007. As an undergraduate, he undertook research in computer vision and genetic algorithms under the guidance of Profs. Steven Skaar and Mihir Sen. He was awarded the Rockwell Automation Design Award for the best Senior Design Project for his role in the development of an automated circuit board assembler; additionally he earned the Rev. Thomas Steiner Award for overall excellence in engineering. At the conclusion of his undergraduate education, he graduated with a B.S. in Mechanical Engineering and earned a National Defense Science and Engineering Graduate (NDSEG) Fellowship. Driven by his interest in energy systems and computational sciences, he then enrolled at Cornell University to commence his graduate studies.

David attended Cornell University in Ithaca, New York, as an NDSEG Fellow from 2007 to 2012. There, he was privileged to conduct research in the modeling of turbulent reactive flows under the guidance of Prof. Stephen Pope. As part of his research, he performed the first modeling studies of two challenging turbulent flows: a series of lean premixed turbulent jet flames, and a three-stream coaxial mixing jet. The two most memorial and enjoyable aspects of his research work were (i) the opportunity to work with some of the most sophisticated modeling capabilities, including the tool HPDF developed by Prof. Haifeng Wang and Prof. Stephen Pope, and (ii) the opportunity to participate in conferences together with the world's leading experts, including the international combustion meetings in Montreal and Beijing, and the national meetings in Ann Arbor and Atlanta. David received his M.S. in Mechanical Engineering in 2010, and he is earning his Ph.D. in Mechanical Engineering in 2013.

This document is dedicated to my parents, Dennis and Mary.

ACKNOWLEDGEMENTS

I first offer my sincere gratitude to my advisor, Prof. Stephen Pope, for taking on the challenge of advising my graduate education, and for teaching me how to grow as both a scholar and a person. The last five years at Cornell have been a challenging and rewarding time, and I owe any self-improvement I might have made during those years to his never-failing guidance.

I would like to thank the members of my special committee, Prof. David Bindel, Prof. Peter Diamessis, and Prof. David Caughey for shaping the course my research has taken, for challenging me during my examinations, for their helpful advice on both research problems and my thesis. I would also like to thank all of my former teachers, including Prof. Steven Skaar and Prof. Mihir Sen, for all their fortitude in instructing me, and for the passion for scientific research they instilled within me.

I also send a hearty thanks to my colleagues at the Turbulence and Combustion Group at Cornell, including Dr. Steve Lantz, Prof. Haifeng Wang, Dr. Konstantin Kemenov, Prof. Zhuyin Ren, and Varun Hiremath, for their contributions and ideas through research group meetings, and for all the times they helped me with research problems.

Lastly, I thank my family for their support and encouragement along every step of the exciting, challenging, and fulfilling journey my graduate studies have been. Most of all, I offer this thanks to my parents, Dennis and Mary, for their selfless gifts of life, a sound education, and faith.

TABLE OF CONTENTS

LIST OF TABLES

LIST OF FIGURES

CHAPTER 1

INTRODUCTION

1.1 Motivation

Two of the most serious problems the world faces today are (i) meeting the ever-growing demand for energy, and (ii) combatting environmental pollution and its many consequences, including global warming and climate change. These two challenges are strongly interconnected: more than 80% of the world's energy comes from fossil fuel combustion [1], which is a notorious source of pollutant emissions. While many revolutionary innovations in transportation and energy generation have arisen due to combustion technology, the world's dependence on these devices has led to many challenges in energy efficiency, air quality, global warning, and safety. Combustion research, one must recognize, is an integral part of solving these problems for the future.

In the past, combustion research has led to substantial improvements regarding both of these two problems. For example, in the automotive industry these improvements include the development of pollution-reducing and energy-saving technologies such as the catalytic converter, exhaust gas recirculation, direct fuel injection, ultra-lean fuel burning, and engine design optimization. Combustion research in other areas is providing more means by which to solve these two problems. Research in the development of biofuels and synthetic fuels shows potential in removing dependence on fossil fuels. The development of clean coal technology through carbon capture and sequestration is a promising means of reducing harmful pollutants, which can also be applied to fuel sources other than coal. So, while combustion certainly contributes to

the problems of depleting fuel sources and pollution, combustion research is an essential part of achieving the right solutions.

The particular type of combustion research of which this work is a part is the computationally-driven design of combustion devices. Design has traditionally been done in an *ad hoc* fashion using trial-and-error procedures in a laboratory setting. Computational design is advantageous over traditional design methods for several reasons, one of which is the potential for design optimization: design parameters can be chosen so that certain criteria, for example, fuel efficiency and pollutant concentrations, are optimized. Through this type of research, combustion devices can be designed to be as efficient, as reliable, and as clean as possible.

1.2 Methodologies

This type of computational design requires complete computational models of realistic combustion devices. Combustion devices, such as gas turbines, internal combustion engines, boilers, and furnaces, are indeed complex. The physical processes occurring in these devices often include the injection of a liquid fuel, atomization or liquid droplet formation, spray evaporation, gas-phase turbulent flow, intense chemical reaction with rapid changes in temperature and pressure, acoustic effects, and soot formation. While all of these processes are important, this study focuses solely on the primary driving process, gas-phase turbulent reactive flow.

1.2.1 Direct Numerical Simulation

Turbulent reactive flow is a process whose governing physics is generally well-understood. The transport equations are readily derived from a force balance and an energy balance, and the direct solution of these transport equations (Direct Numerical Simulation, or DNS) is one possible computational method. For example, we consider a Newtonian fluid whose state is determined by a velocity vector field $\mathbf{U}$ (whose i-th component is denoted by U_i), density field ρ, pressure field P, and a vector of n_ϕ reactive scalar composition variables ϕ (each denoted by ϕ_α). The governing equations for this flow are continuity,

$$\frac{\partial \rho}{\partial t} + \frac{\partial \rho U_j}{\partial x_j} = 0, \tag{1.1}$$

conservation of momentum,

$$\frac{\partial \rho U_i}{\partial t} + \frac{\partial \rho U_i U_j}{\partial x_j} = -\frac{\partial P}{\partial x_i} + 2\frac{\partial}{\partial x_j}\left(\rho\nu\left(S_{ij} - \frac{1}{3}S_{kk}\delta_{ij}\right)\right), \tag{1.2}$$

and conservation of each composition variable,

$$\frac{\partial \rho \phi_\alpha}{\partial t} + \frac{\partial \rho U_j \phi_\alpha}{\partial x_j} = \frac{\partial}{\partial x_j}\rho\Gamma\frac{\partial \phi_\alpha}{\partial x_j} + \rho S_\alpha(\phi), \tag{1.3}$$

along with an equation of state which relates the pressure, density, and composition (for example, the ideal gas equation). In this set of equations, ν is the kinematic viscosity, S_{ij} is the strain rate tensor ($2S_{ij}=\partial U_i/\partial x_j+\partial U_j/\partial x_i$), Γ is the diffusivity of the composition variable ϕ_α, and S_α is the reaction source term for ϕ_α. In DNS, this set of $5 + n_\phi$ equations is solved for the density, ρ, the three components of velocity, U_j, the pressure, P, and the n_ϕ composition variables, ϕ_α.

However, the application of DNS to turbulent combustion presents major computational challenges. Turbulent flows demonstrate a huge variety in

length scales, ranging from the length scale of the device (around 1 m) to the smallest turbulent scales (as small as 10^{-6}m), and an equally wide range of time scales. Due to the nature of combustion, the reaction source term S is stiff and highly non-linear. Furthermore, a large number of chemical species (between 10 and 1,000) is required to characterize sufficiently the composition. All of these complexities result in systems of many stiff, non-linear, coupled differential equations. The solution of these governing equations via DNS has restrictive computational requirements for the grid size and time step. Specifically, the computational work scales approximately with Re^3, where Re is the Reynolds number. For computationally tractable calculations of realistic flows, DNS is not practical and modeling is needed for the turbulence and chemistry.

1.2.2 Reynolds-Averaged Navier-Stokes methods

One group of widely-used methodologies for modeling the turbulence is Reynolds-Averaged Navier-Stokes (RANS). In RANS, each quantity is decomposed into two components: the ensemble mean and the fluctuating component. The general methodology is to solve the mean governing equations and to model the fluctuating components. Each component of the velocity is decomposed into $U_j = \langle U_j \rangle + U'_j$, where $\langle U_j \rangle$ is the ensemble mean and U'_j is the fluctuating component, and the scalar variables are decomposed analogously. By substituting these expressions into Eqs. 1.1–1.3, the RANS equations are obtained. For the case of constant-property flow, these are the mean continuity,

$$\frac{\partial \rho}{\partial t} + \frac{\partial \rho \langle U_j \rangle}{\partial x_j} = 0, \tag{1.4}$$

mean conservation of momentum,

$$\frac{\partial \rho \langle U_i \rangle}{\partial t} + \frac{\partial \rho \langle U_i \rangle \langle U_j \rangle}{\partial x_j} = -\frac{\partial \langle P \rangle}{\partial x_i} + 2\frac{\partial}{\partial x_j}\left(\rho\nu\left(\langle S_{ij} \rangle - \frac{1}{3}\langle S_{kk} \rangle \delta_{ij}\right)\right) - \frac{\partial}{\partial x_j}\left(\rho \langle U_i' U_j' \rangle\right), \quad (1.5)$$

and mean species conservation,

$$\frac{\partial \rho \langle \phi_\alpha \rangle}{\partial t} + \frac{\partial \rho \langle U_j \rangle \langle \phi_\alpha \rangle}{\partial x_j} = \rho\Gamma\frac{\partial^2 \langle \phi_\alpha \rangle}{\partial x_j \partial x_j} + \rho \langle S_\alpha(\phi) \rangle - \frac{\partial}{\partial x_j}\left(\rho \langle \phi_\alpha' U_j' \rangle\right), \quad (1.6)$$

equations.

The primary challenges of RANS-based approaches are to model the unclosed turbulent fluxes, $\langle U_i' U_j' \rangle$ and $\langle \phi_\alpha' U_j' \rangle$ and the mean reaction source term, $\langle S_\alpha(\phi) \rangle$. It is important to recognize that due to the highly non-linear nature of the reaction source term, $\langle S_\alpha(\phi) \rangle$ is very different from $S_\alpha(\langle \phi \rangle)$. The use of a pure RANS-based approach for turbulent combustion is therefore highly dependent on the model for this quantity.

1.2.3 Large Eddy Simulation

An alternative to RANS-based turbulence modeling is Large Eddy Simulation (LES). In LES, each quantity is decomposed into a resolved and a modeled component. The main idea of LES is to resolve the large-scale motions of the flow, while modeling the small-scale motions. Quantities such as momentum, mass, energy, and species are primarily transported by the large-scale structures of the flow, which are controlled largely by the details of the problem (such as boundary conditions and geometry). The small-scale features of the flow are more universal, so they can be modeled more readily.

The mass-weighted resolved component of the velocity, $\widetilde{U}_j$, and composition, $\widetilde{\phi}_\alpha$, and the volume-weighted density, $\bar{\rho}$, and pressure, $\bar{P}$, are all obtained

from the resolved transport equations, which are essentially the resolved components of Eqs. 1.1–1.3. These equations are the resolved continuity equation,

$$\frac{\partial \bar{\rho}}{\partial t} + \frac{\partial \bar{\rho} \widetilde{U}_j}{\partial x_j} = 0, \tag{1.7}$$

resolved conservation of momentum,

$$\frac{\partial \bar{\rho} \widetilde{U}_i}{\partial t} + \frac{\partial \bar{\rho} \widetilde{U}_i \widetilde{U}_j}{\partial x_j} = -\frac{\partial \bar{P}}{\partial x_i} + 2\frac{\partial}{\partial x_j}\left(\bar{\rho}\left(\widetilde{\nu} + \nu_T\right)\left(\widetilde{S}_{ij} - \frac{1}{3}\widetilde{S}_{kk}\delta_{ij}\right)\right), \tag{1.8}$$

and resolved transport of each composition variable,

$$\frac{\partial \bar{\rho} \widetilde{\phi}_\alpha}{\partial t} + \frac{\partial \bar{\rho} \widetilde{U}_j \widetilde{\phi}_\alpha}{\partial x_j} = \frac{\partial}{\partial x_j}\left(\bar{\rho}\left(\widetilde{\Gamma} + \Gamma_T\right)\frac{\partial \widetilde{\phi}_\alpha}{\partial x_j}\right) + \widetilde{S_\alpha(\phi)}. \tag{1.9}$$

In this system of equations, ν_T is the turbulent viscosity, $\widetilde{S}_{ij}$ is the resolved strain rate, and Γ_T is the turbulent diffusivity. The primary objective in LES is to develop robust models for ν_T and Γ_T to close this system of equations. Additionally, in reacting flows, a closure is also needed for the resolved reaction source term, $\widetilde{S_\alpha(\phi)}$.

1.2.4 PDF methods

It is clear from Eqs. 1.4–1.9 that both RANS and LES turbulence closures encounter modeling and numerical challenges when applied directly to turbulent combustion. First, the closure of the reaction source term is major problem, particularly due to the high non-linearity of this term in combustion. Second, the number of composition variables necessary to describe combustion may be very large, resulting in large, coupled systems of differential equations. The application of the Probability Density Function (PDF) method [2] to turbulent combustion is one method which can alleviate these difficulties.

In the PDF method, the single-point, joint probability density function of composition (or composition, velocity, and turbulence frequency, depending on which method is used) is derived from the Navier-Stokes equations. For example, for the case of the composition PDF method in constant-property flow, the transport equation for the joint PDF of compositions, f_ϕ, is

$$\frac{\partial f_\phi}{\partial t} + \frac{\partial}{\partial x_j}\left(f_\phi\left(U_j + \langle u_j|\underline{\psi}\rangle\right)\right) = -\frac{\partial}{\partial \psi_\alpha}\left(f_\phi\left(\langle \Gamma\nabla^2\phi_\alpha|\underline{\psi}\rangle + S_\alpha(\underline{\psi})\right)\right) \tag{1.10}$$

where U_j and u_j are the mean and fluctuating velocities, S_α is the reaction source term, Γ is the molecular diffusivity, and ψ_α is the sample-space variable corresponding to ϕ_α. The unclosed terms in the RANS or LES equations are then obtained by taking the appropriate moments of the joint PDF.

The PDF is solved using a Lagrangian Monte Carlo particle solver. Computational particles evolve due to convection, mixing, and reaction and provide a statistical solution to the PDF. The two principal advantages of the PDF method are that (i) the reaction source term appears in closed form and (ii) the Lagrangian Monte Particle method scales linearly with the number of dimensions of the PDF. Both of these features are advantageous for turbulent combustion, where the reaction source term is highly non-linear, and the number of composition variables can be large. Two disadvantages are that (i) the molecular diffusion term in Eq. 1.10, $\langle \Gamma\nabla^2\phi_\alpha|\underline{\psi}\rangle$, is unclosed and must be modeled, and (ii) the solution incurs statistical errors due to using a finite number of particles. An overview of three classical mixing models used in PDF methods is presented in Appendix A, and these models are an important topic addressed throughout this work.

1.3 Outline

In this work, we study the PDF method in conjunction with both RANS and LES through calculations of several novel flows. To ensure that the calculations are useful, all of the flow configurations studied here are based on recently developed flows from the Turbulent Non-premixed Flames (TNF) workshop, a collaborative effort between experimentalists and modelers. Each flow from the experiments at TNF is carefully devised to isolate certain physical processes. These processes include turbulent mixing and combustion phenomena such as extinction and re-ignition. Additionally, the collaboration through TNF ensures that the flows studied are accompanied by thorough experimental measurements and detailed descriptions of the boundary conditions.

In Chapter 2 (an article published in Combustion Theory and Modelling), we perform the first comprehensive modeling study of a series of lean, premixed turbulent flames. We validate the experimental data and perform a large set of sensitivity studies, to examine the sensitivity of the calculations to nearly every aspect of the modeling. We thoroughly assess the combustion events occurring in the calculations and make comparisons to simpler combustion models.

In Chapter 3 (an article submitted for publication to Combustion Theory and Modeling), we return to the same flames studied in Chapter 2. We approach them with a wide variety of new tools (including a model for the reduced description of the chemistry, as well as the LES-PDF modeling tool) and target the particular aspects of the modeling called into question in Chapter 2. We perform the first calculations of the flow PM1-150 from this series that yields improved agreement far downstream. An investigation of the constant mechanical-to-

scalar timescale ratio, C_M, provides strong evidence that in these turbulent premixed flames, a value of C_M significantly larger than that in other studies is needed.

As most of the difficulties in modeling the aforementioned flames are related to the modeling of molecular mixing, we focus the next study more deeply into this topic. In Chapter 4 (an article submitted for publication to Physics of Fluids), we present the first modeling study of a three-stream non-reacting jet flow from another recent experimental study. From this study, we extract detailed statistics from the calculations and for the first time can present comparisons to experimentally measured conditional diffusion. This last study gives a very detailed comparison of the current modeling and experimental capabilities, and introduces the *attenuation of variance production* model for LES-PDF methods. Lastly, in Chapter 5, conclusions are drawn from the studies presented here.

Two of the most important physical processes in turbulent reactive flows are turbulent mixing and chemical reaction. While the research presented in this work is largely motivated by applications to combustion (where both turbulent mixing and chemical reaction are critical), there are many other important problems in which either turbulent mixing or chemical reaction is very important. For example, in environmental flows, turbulent mixing is a critical driving process necessary for understanding transport of nutrients and sediment in rivers and lakes, as well as dispersion of pollutants in the atmosphere. Many of the same difficulties appear in these problems, including the wide variety of important length scales and time scales, so the research discussed here has applicability to these other communities as well.

CHAPTER 2

PDF CALCULATIONS OF PILOTED PREMIXED JET FLAMES

2.1 Introduction

The ability of the PDF method [2] to treat chemical reaction exactly has rendered it a useful tool for the prediction of finite-rate chemistry effects in turbulent flames. Past studies have shown the PDF method to be capable of calculating nonpremixed jet flames [3,4], including flames exhibiting combustion phenomena such as local extinction and reignition [5–9]. Similarly, the PDF method has successfully been applied to stoichiometric premixed planar flames [10] and jet flames [11]. In the current work, the PDF method is applied to a series of piloted premixed jet flames [12–14] which exhibit high turbulence levels, wide reaction zones, and extinction-reignition events, while based on a burner of simple geometry using a lean premixed fuel jet. While there exist other approaches specifically for modeling premixed flames, the PDF approach is not inherently limited to a particular mode of combustion.

Lean premixed combustion is of practical interest as a means of pollutant reduction. A prominent feature of lean premixed combustion is the low temperature at which combustion occurs. Consequently, there is decreased formation of pollutants such as NO_x, soot, and volatile organic compounds. However, operation at lean equivalence ratios also has the complication of increased tendency for extinction or blowoff, and the details of the combustion can be extremely sensitive to fuel composition [15]. For these reasons, a better understanding of the turbulence-chemistry interaction in this regime is critical.

The flames studied here are based on the Sydney piloted premixed jet burner (PPJB) [12]. The burner consists of a central jet of a lean methane-air premixture surrounded by a pilot of hot stoichiometric methane-air products. Outside the pilot stream is a hot coflow of lean hydrogen-air products. The stream configurations in the PPJB are summarized in Table 2.1. There is an additional coflow of ambient air around the hot coflow stream. However, additional calculations of the four-stream problem (shown in the supplemental material in Fig. SM-1, where Fig. SM-1 denotes Fig. 1 of the supplemental material) reveal that the entire flame lies well within the hot coflow of lean hydrogen products, and there is little difference when the additional air stream is not considered. Therefore, the air stream is neglected in these calculations. The problem is then reduced to a three stream problem. A mixture fraction is associated with each stream, and is defined to be a passive scalar that is unity at the composition of that stream, and zero at the composition of the other streams. The mixture fractions sum to unity, so there are only two independent mixture fractions. In practice, the mixture fractions are defined based on the elemental specific moles of H, O, and C.

Stream	D (mm)	U_b (m/s)	T (K)	ϕ	Composition
Jet	4	50-200	300	0.5	CH_4-air (unburnt)
Pilot	23.5	5.3	2280	1	CH_4-air (burnt)
Coflow	197	4.0	1500	0.43	H_2-air (burnt)

Table 2.1: Properties of the three concentric streams in the PPJB: D is diameter, U_b is jet bulk velocity, T is temperature, ϕ is equivalence ratio. The two flames considered, PM1-50 and PM1-200, have jet velocities of 50 m/s and 200 m/s, respectively.

Four flames are measured in [12], and the flames with the lowest and highest jet velocities, PM1-50 and PM1-200, are presented here. PM1-50 has a central jet with bulk velocity of 50 m/s and Reynolds number (Re) of 12,500 based on

the central jet. The configuration of PM1-200 is identical to that of PM1-50, except that the central jet bulk velocity is 200 m/s, yielding Reynolds number of 50,000. PM1-200 exhibits a decreased luminosity downstream from x/D of 15 to 45, where x is the axial coordinate and D=4 mm is the central jet diameter. This region is referred to here as an extinction region. Farther downstream, between x/D of 45 and 60, there is a small increase in luminosity, referred to here as a reignition region.

This work is outlined as follows: First, in Sec. 2, a brief description of the models and numerical methods used in the calculation is presented. In Sec. 3, the numerical and model parameters used in the calculations are stated, and the level of numerical accuracy is reported. In Sec. 4, results are presented for the base case, and the findings of a large number of sensitivity studies are summarized. The sensitivity of the flames to the chemical reaction timescale is shown, and the results are discussed in detail. Conclusions are drawn in Sec. 5 regarding the performance of the models and the nature of the combustion in these flames. Additionally, the supplemental material contains many more results than can be presented in this paper.

2.2 PDF Method

In the joint velocity-turbulence frequency-composition PDF method [16], the joint PDF of fluctuating velocity, turbulence frequency, and composition is solved by a particle-based Monte Carlo method. Particle velocities are modeled by the simplified Langevin model [17], and the timescale of turbulence is provided by a stochastic frequency model [18].

The particle composition evolves by mixing and reaction. In the base case, the EMST (Euclidean Minimum Spanning Tree) mixing model [19] is used to advance the particle composition due to mixing. A chemical mechanism dictates the reaction rates through which the particle composition advances due to chemical reaction; this step is performed in a computationally efficient way by using the ISAT (*In Situ* Adaptive Tabulation) algorithm [20, 21] to build a storage-retrieval table as the calculation progresses. The parallel algorithm of domain partitioning of particles [8] is used to facilitate efficient parallel computation.

The particle solver is coupled with a finite volume solver which solves the mean equations of mass, momentum, energy, and state [22–24]. The finite volume solver provides the particle solver with the mean velocity and pressure, while the particle solver provides the turbulence quantities and reaction source term to the finite volume solver. These models and solvers are the same used in many previous calculations [8, 9, 24] with the same model constants, excluding the turbulence model parameter $C_{\omega 1}$, as discussed later.

2.3 Calculation Details

2.3.1 Computational domain and boundary conditions

The solution domain is a rectangle represented in polar cylindrical coordinates. The origin corresponds to the center of the central jet at the jet exit plane. The domain extends $40D$ in the radial (r) direction and $100D$ in the axial (x) direction. The coflow boundary (r/D=40) is taken to be a perfect-slip wall, the centerline

(r/D=0) is axisymmetric, and at the outflow (x/D=100) the mean pressure is uniform.

At the inflow plane (x/D=0), the mean velocities are prescribed based on separate calculations using the commercial code FLUENT. The $k-\varepsilon$ model is used on a domain similar to that used for the joint-PDF calculations, but extending $100D$ upstream of the jet exit plane. The velocity profiles at the jet exit plane are extracted to represent the fully developed pipe flow of the jet and the entrainment of the pilot and coflow. The variances of velocity, $\langle u_x u_x \rangle$, $\langle u_r u_r \rangle$, and $\langle u_\theta u_\theta \rangle$, are approximated based on the turbulent kinetic energy, k, according to $\langle u_x u_x \rangle = k$ and $\langle u_r u_r \rangle = \langle u_\theta u_\theta \rangle = (1/2)k$. The velocity covariance, $\langle u_x u_r \rangle$, is prescribed based on the turbulent viscosity, ν_T, and the gradient of the mean axial velocity in the radial direction, $\partial \langle U_x \rangle / \partial r$, according to $\langle u_x u_r \rangle = -\nu_T \partial \langle U_x \rangle / \partial r$. The mean velocity profiles, the axial variance of velocity, and the velocity covariance are shown in Fig. 2.1 for the base case calculations of PM1-200.

The compositions are prescribed based on the experimental conditions given in Table 2.1, and the coflow and pilot are taken to be in chemical equilibrium. For the base case, the mean temperature profiles at the inlet are uniform for each stream. Additionally, the heat transfer between the hot coflow and the cold, pre-ignited pilot stream through the coflow-pilot wall is considered in subsequent calculations. The temperature profiles for these two cases are compared in Fig. 2.1 for the calculations of PM1-200.

It is emphasized that the FLUENT calculations are used solely to obtain these inflow boundary conditions for the PDF calculations. Furthermore, although some of the turbulence quantities are crudely approximated, it is found from sensitivity studies that the inlet conditions make little difference in the region of

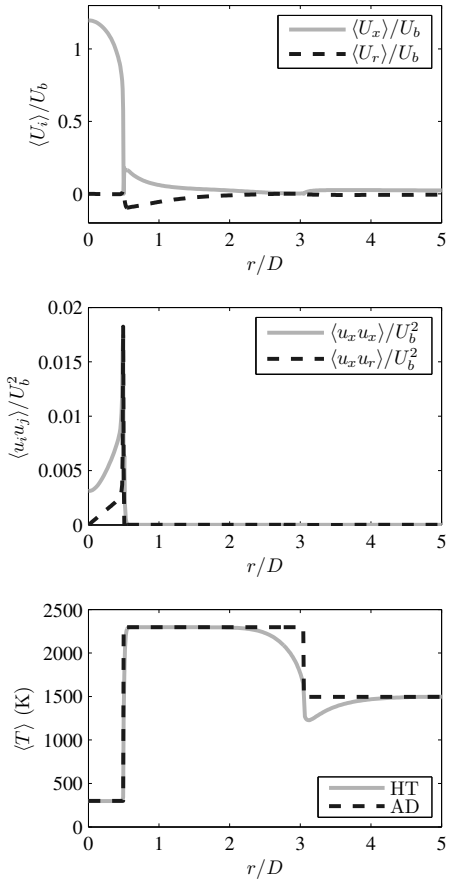

Figure 2.1: Inlet profiles from FLUENT calculations for flame PM1-200. The topmost plot shows the profiles at the inlet plane for mean axial velocity, $\langle U_x \rangle$, indicated by the solid line, and mean radial velocity, $\langle U_r \rangle$, indicated by the dashed line. Quantities are non-dimensionalized by the jet bulk velocity, U_b, and the jet diameter, D. The middle plot shows the inlet profiles of the axial variance of velocity, $\langle u_x u_x \rangle$, indicated by the solid line, and the covariance, $\langle u_x u_r \rangle$, indicated by the dashed line. The bottom plot shows the mean temperature profiles for the case considering heat transfer, indicated by the solid line, and for the adiabatic base case, indicated by the dashed line.

interest in these calculations, generally beyond 25 jet diameters downstream.

2.3.2 Base case

Numerical parameters

Numerical error is present in the calculations due to the finite number of cells in the axial and radial directions, N_x and N_r, particles per cell, N_{pc}, iterations of time averaging, N_{ta}, and due to the ISAT error tolerance, ϵ_{tol}, being greater than zero. In the base case, these parameters are taken to be: N_x=N_r=144, N_{pc}=50, N_{ta}=4000, and ϵ_{tol}=2×10^{-5}. The error in the calculations is examined through convergence studies of these four parameters in PM1-200. The reported error between two cases is defined as the maximum percentage difference relative to the peak value, at all investigated locations. The results of the convergence studies are summarized in Table 2.2, showing the maximum errors in mixture fractions ξ, temperature T, and mass fractions of major (CH_4,O_2,N_2,CO_2,H_2O) and minor (CO,OH) species, Y_{maj} and Y_{min}. In case A, the grid is refined from (N_x,N_r) of (144,144) to (192,192); in case B, N_{pc} is increased from 50 to 200; in case C, ϵ_{tol} is reduced from 2×10^{-5} to 1×10^{-5}; in case D, N_{ta} increases from 4000 to 8000. As may be seen, the only significant numerical error is due to the grid size (case A). This error is generally of order 5% for mean quantities and 10% for rms quantities, although slightly higher for minor species.

Model parameters

The value for the turbulence model parameter $C_{\omega 1}$, which controls the spreading rate of the jet, is determined from calculations of nonreacting flows on the same burner configuration. The value $C_{\omega 1}$=0.70 is chosen, and the agreement of velocity in the nonreacting flows is good. This value of $C_{\omega 1}$ is larger than the val-

	ξ		T		Y_{maj}		Y_{min}	
Case	ϵ_{mean}	ϵ_{rms}	ϵ_{mean}	ϵ_{rms}	ϵ_{mean}	ϵ_{rms}	ϵ_{mean}	ϵ_{rms}
A	4%	8%	4%	7%	7%	10%	8%	15%
B	1%	3%	1%	2%	1%	3%	2%	7%
C	1%	1%	1%	1%	1%	2%	1%	3%
D	1%	2%	1%	2%	1%	1%	2%	3%

Table 2.2: Results of numerical convergence tests. Shown are the maximum percentage changes (relative to the base case) in the mean and rms of various quantities for tests A, B, C, and D. In case A, the grid is refined from (N_x,N_r) of (144,144) to (192,192); in case B, N_{pc} is increased from 50 to 200; in case C, ϵ_{tol} is reduced from 2×10^{-5} to 1×10^{-5}; in case D, N_{ta} increases from 4000 to 8000.

ues of 0.65 used in [8, 9] and 0.56 in [6]. The EMST mixing model with a mixing constant, C_ϕ, of 1.5 is used for the base case, along with the ARM1 16-species reduced mechanism for methane [26]. This mixing model, value of C_ϕ, and mechanism have previously yielded successful calculations of nonpremixed jet flames [8].

2.4 Results and Discussion

2.4.1 Base case

A brief summary of the base case for both flames is provided first. Figure 2.2 shows profiles of scalar statistics for the base case calculations of PM1-50 at the two farthest downstream measurement locations, $x/D = 15$ and $x/D = 25$. The base case for PM1-50 is generally marked by good agreement in the mean and rms of all mixture fractions, fuel, oxidant, and products. Near the centerline at $x/D = 25$, there is a small region where the reaction progress is overpredicted.

One shortcoming is an inaccurate calculation of the initial mixing between the pilot and coflow. This can be observed both in the faster spreading of the temperature profile in the calculations and also in the larger variances produced between the pilot and the coflow in the calculations. These discrepancies are observed at x/D = 15 and further upstream. However, sensitivity studies show that the inlet conditions make little difference beyond x/D=25 in PM1-50, and far less difference in PM1-200. Scatter plots of the radicals CO and OH (shown in the supplemental material, Fig. SM-5) as a function of equivalence ratio, ϕ, suggest that most reaction occurs around ϕ of 0.6 to 0.7. This range of equivalence ratios is slightly richer than than central jet, where ϕ is 0.5, suggesting that in general the combustion occurring in this flame is sustained by richer mixtures.

The base case for PM1-200 is markedly different. Figure 2.3 shows the scalar statistics in the base case calculations of PM1-200 at the two farthest downstream measurement locations, x/D = 30 and x/D = 45. While all mean and rms mixture fractions show good agreement, the fuel and oxidant are drastically underpredicted while the products and temperature are overpredicted downstream. These calculations involve three streams, namely the jet, pilot, and coflow. A mixture fraction is associated with each stream and is evaluated in the calculations. It is important to note that the mean and rms of all three mixture fractions is generally well-predicted, so that the observed differences are not caused by inaccurate calculations of the mixing but rather by the overprediction of the progress of the reaction. To examine the influence of model parameters on this discrepancy, sensitivity studies are conducted.

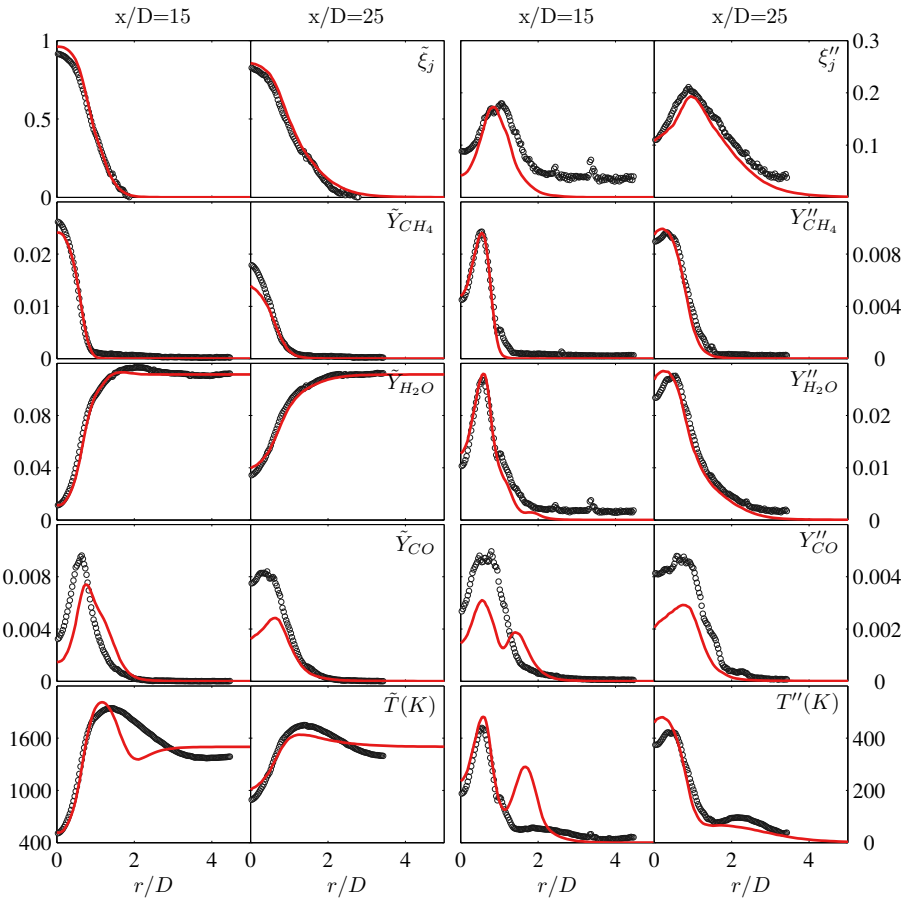

Figure 2.2: Radial profiles of Favre mean and rms mass fractions (Y) and temperature (T) for the base case of PM1-50 at $x/D = 15$ and $x/D = 25$. Open circles are measurements, solid lines are the base case calculations.

2.4.2 Sensitivity studies

An extensive set of sensitivity studies is performed on PM1-200. The details of these studies are provided in the supplemental material in Figs. SM-24-62. These studies are summarized here. Several inlet velocity profiles are compared (Figs. SM-24-26), including velocity profiles generated from FLUENT calculations of varying geometric detail, and profiles of simple plug flows and fully developed pipe flows. A wide range of pilot temperatures (2230 K-2330 K) is

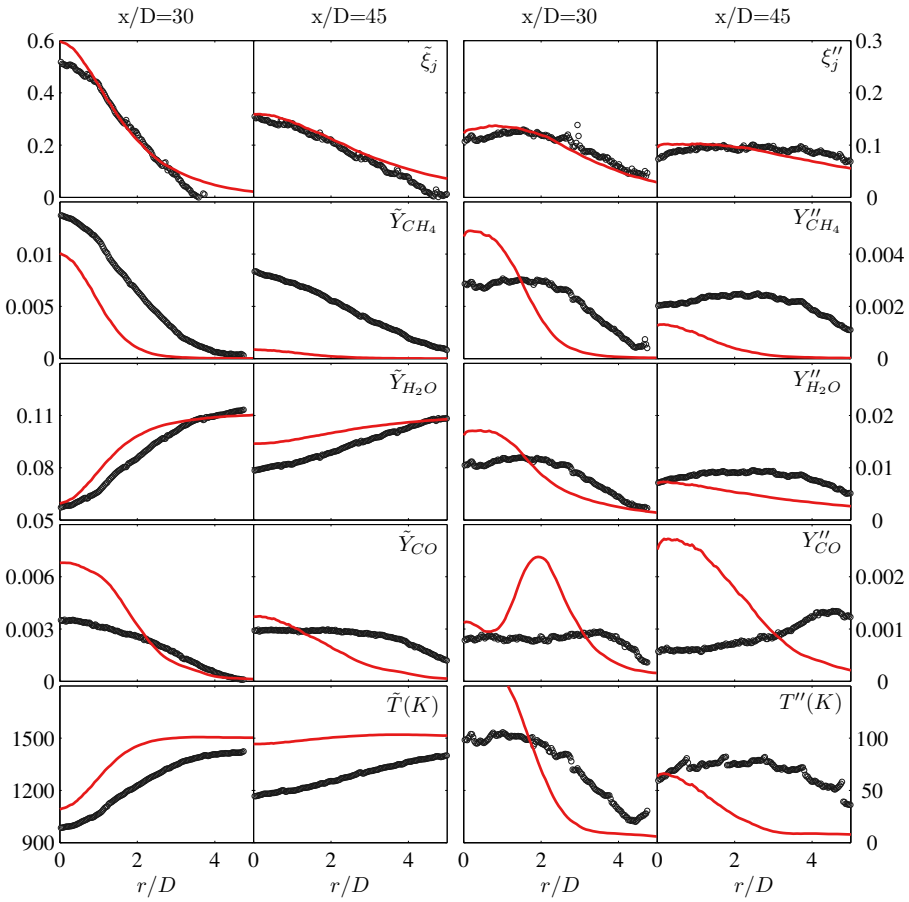

Figure 2.3: Radial profiles of Favre mean and rms mass fractions (Y) and temperature (T) for the base case of PM1-200 at $x/D = 30$ and $x/D = 45$. Open circles are measurements, solid lines are the base case calculations.

examined (Figs. SM-27-29). The heat loss from the coflow to the unreacted pilot stream is investigated by modeling the heat transfer in the FLUENT calculations for the inlet profiles. Overall, the effect of all these inflow conditions on the level of reaction downstream is small.

The model parameters are also investigated in the sensitivity studies. The value of $C_{\omega 1}$ is varied between 0.65 and 0.75 (Figs. SM-33-35). A wide range of values of C_ϕ (1-12) is investigated with the base case EMST mixing model (Figs. SM-36-41), in addition to the modified Curl (MC) [27,28] and interaction-

by-exchange-with-the-mean (IEM) [29,30] mixing models (Figs. SM-42-53). The influence of the chemical mechanism is studied (Figs. SM-54-59) with mechanisms ranging from a 5-step reduced mechanism [26] to the detailed GRI3.0 mechanism [31].

A wide range of coflow temperatures from 1200 K to 1500 K is investigated with two different chemical mechanisms, namely ARM-1 from the base case, and the UCSD mechanism [32]. Shown in Fig. 2.4 is the mean fuel mass fraction at x/D=45 on the centerline, normalized by the fuel mass fraction in the jet. Though there is some sensitivity to the reaction progress with the coflow temperature, no temperature in the studied range can adequately predict the reaction progress. Also, there is little difference between both of these chemical mechanisms throughout this coflow temperature range.

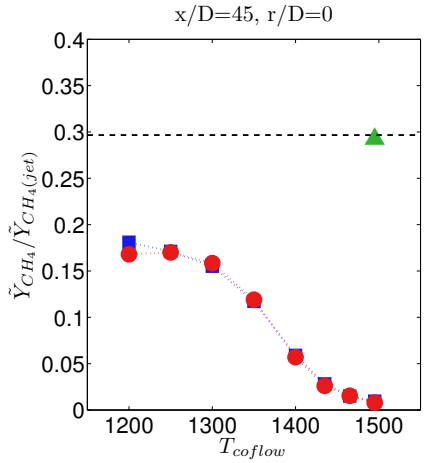

Figure 2.4: Mean fuel mass fraction normalized by the fuel mass fraction of the jet, at x/D=45 on the centerline as a function of coflow temperature in calculations of PM1-200. Squares indicate the ARM-1 mechanism, and circles indicate the UCSD mechanism. The triangle corresponds to the inert case. The experimental measurement is shown as the dashed line.

In conclusion, these sensitivity studies reveal that none of the investigated parameters yields accurate calculations of the observed reaction progress in

PM1-200; therefore, diagnostic calculations are next performed to determine if the reaction rates are in fact overpredicted.

2.4.3 Diagnostic tests on the chemical reaction timescale

Additional diagnostic calculations of PM1-50 and PM1-200 are performed in which all chemical reaction rates are attenuated by a constant factor f_R. Thus, f_R=1 corresponds to no modification; f_R=0 corresponds to inert mixing; and the values f_R=0.1,0.2,and 0.5 are also investigated. It is not suggested that the reaction mechanism has an uncertainty of 10 (as implied by f_R=0.1). Instead, these calculations are performed as a way to shed light on the observed discrepancies.

Scalar fields for PM1-50 are shown in Fig. 2.5 for three values of f_R at x/D=15 and x/D=25. There are three principle observations from this figure. First, the base f_R=1 displays good agreement for mean and rms jet mixture fraction, and good agreement for major species and temperature with the exception of the small region near the centerline. Second, slowing down the chemistry by a factor of five (f_R=0.2) has minor consequences in this flame; the major species are not much changed, and only the minor species such as CO show significant sensitivity to f_R. Third, the inert case (f_R=0) clearly overpredicts the amount of fuel and underpredicts the amount of products and the temperature downstream, and therefore this provides evidence that reaction levels are significant in PM1-50. Comparison to the inert case also demonstrates the effect of the heat release from reaction to the temperature field. In the unperturbed case, the temperature field can be around 500 K greater than that of the inert case, suggesting that there is sizable impact of the reaction to the temperature field.

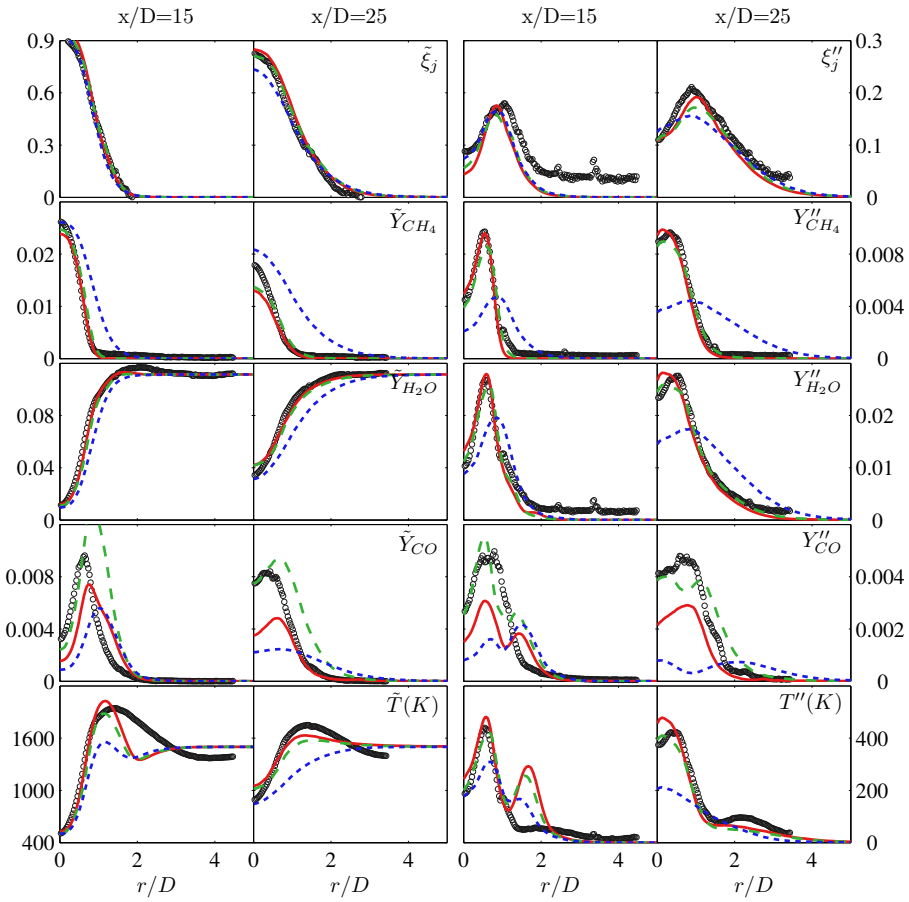

Figure 2.5: Radial profiles of Favre mean and rms mass fractions (Y) and temperature (T) in PM1-50 at x/D = 15 and x/D = 25. Open circles are measurements, lines are calculations for different values of f_R: solid (red), f_R=1, unperturbed; dashed (green), f_R=0.2, attenuated; dotted (blue), f_R=0, inert.

Results for PM1-200 using the same three values of f_R are presented at x/D=30 and x/D=45 in Fig. 2.6. The base case demonstrates good predictions of mean and rms mixture fractions, but drastically underpredicts fuel and overpredicts products and temperature. Unlike PM1-50, PM1-200 is sensitive to the value of f_R; there are significant differences when the reaction rates are slowed by a factor of five (f_R=0.2). In this case, the fuel levels are still slightly underpredicted, but are improved from the base case. Similarly, the product levels and

temperature show improvement. The *CO* levels in the slowed chemistry case show good agreement at this location. The inert case yields the best predictions of mean and rms for major species and temperature at this location. Inevitably, in the inert case, the *CO* levels are not predicted. A very important conclusion from this diagnostic test is that the inert case provides strong evidence that the amount of reaction occurring in PM1-200 is small, compared to both that in PM1-50 and that in the base case calculations of PM1-200.

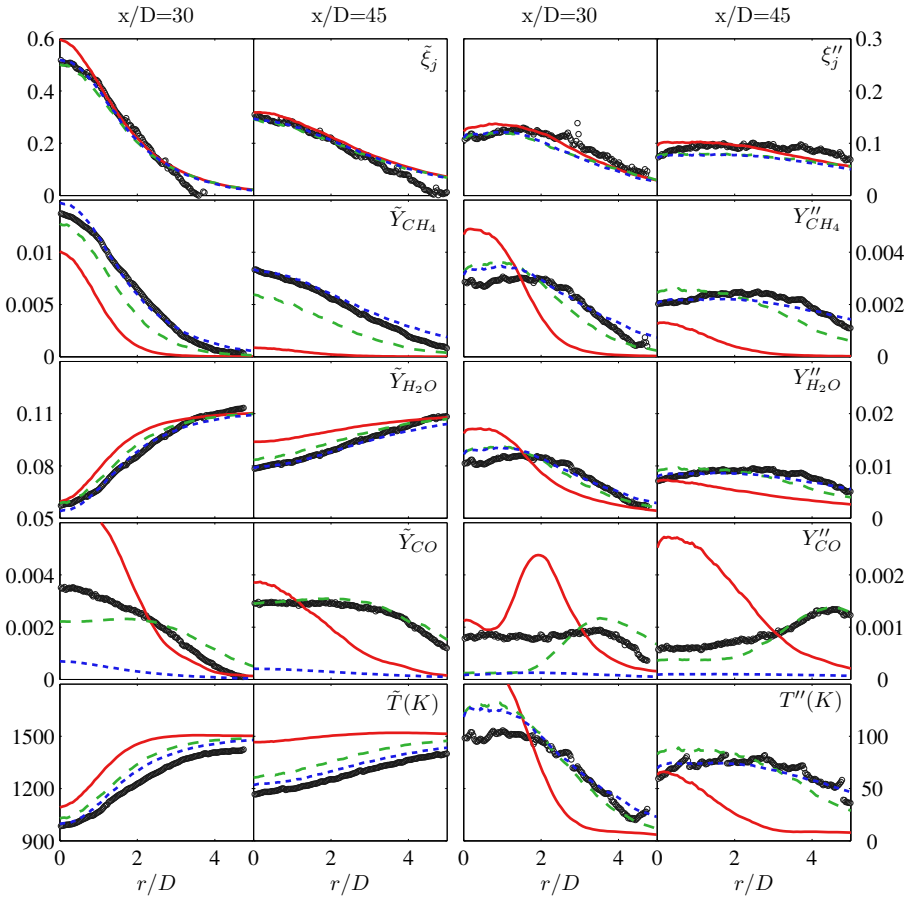

Figure 2.6: Radial profiles of Favre mean and rms mass fractions (Y) and temperature (T) in PM1-200 at $x/D = 30$ and $x/D = 45$. Open circles are measurements, lines are calculations for different values of f_R: solid (red), f_R=1, unperturbed; dashed (green), f_R=0.2, attenuated; dotted (blue), f_R=0, inert.

2.4.4 Analysis of finite-rate chemistry effects

Laminar flame calculations

The nature of the combustion in these flames is examined through the behavior of the minor species CO and OH as functions of temperature. First, simpler laminar flames are analyzed at conditions similar to those in the PPJB. Two primary laminar flames are considered: an opposed flow flame of the jet and the pilot compositions and an opposed flow flame of the jet and the coflow compositions. All of the following calculations are performed using the commercial software CHEMKIN 4.1 with the 53-species GRI3.0 [31] chemical mechanism. In the results presented, the mixture-averaged formulation is used for the evaluation of transport properties and thermal diffusion is accounted for. The evaluation of transport properties by the mixture-averaged formulation has been compared to that by the full multicomponent formulation, and the difference has been found to be negligible at this level of comparison.

In regions where the jet is heavily shielded by the pilot (i.e., near the inlet plane), the influence of the coflow stream is small and the combustion is dominated by the pilot and the jet. This region is analyzed by considering the opposed flow of two streams, denoted A and B, with velocities v_A and v_B, separated by a distance d. The composition of stream A is taken to be the jet composition, and the composition of stream B is taken to be the pilot composition. The stream compositions are those of the pilot and jet, as indicated by Table 2.1.

The imposed strain rate, a, is defined by $a = (v_A + v_B)/(d \times g)$, where g is a factor determining relative time scales of the chemistry and the flow. A large number of calculations spanning a broad range of values of a is presented in

Fig. 2.7, showing the primary quantity of interest, the CO mole fraction, X_{CO} versus temperature. In the cases of extremely high strain rate, the chemical time scale is much slower than the flow time scale, and thus no reaction takes place. The values of X_{CO} in this case lie on the mixing line between streams A and B. On the other extreme of very low strain rate, the jet mixture reacts with little or no mixing, and mixing then proceeds between the two reacted compositions. The behavior in between these extremes is nontrivial, and there exists a strain rate at which the peak X_{CO} is maximized over all strain rates. The reaction moves to higher T as a increases.

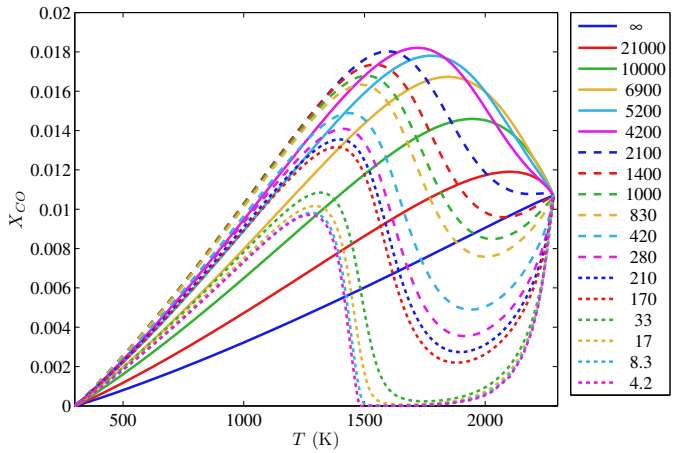

Figure 2.7: Mole fraction of CO versus temperature for laminar opposed flow flames of the jet and pilot compositions. The imposed strain rate, a, for each calculation is indicated in the legend in units of s^{-1}.

In regions where the presence of the pilot is insignificant (i.e., far downstream of the inlet plane), the combustion is dominated by the coflow and the jet. This case is examined by considering the opposed flow of two streams, A and B, where the composition of stream A is taken to be the jet composition, and the composition of stream B is taken to be the coflow composition. The stream compositions are those of the jet and the coflow from Table 2.1.

The values of X_{CO} versus temperature of the jet-coflow flames are shown in Fig. 2.8 for a large range of imposed strain rates. In this case, the limit of high strain rates bring the X_{CO} to zero since there is no CO present initially in either stream. Unlike the pilot-jet laminar flames, the peak X_{CO} occurs near the limit of very low strain rate in the jet-coflow flames.

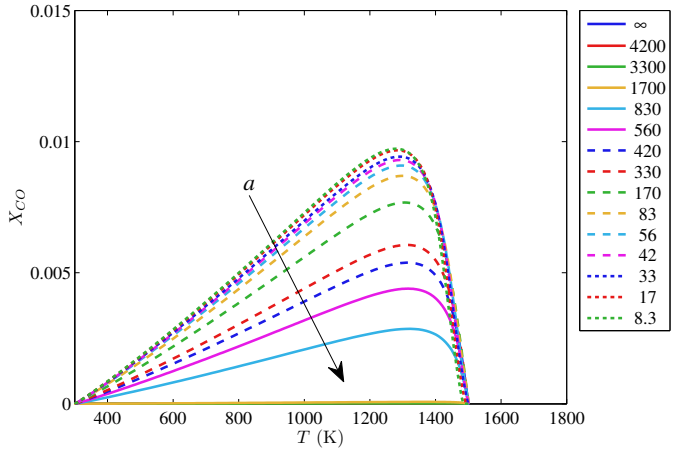

Figure 2.8: Mole fraction of CO versus temperature for laminar opposed flow flames of the jet and coflow compositions. The imposed strain rate, a, for each calculation is indicated in the legend in units of s^{-1}, and the arrow indicates the direction of increasing a.

In the PDF calculations, the overprediction of reaction progress is primarily confined to the jet-coflow region. For this reason, the laminar jet-coflow flames are studied in greater detail. The extinction behavior for these flames is shown in Fig. 2.9 through the quantity $\max\{T^\star\}$, where $T^\star(x) = T(x) - T_{mix}(x)$ and $T_{mix}(x)$ is the temperature in the case of inert mixing between the streams. Several chemical mechanisms are evaluated, including USC-mech-II [33], GRI3.0 [31], DRM-22 [34], the UCSD mechanism [32], and a skeletal C_1 mechanism used by Correa [35, 36]. For all mechanisms, except possibly for that of Correa, there is no sharp extinction.

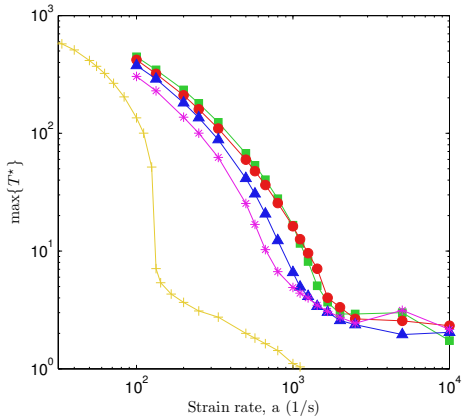

Figure 2.9: The quantity $max\{T^\star\}$ as a function of imposed strain rate in laminar jet-coflow flames for different chemical mechanisms. The quantity $T^\star(x)$ is defined as $T^\star(x) = T(x) - T_{mix}(x)$ where $T_{mix}(x)$ is the temperature in the case of inert mixing between the streams. The chemical mechanisms are represented by the following symbols: squares are USC-mech-II; circles are GRI3.0; triangles are DRM-22; asterisks are UCSD; plus signs are Correa.

This extinction behavior is consistent with that mentioned in [37]. For a flame of premixed reactants against hot products, there is a critical temperature of the hot products above which there is no sharp extinction. Instead of the usual S-shaped curve with a definite extinction strain rate, the curve is monotonic and there is no definite extinction strain rate.

It is noted that the only mechanism that is appreciably slower in the laminar flame calculations is that of Correa. In the PDF sensitivity studies (Figs. SM-54-59), this mechanism yields slightly less fuel consumption; however, even for this mechanism the reaction progress is largely overpredicted. Thus, the laminar jet-coflow flames do show a variation with chemical mechanism that is consistent with what is observed in the PDF calculation sensitivity studies. However, in order for the chemical mechanism to be the sole cause of the discrepancy in reaction progress, the behavior of the corresponding jet-coflow flames would

most likely be radically different, with extinction strain rates even less than that of the Correa mechanism.

Predictions of CO and OH in turbulent flames

A comparison is now made between the laminar flame calculations and the PDF calculations in terms of the radicals CO and OH. Shown in Fig. 2.10 are scatter plots of CO mole fraction, X_{CO}, versus temperature at two axial locations for PM1-50. The particles shown in these figures are those whose radial location is between the centerline and the half-width based on the mean jet mixture fraction. In the calculations at x/D=7.5, the ensemble mean coflow mixture fraction, $\langle \xi_c \rangle$, is very small, indicating that fluid originates primarily from the jet and pilot. As in [13], it is observed that X_{CO} conditioned on temperature, $\langle X_{CO}|T \rangle$, resembles that in a laminar opposed flow flame of the jet and the pilot compositions. Such a calculation with an imposed strain rate, a, of 1000 s^{-1} is found to match both measured and calculated $\langle X_{CO}|T \rangle$ at x/D=7.5.

The CO versus T behavior for both the calculations and the experiments of PM1-50 shares some common features with that in the stratified flames, particularly the flame fnh6, studied in [38]. Here, in PM1-50, the lean (equivalence ratio of 0.5) methane-air jet interacts with the stoichiometric methane-air pilot. The flame fnh6 consists of a stratification of methane-air ranging in equivalence ratio from 0.37 to 1.10. In the CO versus T behavior in both flames, there is an intermediate temperature range at which the CO mole fractions peak. In fnh6, however, the peak CO mole fractions observed are generally larger, possibly a result of the richer equivalence ratio conditions.

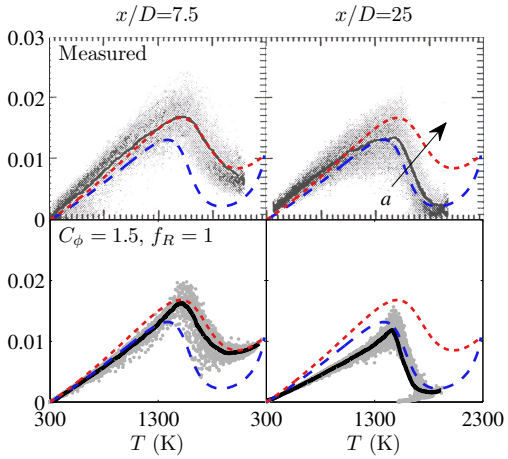

Figure 2.10: Mole fraction of CO versus temperature in PM1-50. Left plots, x/D=7.5; right plots, x/D=25; top plots, experiments; bottom plots, PDF calculations (base case). Solid line is the conditional mean, and other lines are laminar jet-pilot flames of imposed strain rate: dashed (blue), $a = 160\ s^{-1}$; dotted (red), $a = 1000\ s^{-1}$. The arrow indicates the direction of increasing a.

At x/D=25 in PM1-50, $\langle \xi_c \rangle$ is still small at 0.1, and a laminar opposed flow flame of the jet and pilot at $a = 160\ s^{-1}$ corresponds well with the observed $\langle X_{CO}|T \rangle$. The decreasing strain rate in the laminar calculations is consistent with the idea that the scalar dissipation rate of an conserved passive scalar is generally decreasing downstream in this flame, considering the approximate proportionality between strain rate and scalar dissipation rate. The agreement between the measurements, PDF calculations, and laminar calculations suggests that the scalar dissipation rate implied by the mixing model may be reasonable in the base case calculations of PM1-50.

Scatter plots of X_{CO} versus temperature for PM1-200 are shown in Fig. 2.11. In PM1-200, the ensemble mean pilot mixture fraction is small (0.07 at x/D=15 and yet smaller at x/D=45). This shows that the fluid is dominantly from the jet and coflow, and hence, comparisons are made with laminar opposed flow

flames of these two streams. Note that here (PM1-200, Fig. 2.11), the two relevant streams are the jet and the coflow; whereas for PM1-50 (Fig. 2.10), they are the jet and the pilot.

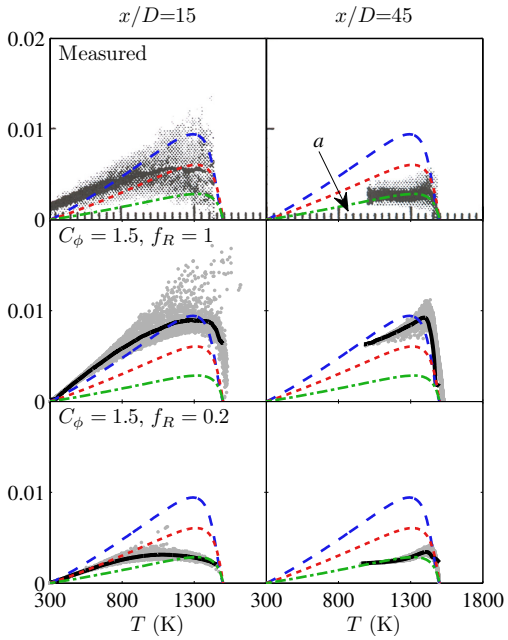

Figure 2.11: Mole fraction of CO versus temperature in PM1-200. Left plots, x/D=15; right plots, x/D=45; top row, experiments; bottom rows, PDF calculations (middle row, base case; bottom row, attenuated); Solid line is the conditional mean, and other lines are laminar jet-coflow flames of imposed strain rate: dashed (blue), $a = 30\ s^{-1}$; dotted (red), $a = 330\ s^{-1}$; dashed-dotted (green), $a = 830\ s^{-1}$. The arrow indicates the direction of increasing a.

In general, the $\langle X_{CO}|T \rangle$ in PM1-200 (Fig. 2.11) is lower than that in PM1-50 (Fig. 2.10) as a result of both the extent of the pilot stream influence and the difference in the scalar dissipation rates between the two flames. Unlike PM1-50, PM1-200 contains few particles above a temperature of 1500 K, providing further evidence of small pilot presence at these locations.

The measured $\langle X_{CO}|T \rangle$ resembles that in a laminar flame at $a = 330\ s^{-1}$ at

x/D=15, and a = 830 s^{-1} at x/D=45. The base case PDF calculations overpredict $\langle X_{CO}|T\rangle$ by a factor of two compared to the measurements. The values of $\langle X_{CO}|T\rangle$ in the base case are similar to those in a laminar flame of much lower strain rate, about 30 s^{-1}, which may suggest that the scalar dissipation rate implied by the mixing model is underpredicted in the base case.

Figure 2.11 also shows the calculations with f_R of 0.2. In these calculations, $\langle X_{CO}|T\rangle$ appears well predicted, particularly at x/D=45. This artificial modification to the chemical reaction timescale alters $\langle X_{CO}|T\rangle$ in a way different than any value of C_ϕ or mixing model does (Figs. SM-36-53). The values of $\langle X_{CO}|T\rangle$ measured and computed with f_R=0.2 are consistent with a laminar calculation of strain rate about ten times greater than that in the laminar calculation consistent with the base case. Because the scalar dissipation rate is primarily controlled by the mixing model, these observations suggest that it is the mixing models which perform inadequately at the conditions of PM1-200.

The product of CO and OH mole fractions, $X_{CO}X_{OH}$, serves as an indicator of a general product formation rate as in [12, 13], assuming that most of the CO_2 is formed from the reaction $CO + OH \rightarrow CO_2 + H$. In Fig. 2.12, scatter plots of X_{CO}, X_{OH}, and $X_{CO}X_{OH}$ are shown from the base case calculations of PM1-50 and compared to the measurements. It is observed as before that the X_{CO} is generally well-predicted as a function of temperature for this flame, and the trend in peak $\langle X_{CO}|T\rangle$ decreasing downstream is represented well in the calculations. The calculations of X_{OH} are slightly overpredicted compared to the measurements; however, the trend in $\langle X_{OH}|T\rangle$ decreasing downstream is still captured in the calculations. There is a large sensitivity of X_{OH} to temperature at T=1400 K, and consequently, when the product $X_{OH}X_{CO}$ is formed, there is a significant

overprediction at T=1400 K.

The mole fraction product $X_{CO}X_{OH}$ conditioned on a temperature of 1400 K is shown in Fig. 2.13 as a function of axial distance for both flames. This quantity is considered to be a comprehensive representation for this flame series in that the trend downstream reflects the observed changes in luminosity.

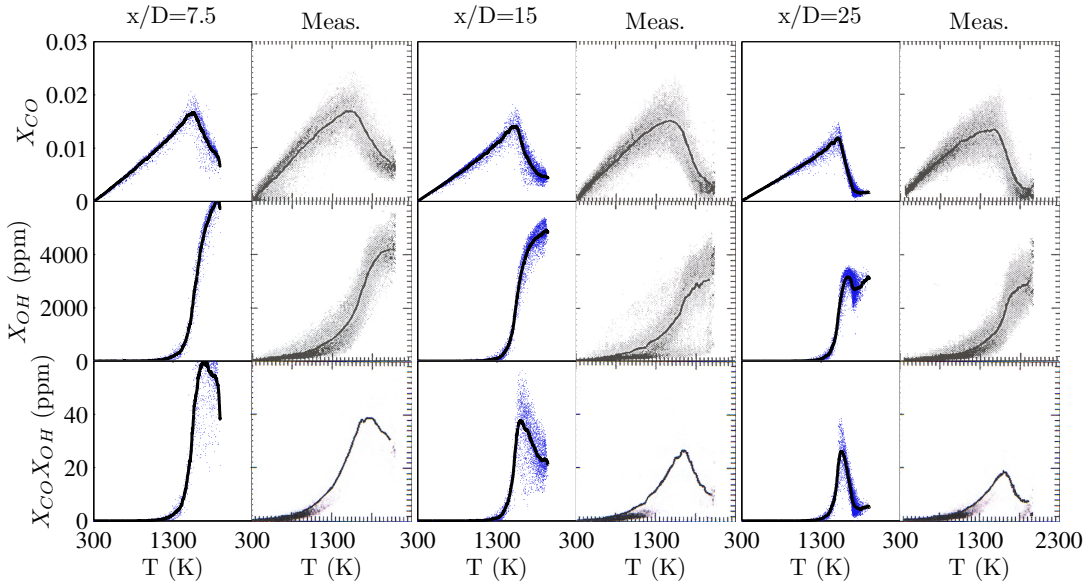

Figure 2.12: Scatter plots of CO mole fraction (top), OH mole fraction (middle), and the product of CO and OH mole fractions (bottom) in flame PM1-50 versus temperature. Axial locations are x/D=7.5 (left two plots), x/D=15 (middle two plots), and x/D=25 (right two plots). For each axial location, the left-hand plots are calculations and the right-hand plots are measurements. The solid line indicates the conditional mean.

The trend in PM1-50 is represented well with f_R=1, although the magnitude is largely underpredicted as explained previously. In PM1-200, however, $X_{CO}X_{OH}$ is overpredicted by two orders of magnitude in the base case. It is important to consider that none of the sensitivity studies with f_R=1 yield even the correct order of magnitude of this quantity. The large sensitivity in PM1-200 to f_R is shown in Fig. 2.13, and $X_{CO}X_{OH}$ is predicted reasonably only when the

chemistry is slowed by a factor of five or ten. Additionally, the slowed cases provide the correct order of magnitude and axial location for the small region of increased product formation observed near x/D of 60.

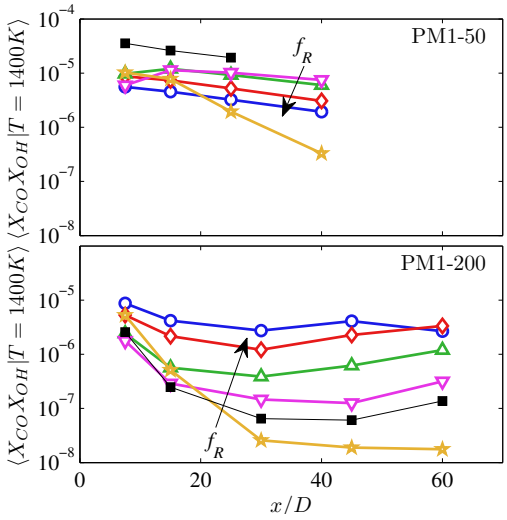

Figure 2.13: Product of CO and OH mole fraction conditioned on a temperature of 1400 K for the two flames presented from this flame series. Filled squares are measurements, PDF calculations of different values of f_R are open symbols: circles (blue), f_R=1, unperturbed; diamonds (red), f_R=0.5; triangles (green), f_R=0.2; upside-down triangles (magenta), f_R=0.1; stars (yellow), f_R=0, inert. The arrows indicate the direction of increasing f_R.

Quantification of reaction progress

In order to quantify and to compare the level of reaction progress in these flames, a reaction index is introduced. The reaction index based on temperature, R_T, is defined for each particle, i, according to $R_T^i = (T^i - T_{mix}^i)/(T_{eq}^i - T_{mix}^i)$ where T^i is the temperature of particle i, T_{mix}^i is the temperature of an inert mixture at the mixture fractions of particle i, and T_{eq}^i is the equilibrium temperature of particle i. A reaction index of zero corresponds to an unburnt particle, and

a reaction index of unity corresponds to a particle at equilibrium. It should be noted that this quantity is poorly defined when $T^i_{eq} = T^i_{mix}$, which occurs for streams initially at equilibrium, for example, both the pilot and the coflow here. So when this quantity is examined, only particles with sufficiently large jet mixture fractions are considered.

The particle values of R_T are shown for the base case of all flames in this series in Fig. 2.14. The particles are conditioned on a jet mixture fraction, ξ_j, greater than half the mean jet mixture fraction on the centerline, ξ^C_j. This conditioning has been compared to conditioning on particles originating from the jet, and the results are similar at this level of comparison. Figure 2.14 shows that for all four flame calculations, there is little difference in the evolution of reaction progress downstream, which is most likely incorrect based on the experimental observations.

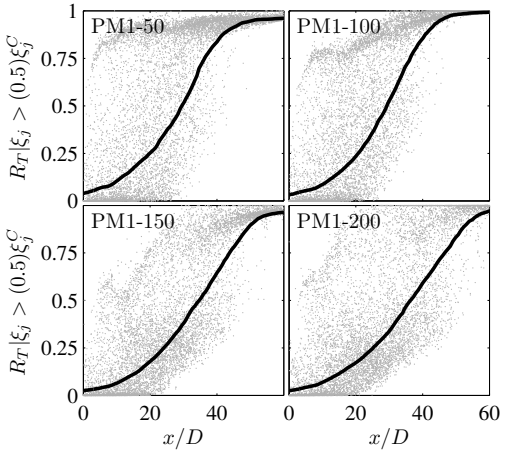

Figure 2.14: Reaction index based on temperature, R_T, for particles in base case calculations of all flames in this series. The mass-weighted mean conditioned on axial location is indicated by the solid line, and the particle values are indicated by the light dots. Particles are conditioned on a jet mixture fraction greater than half the mean jet mixture fraction on the centerline.

Figure 2.15 shows the same information for different values of the mixing model constant, C_ϕ, in calculations of PM1-200. As summarized in the sensitivity studies, there is little sensitivity to the mixing model constant. Since the reaction progress is generally determined by the scalar dissipation rate, it can be inferred that the scalar dissipation rate is largely uninfluenced by the mixing models and constants; this behavior is unlike several previous calculations of nonpremixed flames [6], in which the mixing models and constants significantly influence scalar dissipation rate.

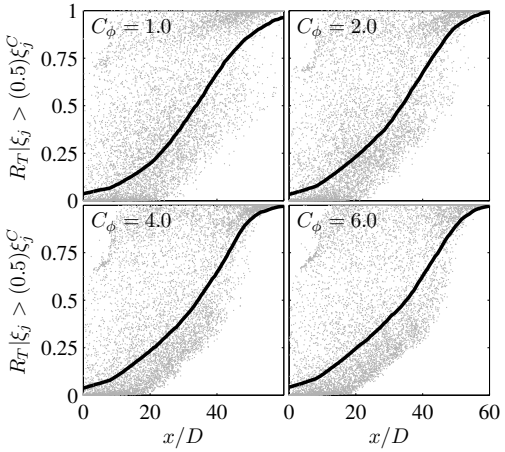

Figure 2.15: Reaction index based on temperature, R_T, for particles in calculations of PM1-200 for varying levels of C_ϕ, indicated in the top left corner of each plot. The mass-weighted mean conditioned on axial location is indicated by the solid line, and the particle values are indicated by the light dots. Particles are conditioned on a jet mixture fraction greater than half the mean jet mixture fraction on the centerline.

Lastly, Fig. 2.16 shows R_T from the diagnostic tests of PM1-200 in which the reaction rates are attenuated. From these tests, a more likely level of reaction index can be determined for this flame. Based on the previous comparisons, PM1-200 is better calculated with f_R of 0.1 or 0.2. Therefore it might be assumed that the reaction index for this flame is more realistically near the levels of that

determined for f_R of 0.1 or 0.2, which is generally lower by a factor of about five from the base case calculations.

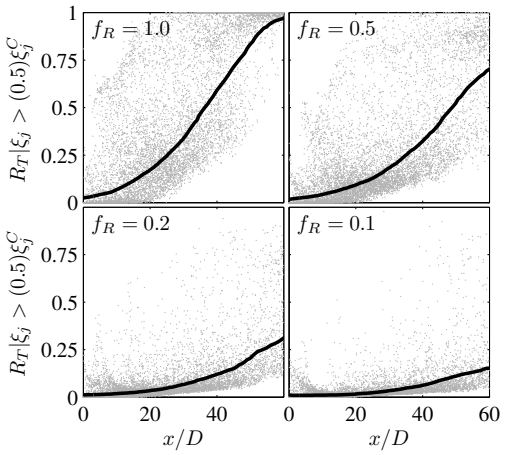

Figure 2.16: Reaction index based on temperature, R_T, for particles in diagnostic test calculations of PM1-200 for varying reaction rate attenuation factors, f_R, indicated in the top left corner of each plot. The mass-weighted mean conditioned on axial location is indicated by the solid line, and the particle values are indicated by the light dots. Particles are conditioned on a jet mixture fraction greater than half the mean jet mixture fraction on the centerline.

2.5 Conclusions

Calculations of a challenging series of lean piloted premixed jet flames have been performed using the PDF method. The following conclusions can be drawn from this study:

1. With the base case models and constants, the PDF method provides accurate calculations of PM1-50 with the exception of an overprediction in reaction progress localized in a small region near the centerline.

2. For PM1-200, with its increased jet velocity, the base case computations overpredict the extent of reaction much more severely than in PM1-50.

3. An extensive set of sensitivity studies on PM1-200 demonstrates that no set of models or parameters is able to predict the correct extent of reaction. PM1-200 is shown to be much more sensitive to the chemical reaction attenuation factor than is PM1-50. More accurate calculations of PM1-200 are obtained only by artificially slowing the chemistry.

4. Thorough studies are performed to show that transport is calculated accurately, and additional sensitivity studies show that the chemistry is insensitive to a wide variety of chemical mechanisms. By process of elimination, the mixing models are identified as a likely cause for the modeling deficiencies evident at these conditions.

5. The finite-rate chemistry effects are shown to be significant in this flame series. The PDF method is reaffirmed as a useful tool for investigating these effects and is shown to be computationally feasible for performing extensive sensitivity studies.

As in previous PDF calculations of premixed flames [11, 39], an aspect of the mixing model called into question is the specification of the mechanical-to-scalar time scale ratio, C_ϕ. These previous works have reported increased success with values of C_ϕ nearly an order of magnitude larger than the typically used values (i.e., C_ϕ in the range of 6 to 12, compared to typical values of C_ϕ in the range of 1.5 to 2.5). In the sensitivity studies of PM1-200, it is learned that increasing C_ϕ does in fact decrease the overprediction in reaction progress (Fig. SM-36-41). However, even a value of C_ϕ as large as 12 is unable to match the observed reaction progress. Furthermore, increasing C_ϕ degrades the calcu-

lation of the mixture fraction fields, and the mixture fraction fields are computed most accurately with C_ϕ in the range of 1.5 to 2.0. The aforementioned previous works have also indicated increased success when mechanical-to-scalar time scale ratio is specified based on a model for the scalar dissipation rate. This type of procedure has not yet been investigated in the PPJB flame series. However, it should be noted that the PPJB flames are quite different from the aforementioned premixed flames; for instance, the Damköhler numbers are significantly smaller in the PPJB flames, and it is concluded in [11] that the influence of the chemical reaction on the scalar dissipation rate is most considerable in the high Damköhler number limit.

The increase in jet velocity from 50 m/s in PM1-50 to 200 m/s in PM1-200 has several effects: the flow time scales (and hence the Damköhler numbers) are reduced (by about a factor of four); the pilot provides less shielding in that it is fully entrained in a significantly shorter distance; and (perhaps of least significance) the Reynolds number is increased by a factor of four. It is conjectured that the reduced shielding is the dominant effect. This could be tested experimentally by increasing the pilot velocity to maintain the same ratio to the jet velocity (as done in the Barlow & Frank flames [40]). Indeed a PDF calculation of PM1-50 with f_R=0.25 corresponds very closely to a calculation of PM1-200 with the pilot velocity increased by a factor of four; and it is evident that PM1-50 with f_R=0.2 (Fig. 2.5) is very different from PM1-200 (Fig. 2.6).

2.6 Acknowledgements

This work was supported in part by Air Force Office of Scientific Research, Grant FA9550-09-1-0047. This research was made with Government support under and awarded by DoD, Air Force Office of Scientific Research, National Defense Science and Engineering Graduate (NDSEG) Fellowship, 32 CFR 168a.

CHAPTER 3

COMPUTATIONAL STUDY OF LEAN PREMIXED TURBULENT FLAMES USING RANS-PDF AND LES-PDF METHODS

3.1 Introduction

3.1.1 Motivation for a Computational Study of Lean Premixed Combustion

Turbulent combustion is currently responsible for generating around 80% of the world's energy supply [1]. Given the world's growing needs for energy and, at the same time, reduced emissions of pollutants, understanding turbulent combustion is of prime practical importance. A better understanding of this intricate physical process, and the ability to incorporate this understanding into computational models, will ultimately lead to the ability to design combustion devices that can produce energy more efficiently, more reliably, and more cleanly.

One particular mode of combustion that yields improved efficiency and reduced emissions is lean premixed combustion [36, 41, 42]. With a lean premixture of fuel and oxidizer, the flame temperature is substantially reduced, resulting in decreased production of pollutants such as NO_x. Since the reacting mixture is fuel-lean, the abundance of oxidizer ensures a more complete burning of the fuel; the amount of products of incomplete combustion, such as CO and unburned hydrocarbons, is reduced.

However, lean combustion is subject to instabilities [43–45]. These instabil-

ities take the form of complex turbulence-chemistry interactions such as local extinction of the flame. They occur when the turbulence intensity is high, and the fuel is near its flammability limit. To ensure that combustion devices can be designed for safe and reliable operation while utilizing lean premixed combustion, it is essential to ensure that the computational models are able to capture these phenomena. Therefore, a set of experiments has been developed [12,12,12] in which these turbulent-chemistry interactions are present to various degrees, and detailed measurements have been made to allow comparison to model predictions.

3.1.2 Description of the Experiments to be Studied

The Sydney Piloted Premixed Jet Burner (PPJB) was developed to test turbulence-chemistry interactions at lean and highly turbulent conditions [12, 12, 12]. The burner consists of three main streams: a jet, a pilot, and a coflow. The central jet is lean, premixed methane-air exiting at a high velocity. Surrounding the jet is a hot pilot of stoichiometric methane-air combustion products at a low velocity. Around the pilot is a hot coflow of lean hydrogen-air products. More detailed information on the bulk properties of the inflowing streams is presented in Table 3.1. The diameter of the central jet, D, is 4 mm, and is taken to be a reference length scale throughout this study.

Four different flames are studied on the PPJB, and differ only in the bulk velocity of the central jet. The four flames are denoted as PM1-50, PM1-100, PM1-150, and PM1-200 with jet bulk velocities of 50, 100, 150, and 200 m/s, respectively. The Reynolds number, Re, based on the bulk velocity of the jet, the

Stream	Vel. (m/s)	Temp. (K)	Eq. Rat.	Fuel / Oxid.	Diameter (mm)
Jet	50-200	300	0.5	Methane / Air	4.0
Pilot	5.3	2280	1.0	Methane / Air	23.5
Coflow	3.7	1500	0.43	Hydrogen / Air	197

Table 3.1: Properties of the inflowing streams for the Piloted Premixed Jet Burner.

jet diameter, and the unburned jet composition, increases from 12,500 in PM1-50 to 50,000 in PM1-200. As the jet bulk velocity increases, the luminosity of each flame is observed to vary differently in the axial direction. Flames PM1-50 and PM1-100 have strong luminosity throughout the length of the flame. Flame PM1-150 exhibits reduced luminosity between x/D of 15 and x/D of 45. Flame PM1-200 has the most drastic reduction in luminosity, extending from x/D of 7.5 to x/D of 45. Beyond x/D of 45 there is a very faint increase in the flame luminosity, suggesting that burning begins to increase in intensity around this region.

Detailed measurements of both velocity and scalar statistics have been made for these four flames. The burner is characterized and the stability of the flames is explored as a function of the jet equivalence ratio and bulk velocity in [12]. By seeding the jet with particles, laser doppler velocimetry is used to measure the mean and fluctuating axial and radial components of velocity [12]. Simultaneous two-dimensional images of both temperature and the mass fraction of OH are obtained using Rayleigh-OH planar laser-induced fluorescence (PLIF) [12]. The thermochemical composition throughout these flames is further revealed through simultaneous line measurements of temperature and mass fractions of the chemical species CH_4, O_2, N_2, H_2, H_2O, CO_2, CO, and OH, from which radial profiles of the mean and RMS of these quantities are obtained [12]. These

measurements are made using the Raman-Rayleigh procedure. Additionally, measurements of the CO mass fraction are made using laser-induced fluorescence (LIF) and measurements of the OH mass fraction are made using PLIF. Lastly, simultaneous imaging of temperature and the mass fractions of OH and CH_2O is performed to further explore the finite-rate chemistry effects in these flames [12].

3.1.3 Previous Calculations of this Flame Series

Several previous studies of this flame have been performed or are currently in progress. In [12], a hybrid Reynolds-Averaged Navier-Stokes (RANS) and transported composition probability density function (PDF) method is used to make calculations of all four flames. The calculations use two-equation turbulence models and detailed chemistry. It is found that the flame length is underpredicted in the calculations, as a result of both the jet spreading too rapidly, and the reaction progress being overpredicted. A study of the mixing model constant, C_ϕ, shows that larger values of C_ϕ result in a cross product of CO and OH mole fractions, $CO \times OH$, with qualitative behavior in better agreement with the experimental measurements. However, the magnitude of $CO \times OH$ is over an order of magnitude too large in these calculations, and the scalar statistics such as the RMS temperature do not agree quantitatively with the measurements, so the effect of C_ϕ is still ambiguous.

In [46], a hybrid RANS and joint velocity - turbulence frequency - composition PDF method is used to model all the flames in the series. Calculations of the mean and RMS species mass fractions and temperature are in reason-

able agreement with the experimental measurements for flame PM1-50. For flame PM1-200, the mean and RMS mixture fractions are in good agreement with the experimental data for all locations at which measurements have been taken; however, the mean temperature is substantially overpredicted and the mean fuel mass fraction is underpredicted, showing that the reaction progress is overpredicted in the calculations. A comprehensive set of sensitivity studies is performed on flame PM1-200 to examine the effect of nearly all aspects of the modeling on the amount of reaction progress calculated for PM1-200. This study involves the use of different detailed chemical mechanisms, mixing models, mixing model constants, turbulence model constants, and inflow boundary conditions. No parameter in the investigated parameter space yields a significant reduction of the reaction progress, and it is reasoned that the mixing models are the largest source of modeling uncertainty. These calculations also suffer from poor predictions of mixture fractions and temperature in the near field of the mixing layer between the pilot and coflow streams. Lastly, the results are sensitive to the value of the turbulence model constant $C_{\omega 1}$, which controls the spreading rate of the jet; a value of 0.70 is used to adequately calculate the spreading rate of the jet, which is the same as the value used in some other calculations of jet flames [47], but is slightly larger than the values of 0.56 and 0.65 used more commonly in previous studies of jet flames [6, 8, 47].

In [48], LES calculations of PM1-100 are performed. In these calculations, the filtered reaction source term is taken from the reaction source term evaluated at the filtered composition field, so the effect of subgrid-scale variations in the composition is essentially neglected. The mean velocity field is in good agreement with the experimental measurements. The radial profiles of mean and RMS species mass fractions and temperature are compared at x/D of 2.5,

7.5, and 15. Generally, the agreement between the experimental and calculated mean and RMS scalar fields is good for x/D of 2.5 and 7.5. At x/D of 15, the mean temperature is underpredicted in the pilot region, and overpredicted near the centerline, suggesting that the calculations either overpredict the rate at which the pilot spreads into the jet or overpredict the reaction progress. The study also finds that 1-step and 2-step chemical mechanisms are insufficient to calculate the mean CO mass fraction and mean temperature accurately using this methodology, whereas a 20-species, 82-reaction skeletal mechanism results in improved predictions of these quantities.

In more recent and ongoing works, [49] uses a RANS and conditional moment closure (CMC) methodology to perform calculations of PM1-50 and PM1-200. The results indicate a behavior of the reaction progress similar to that in [12, 46, 48]; the reduced amount of variables used in the CMC is found to provide description of the chemistry of equal quality to calculations without a reduced-variable description of the flow. In [50], an Eulerian stochastic fields methodology with LES and detailed chemistry is used to make calculations of flame PM1-100. Good agreement in the mean and RMS scalar fields is obtained at x/D of 7.5 and farther downstream at x/D of 45. From x/D of 15 to 30, the mean temperature is overpredicted and the mean fuel mass fraction is underpredicted in the calculations, with observations similar to those in [46,49]. In [51], a flamelet and progress variable combustion model is used in conjunction with LES. The combustion model uses an additional variable to account for heat loss, which results in improved predictions of the mean temperature. Calculations of PM1-100 show good agreement with the experimental data up to x/D of 15, the last location at which results are presented.

The modeling approaches used in the previous calculations cover a wide range of the currently existing models. However, none of the previous works has proved successful for PM1-150 and PM1-200. Furthermore, most of the calculations of PM1-100 report results only around the near-field of the jet, that is, between x/D of 2.5 and 15, and not further downstream at x/D of 30 or 45.

3.1.4 Objectives for this Study

In light of the findings of the aforementioned previous works, it is clear that there is much to address regarding the ability of existing models and methodologies to compute the flames PM1-150 and PM1-200 accurately. This work targets four particular components of the modeling: the level of turbulence closure (LES-PDF and RANS-PDF), the description of the chemistry (flamelet-based and detailed chemical kinetics), the treatment of molecular diffusion, and the imposed inflow boundary conditions. The objective of this study is to quantify how sensitive the calculations are to these particular components of the models. The most important model components for accurate calculations of these flames are identified, and the computational cost of each is assessed. This study aims to address all flames in the PPJB series, and to compare results at all relevant locations throughout the flames.

A brief overview of the contents of the remainder of this chapter follows. In Sec. 2, the RANS-PDF methodology is described and the computational configuration for those calculations is explained. The implementation of three components of the RANS-PDF model are described and tested, and the effect on the calculations is shown. These three components are: (1) a random walk model

for molecular diffusion, (2) a combustion model based on flamelet-generated manifolds (FGM), and (3) inlet boundary conditions. In Sec. 3, the LES-PDF methodology is described along with the computational configuration of the LES-PDF calculations. The numerical accuracy of the LES-PDF calculations is demonstrated, and the effects of molecular diffusion modeling are examined. The focus of the LES-PDF studies is on the effects of differential diffusion and the model constant, C_M. Following the LES-PDF study, the most important results are discussed in Sec. 4 and conclusions are drawn in Sec. 5.

3.2 RANS-PDF Calculations

One of the notable characteristics of the PPJB flames is the importance of finite-rate chemistry effects. So, when considering modeling these flames, a natural choice for a methodology is a model in which the effects of chemical reaction can be treated exactly. With the probability density function (PDF) method [2,16,52], this is exactly the case; thus it is the basis of all the computational work performed in this study. A second notable characteristic of the PPJB flames is that these important finite-rate chemistry effects occur in flows of simple geometry. There are no wall effects, swirl, or recirculation, and the flow is statistically axi-symmetric. Therefore, a logical first choice for the type of PDF method used to study these flames is one with turbulence closure based on the Reynolds-Averaged Navier-Stokes (RANS) equations. Specifically, the joint velocity-turbulence frequency-composition PDF method [16] is used, in which the joint PDF of the fluctuating velocity, turbulence frequency, and thermochemical composition is solved by a coupled finite-volume solver and particle solver.

RANS-PDF methods have been successfully applied to many jet flames in past studies. The non-premixed methane-air Sandia flames D, E, and F [40] exhibit phenomena of extinction and re-ignition which have been well captured by several RANS-PDF modeling studies [5, 6, 47, 53]. Additionally, the non-premixed lifted hydrogen-air flame in a hot coflow [54] has been the subject of several successful RANS-PDF modeling studies [8,47,55,56]; this flame exhibits a sensitivity to the coflow temperature which has been well-captured by RANS-PDF methods [8]. In addition to non-premixed turbulent jet flames, RANS-PDF methods have also been applied to turbulent premixed jet flames [10,11,39], including two of the previously mentioned studies of the PPJB [12,46]. One of the drawbacks of the PDF method is the need to model the effect of molecular diffusion through a mixing model. In several calculations of premixed flames, this aspect of the model has been suggested to be the primary source of modeling error [11, 12, 46], and therefore modeling studies need to be careful to address the sensitivities to the various parameters of these mixing models.

3.2.1 Joint PDF Computational Methodology

The calculations described in [12, 46] both used RANS-based approaches. The RANS-PDF calculations to be described in this work are based on the same joint velocity-frequency-composition PDF used in [46]. This method is implemented computationally through a coupled finite-volume/particle solver [23].

In the particle solver, Lagrangian particles evolve in position, velocity, turbulence frequency, and composition. The velocity is modeled by the Simplified Langevin Model (SLM) [17]. The turbulence frequency is modeled by a stochas-

tic frequency model [18]. The composition evolves by mixing and chemical reaction. This study uses the EMST mixing model [19], which previous studies [46] have shown to be superior in the PPJB calculations upon comparing scatter plots of the particle composition. The chemical reaction source term is evaluated from detailed chemical kinetics. These calculations use the 16-species ARM-1 mechanism [26], which is shown to yield calculations of these flames of similar quality to those of more detailed mechanisms [46]. The storage-retrieval technique of *in-situ* adaptive tabulation (ISAT) [20, 21] is used to compute the change in composition due to chemical reaction in a computationally efficient manner.

The finite-volume solver solves the mean equations for mass, momentum, energy, and thermochemical state. The particle solver provides the finite-volume solver with the turbulent fluxes and the mean chemical source term. The finite-volume solver provides the mean density and fluctuating component of velocity to the particle solver. When the solution reaches a statistically stationary state, the statistics are time-averaged until sufficient temporal convergence is attained.

3.2.2 Numerical Configuration for the RANS-PDF Calculations

The RANS-PDF calculations are preformed on a two-dimensional cylindrical domain as shown in Figure 3.1. The domain extends $100D$ in the axial direction, where D is the jet diameter and the axial coordinate is denoted by x. The domain extends $40D$ in the radial direction, whose coordinate is denoted by r. The grid size is 144×144 cells in the axial and radial directions. This set up is identical

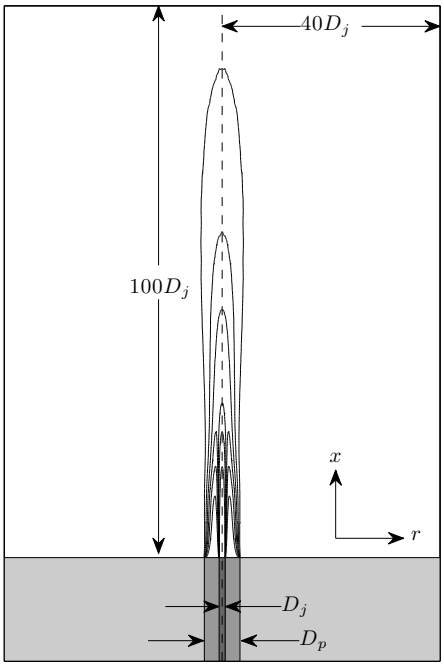

Figure 3.1: Sketch of computational domain for RANS-PDF calculations. The centerline is indicated by the vertical dotted line, and the domain extends to the boundary of the white colored region. The extent of the domain in the axial and radial directions is indicated by the vertical and horizontal measurements in the white region, respectively. In the gray region at the bottom, the location of the three stream boundary conditions are shown by shades of gray; outward from the centerline, they are the central jet, the pilot, and the coflow. The dimensions at the bottom are of the diameters of the jet and pilot. A contour of the mean CO_2 mass fraction from a calculation of PM1-100 is shown in the sketch of the computational domain.

to that used in [46], and the numerical accuracy of such a configuration has previously been assessed. The maximum error in the mean temperature is about 4%, and about 8% for the RMS temperature in PM1-200 [46]. The values for the model constants are shown in Table 3.2, and are the same used in many previous studies of turbulent jet flames.

Boundary conditions are obtained from separate calculations on an extended

Constant	Value	Usage
C_0	2.1	SLM
C_Ω	0.6893	Definition of the mean frequency Ω
$C_{\omega 1}$	0.70	Turbulence frequency model
$C_{\omega 2}$	0.90	Turbulence frequency model
C_3	1.0	Turbulence frequency model
C_4	0.25	Turbulence frequency model
C_ϕ	1.5	EMST mixing model

Table 3.2: Model constants for base-case RANS-PDF calculations.

domain, ranging from x/D of -100 to 100 in the axial direction, and the profiles of velocity and turbulence quantities are extracted at the burner exit plane, x/D of 0, as in [46]. The thermochemical composition at the inlet boundary is prescribed in one of two ways: the first way is to define the composition of the burned streams (that is, the pilot and coflow) to be at chemical equilibrium; the second way is to define the composition of those streams based on a fully burnt laminar flame. The composition of the fully burnt laminar flame is obtained from a Chemkin calculation using the 44-species UCSD mechanism [32] and considering full multi-component transport and thermal diffusion. The resulting boundary conditions are presented in detail in Table 3.3.

3.2.3 The Effect of Molecular Diffusion in the RANS-PDF Calculations

It is found in [46] that the mixing layer between the pilot and the coflow is predicted to evolve much more slowly in the calculations than observed in the experiments. Because the pilot and the coflow bulk velocities are both low and the molecular diffusivity of each stream is large, the observed discrepancy is

Stream	Composition Variable	Equilibrium	Laminar Flame
Jet	O_2	2.26×10^{-1}	2.26×10^{-1}
	CH_4	2.84×10^{-2}	2.84×10^{-2}
	N_2	7.45×10^{-1}	7.45×10^{-1}
	$T(K)$	300	300
Pilot	H_2	3.09×10^{-4}	4.17×10^{-4}
	H	2.11×10^{-5}	3.88×10^{-5}
	O_2	7.72×10^{-3}	1.00×10^{-2}
	OH	2.42×10^{-3}	3.08×10^{-3}
	H_2O	1.20×10^{-1}	1.18×10^{-1}
	CO	1.09×10^{-2}	1.41×10^{-2}
	CO_2	1.34×10^{-1}	1.29×10^{-1}
	N_2	7.25×10^{-1}	7.25×10^{-1}
	T (K)	2280	2240
Coflow	H_2	6.73×10^{-8}	1.02×10^{-6}
	O_2	1.31×10^{-1}	1.32×10^{-1}
	OH	5.24×10^{-5}	1.93×10^{-4}
	H_2O	1.11×10^{-1}	1.11×10^{-1}
	N_2	7.57×10^{-1}	7.57×10^{-1}
	T (K)	1500	1490

Table 3.3: Thermochemical compositions used for the inlet boundary conditions for each stream. The species are shown in units of mass fraction, and are reported only where the mass fraction exceeds 10^{-6}. Two different boundary condition formulations are shown: compositions taken from chemical equilibrium in the burned streams, and compositions taken from a fully burnt laminar flame in those streams.

most likely due to molecular diffusion. In turbulent flames, molecular diffusion is usually small compared to turbulent diffusion, so it is typically neglected in these types of RANS-PDF calculations. To investigate the first-order effects of molecular diffusion in these flames, a simple random walk model is implemented into this method.

In this simple model for molecular diffusion, two additional terms are added to the equation for advancing a particle's position in physical space as illus-

trated in Eq. 3.1:

$$d\mathbf{X}^* = \mathbf{U}^* dt + \left(\frac{1}{\langle \rho \rangle} \nabla \left(\langle \rho \rangle \alpha \right) \right)^* dt + \sqrt{2\alpha} d\mathbf{W} \tag{3.1}$$

where $d\mathbf{X}^*$ is the change in a particle's position, $\mathbf{U}^*$ is the current particle velocity, dt is the time step, $\langle \rho \rangle$ is the volume-weighted mean density, $d\mathbf{W}$ is an increment in an isotropic, vector-valued Wiener process, and α is the mass-weighted cell mean molecular diffusivity which depends on position. The second and third terms on the right-hand side are evaluated based on interpolation of the fields onto the particle's current position. The first additional term in Eq. 3.1 represents the mean drift due to molecular diffusion, while the last term represents a random-walk term. It is very important to note that this simple model results in a spurious production of variance due to the random-walk term [57,58]. Therefore, this model is only used to examine the first-order effects in the RANS-PDF calculations, and more sophisticated models are discussed and used later in this work.

Before examining this model's effects on the PPJB calculations, several tests are performed to verify its correct implementation. Each test consists of a two-stream laminar mixing layer with distinct species mass fractions specified in each stream; the coordinate system, density, and diffusivity are varied among the tests to verify each component of the model. Four test cases are considered, and are outlined in Table 3.4.

The results from the test cases are compared to solutions from the commercial CFD tool Fluent and to analytical solutions where possible. Each solution is investigated for sufficient numerical accuracy by varying the grid size, the number of particles per cell, and the duration of time-averaging. The results of these

Test Case	Coordinate System	Density	Diffusivity
A	Planar	Uniform	Uniform
B	Cylindrical	Uniform	Uniform
C	Cylindrical	Variable	Uniform
D	Cylindrical	Variable	Variable

Table 3.4: Test cases for verification of the random walk model for molecular diffusion implementation in the RANS-PDF calculations.

verification tests are summarized in Figure 3.2, where lateral and radial profiles of species mass fractions from test cases A and D are shown. The results from all the test cases are found to be in good agreement with the results from other solution methods; next, the effect of this model is examined in the calculations of the PPJB flames.

To implement the simple model based on Eq. 3.1, the molecular diffusivity must be defined. In this simple implementation of molecular diffusion, the Lewis number is taken to be unity, so that the molecular diffusivity is simply equal to the thermal diffusivity. For all the compositions realized throughout a flamelet generated manifold (FGM) discussed later in this work, the thermal diffusivity is evaluated using Chemkin, and a curve-fit is constructed as a function of temperature as

$$\alpha(T) = \alpha_0 \, (T/T_0)^b \, , \tag{3.2}$$

where α is the molecular diffusivity, and T is the mass-weighted cell mean temperature. The reference temperature, T_0, is defined as 300 K, where the reference diffusivity, α_0, is equal to 2.24×10^{-5} m^2/s. The exponent, b, is obtained from the curve-fit, and is equal to 1.71. Comparisons of the transport properties evaluated on the FGM to the curve-fits are presented later in this work.

Presented in Figure 3.3 is a comparison between two calculations and the ex-

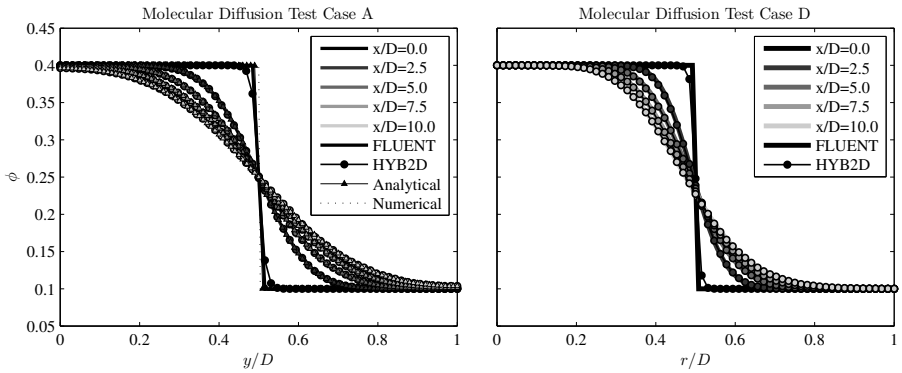

Figure 3.2: Mass-weighted mean species mass fractions in tests of the molecular diffusion implementation. The figure on the left shows the results from the constant-density, constant-diffusivity test case in Cartesian coordinates; the figure on the right shows the results from the variable-density, variable-diffusivity test case in cylindrical coordinates. The color of the lines denotes the axial location as indicated in the legend. The solid lines are from a verification of the test case using the commercial code Fluent; the lines with circle markers are from the new molecular diffusion implementation in the RANS-PDF code, HYB2D; the lines with triangular markers are from an analytical solution; the dashed lines are from a numerical finite difference solution.

perimental measurements for the time-averaged mass-weighted mean temperature and pilot mixture fraction for flame PM1-50. In these flows, three streams are considered, and a mixture fraction is associated with each stream. The mixture fraction represents the fraction of mass originating from that stream, and it is defined here based on a linear combination of the elemental mass fractions, H, O, and C. The first set of calculations shown in Figure 3.3 is essentially identical to that in [46], and the second set of calculations is identical, except with the additional terms in Eq. 3.1 to model the molecular diffusion, and the diffusivity evaluated through Eq. 3.2.

There are three important observations from the comparison of these two

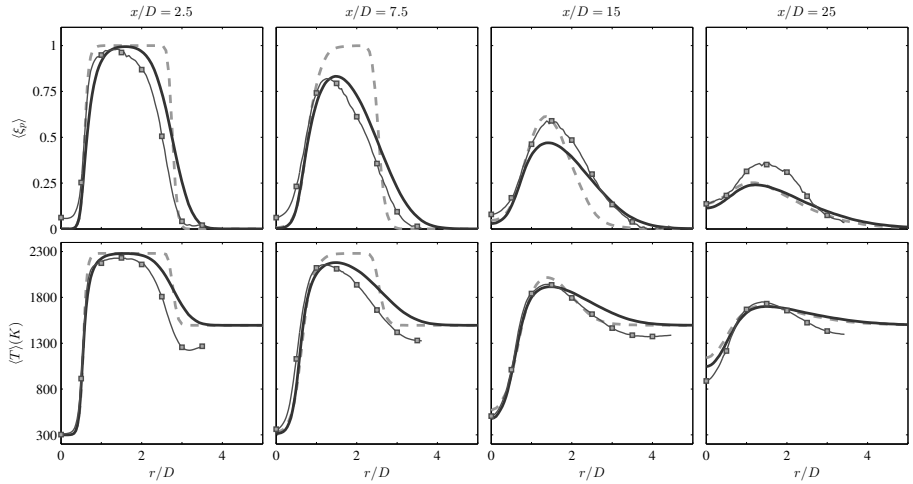

Figure 3.3: Radial profiles of mass-weighted mean pilot mass fraction (top plots) and mass-weighted mean temperature (bottom plots) from calculations and measurements of flame PM1-50 showing the effect of modeling molecular diffusion. The axial location is indicated at the top of each column, and increases from left to right. Dashed gray line – RANS-PDF without molecular diffusion; Solid line – RANS-PDF with molecular diffusion; Lines with squares: experimental data [12].

calculations. The first is that the calculations with molecular diffusion have much more accurate profiles of mean scalars (such as temperature and pilot mixture fraction) in the pilot-coflow mixing layer. The results convincingly show that molecular diffusion is important in this region of the flow, due to the low velocity of the pilot and coflow streams. This marks a significant difference between the PPJB flames and other turbulent jet flames previously studied. The second important observation is that the overall reaction progress of the jet is not significantly affected by the new treatment of molecular diffusion. This occurs mainly because the pilot-coflow mixing layer is sufficiently far from the central fuel jet; by the time the pilot-coflow mixture interacts with the central jet fluid, the pilot and coflow are already well-mixed. A third observation, which will be presented and discussed more in detail in Sec. 3.3, is that the spurious

variance introduced by this random-walk model is large and is clearly evident in the radial profiles of the RMS of temperature and chemical species, up to at least x/D of 15.

3.2.4 The Effect of the Temperature at the Inlet Boundary Condition

Having examined the first-order effect of molecular diffusion on the PPJB calculations, a second important aspect of the model is next examined, namely, the temperature prescribed at the inlet boundary. One deficiency observed in previous calculations of the PPJB flames is an overpredicted temperature in the coflow near the burner exit, by as much as 300 K [12, 46, 48–50]. This discrepancy occurs because, in the experiments, the hot coflow transfers heat to the cold unreacted pilot stream, and this heat transfer is not taken into account in these calculations. The heat loss has been investigated in some previous studies [12, 46], but the results have been not been convincingly improved, possibly due to the neglect of molecular diffusion in those former calculations. In [51], the heat loss is accounted for, but it is specified empirically from an extrapolation of the measurements at x/D of 2.5. The purpose of this part of the study is to perform a thorough analysis of this boundary condition, and to examine the sensitivity of the calculations to it. Because molecular diffusion is now included, much better agreement is obtained in the pilot-coflow mixing layer.

To model the heat transfer between the pilot and coflow, the commercial CFD tool Fluent is used. The domain of these calculations extends from $x/D = -100$ to $x/D = 100$, as in the previous calculations used to obtain the boundary con-

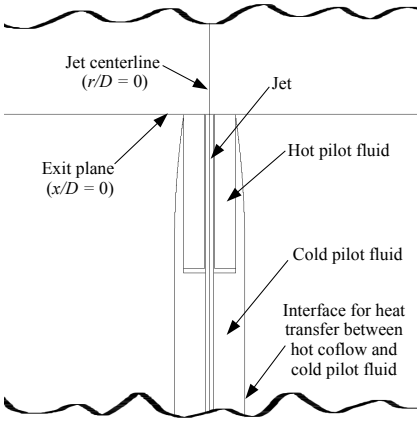

Figure 3.4: Sketch showing the geometry used to formulate inflow boundary conditions with heat transfer from the coflow to the cold pilot fluid. The upstream region extends below the jet centerline, and the downstream region extends above the jet centerline. In the adiabatic calculations, there is no heat transfer at the pilot-coflow interface, but in the non-adabatic calculations, heat transfer occurs between the hot coflow and cold pilot fluid.

ditions. At the region from $x/D = -100$ to 0, referred to as the upstream region, conjugate heat transfer is modeled between the cold pilot fluid and the hot coflow through the pilot-coflow wall. A detail of the upstream region is shown in Figure 3.4. The heating takes place over the entire length of the upstream region, and the thermal boundary layer is fully developed by the jet exit plane at x/D of 0. This boundary condition is implemented into the RANS-PDF calculations by extracting the temperature and density at $x/D = 0$, as well as the velocity and turbulence properties as before. In the RANS-PDF calculations, the density is prescribed at the inlet from these conditions, and the sensible enthalpy is obtained from the species mass fractions and temperature.

Shown in Figure 3.5 is a comparison between the calculations with and with-

out heat loss in the coflow. Three important observations can be made from this figure. The first is that the time-averaged mass-weighted mean temperature is predicted with much greater accuracy when the heat transfer is accounted for, as would be expected. With an adiabatic coflow, there is a 300 K temperature disparity near the pilot-coflow mixing layer, which propagates downstream even farther than x/D of 25, the measurement location farthest downsteam. The agreement in the mean temperature between the experimental measurements and calculations with heat transfer is excellent near the burner exit at x/D of 2.5. The agreement degrades slightly going downstream, which is most likely a result of the turbulence modeling of the spreading of the pilot stream. This is confirmed by examining the pilot mixture fraction, which spreads slightly faster in the calculations compared to the experiments.

The second important observation from Figure 3.5 is that the calculations with heat transfer in the boundary conditions have profiles of the time-averaged mass-weighted mean pilot mixture fraction which are shifted from the previous calculations toward the centerline, in much better agreement with the experimental data. This occurs primarily due to the inclusion of the chamfered edge of the pilot-coflow wall in this boundary condition formulation, and not necessarily due to the heat transfer itself. The chamfered edge results in a slightly larger radial velocity toward the centerline, and hence, slightly faster entrainment of the coflow. Other calculations which do not account for the chamfered edge [12, 46, 48–51] display similar behavior, and could benefit slightly from that addition in the boundary condition. The last observation from Figure 3.5 is that the overall combustion of the fuel from the central jet is not significantly affected by the temperature treatment at the inlet boundary condition, for this range of temperatures. By the time the jet mixes with the fluid from the pilot-

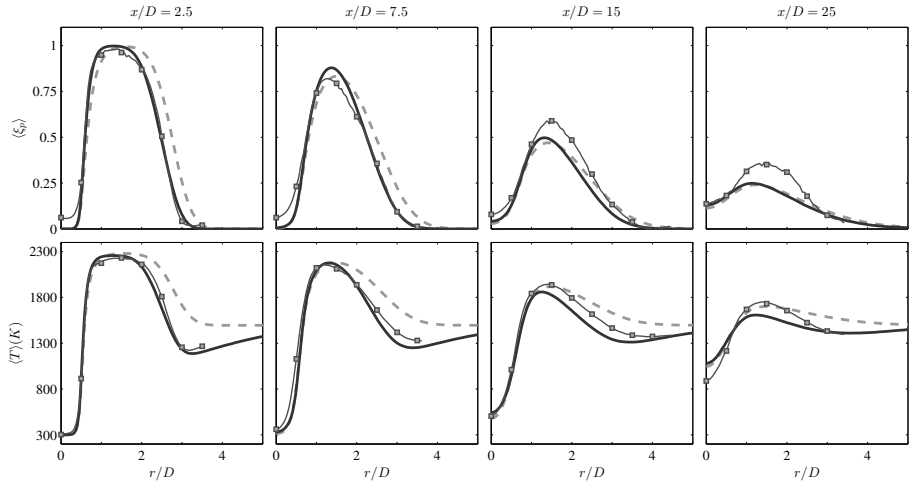

Figure 3.5: Radial profiles of time-averaged mass-weighted mean pilot mass fraction (top plots) and time-averaged mass-weighted mean temperature (bottom plots) from calculations and measurements of flame PM1-50 showing the effect of modeling conjugate heat transfer between the pilot and coflow. The axial location is indicated at the top of each column. Dashed gray line: RANS-PDF calculations with adiabatic boundary conditions; Solid line: RANS-PDF calculations with conjugate heat transfer; Lines with squares: experimental data [12].

coflow mixture layer, it is already sufficiently well-mixed. The findings agree with those of [46], where reducing the coflow temperature in PM1-200 to as low as 1200 K did not significantly impact reaction progress.

3.2.5 Comparison of Combustion Modeling Methodologies

In the next part of this work, a flamelet-generated manifold (FGM) [59,60] is applied to model the combustion in the PPJB. The purpose of doing so is two-fold: firstly, to reduce the computational cost, particularly for the more expensive LES-PDF studies; and secondly, to examine the sensitivity of the PPJB calculations to the combustion modeling. These studies provide a direct comparison

between calculations with detailed chemistry and calculations with simplified combustion models.

For this particular application of FGM, three variables are considered: a mixture fraction of both the jet and pilot streams, ξ_j and ξ_p, and one reaction progress variable, taken here to be the sensible enthalpy, h_s. A grid is constructed in the ξ_j and ξ_p mixture fraction space; for each point in the grid, a chemical composition corresponding to inert mixing of the three streams is formed based on the values of ξ_j and ξ_p at that point. From this composition, a freely-propagating laminar flame is computed for each value of mixture fraction in the grid. In the RANS-PDF calculations, both mixture fractions have no source term. The source term for the sensible enthalpy, $\dot{h_s}$, is evaluated by performing a table look-up from the current values of ξ_j, ξ_p, and h_s and interpolating. The change in h_s over one time step is then computed from simple Euler integration, with integration performed over n_{sub} sub-steps within the current time step as shown in Eq. 3.3:

$$h_s(t+\Delta t) = h_s(t) + \int_t^{t+\Delta t} \dot{h_s}\left(\xi_j(t'), \xi_p(t'), h_s(t')\right) \mathrm{d}t'. \tag{3.3}$$

A second manifold is constructed by the same process as above, but instead of computing a laminar flame, an auto-ignition calculation is performed for each composition formed by inert mixing of the three streams. The purpose of this second manifold is to examine the importance of diffusive effects, and to facilitate comparisons between the two sets of boundary conditions from Table 3.3. For each of these two manifolds, calculations are made using the 44-species UCSD mechanism [32] and the 111-species USC-Mech-II chemical mechanism [33]. The first of the manifolds, assembled from laminar flame cal-

culations, is denoted as FGM-LF; the second, assembled from auto-ignition calculations, is denoted as FGM-AI.

The numerical accuracy of this method is affected by the size of the grid in ξ_j, ξ_p, and h_s, the number of time steps over which the numerical integration is performed, and accuracy to which the flamelets are computed. Convergence studies are performed over all of these parameters, and an error in the ignition delay time, ϵ_t, is defined for each configuration by

$$\epsilon_t = \left| t_{ig}^{FGM} - t_{ig} \right| / t_{ig}, \tag{3.4}$$

where t_{ig}^{FGM} is the ignition delay time based on that configuration of the FGM, and t_{ig} is the ignition delay time computed directly from a laminar flame calculation (or an auto-ignition calculation, in the case of the second manifold) of sufficient numerical accuracy computed using Chemkin. The ignition delay time is defined here as the time taken for the sensible enthalpy of a particle starting from the unburned composition to increase by 50% of the total change in sensible enthalpy. Accuracy tests are conducted using a time step of 10^{-6} seconds, which is near the time step used in the calculations. The time evolution of sensible enthalpy and its time rate of change for a value of (ξ_j, ξ_p) around the most sensitive region of mixture fraction space, $(0.47, 0.50)$, in one of the accuracy tests is illustrated in Figure 3.6. This figure illustrates the consistency between the solution computed using appropriate accuracy in a Chemkin calculation and the solution computed from interpolating in ξ_j, ξ_p, h_s, and time in the FGM.

The accuracy test of the grid size and interpolation is illustrated in Figure 3.7. Three grids are defined, FGM-16, FGM-32, and FGM-64, and have, respectively,

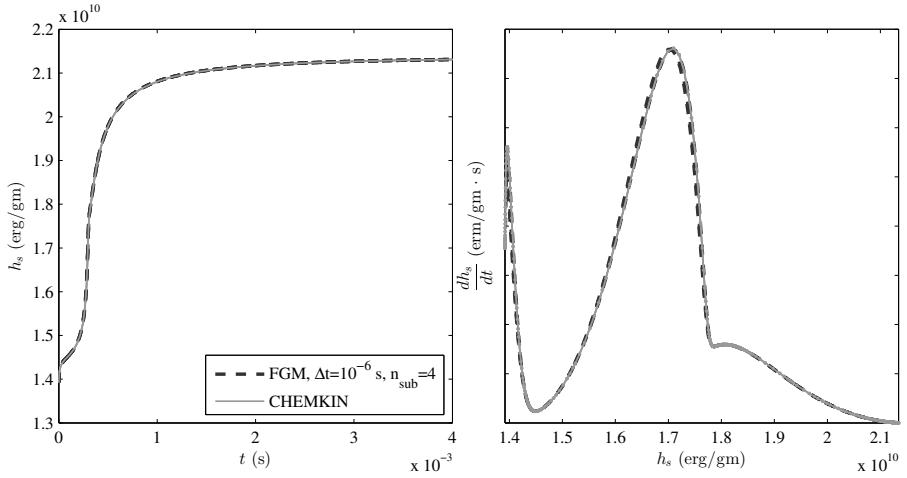

Figure 3.6: Plots of sensible enthalpy, h_s, versus time, t, (left) and the time rate of change of sensible enthalpy, $\dot{h}_s$ or dh_s/dt, versus sensible enthalpy (right) for jet and pilot mixture fractions of (0.47, 0.50). The dark dashed line is computed using a FGM using a time step, Δt, of 10^{-6} and 4 time sub-steps; the light solid line is computed using the commercial software Chemkin using appropriately low values for error tolerances. The rapid variation at the initial time step is due to the reaction of radicals from the pilot and coflow mixtures.

16, 32, and 64 grid points in each dimension. For a large number of points inside the range ($0.44 \leq \xi_j \leq 0.56$) and ($0.44 \leq \xi_p \leq 0.56$), ϵ_t is measured. The convergence tests shown in Figure 3.7 reveal that the error decreases as the grid is refined. Secondly, the error is lowest at the locations near the grid nodes. This study shows that the error from the grid discretization is larger than the error associated with the time sub-step. A grid size of $32 \times 32 \times 100$ in ξ_j, ξ_p, and h_s, and a value of n_{sub} of 4 yields a maximum ϵ_t of about 0.10, and the results from calculations of the PPJB are insensitive to numerical parameters giving greater accuracy. Therefore, these are the numerical parameters used in this study of the FGM.

Figure 3.8 shows the results of using both FGM-AI and FGM-LF with the

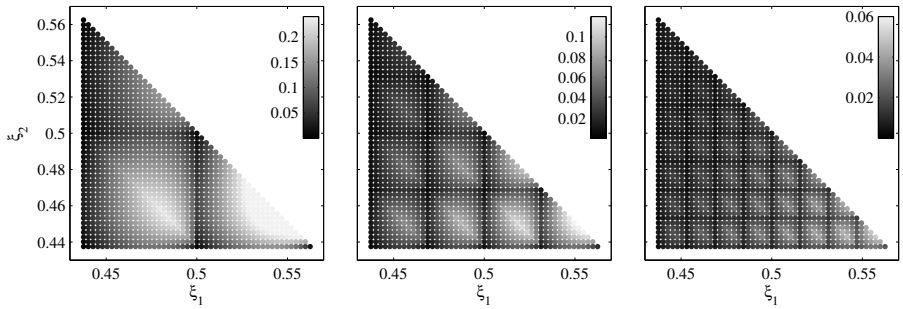

Figure 3.7: Plot in the two-dimensional mixture fraction space colored by the error in ignition delay time as defined in Eq. 3.4 for FGM's constructed on three different grids. The grids are, from left to right, FGM-16, FGM-32, and FGM-64. The color scaling varies for each plot and is indicated by the colorbar in the upper right corner of each plot.

USCD mechanism [32] to model the combustion in PM1-50. The results obtained with these models are compared to results obtained using detailed chemistry with the two sets of boundary conditions described in Table 3.3; for FGM-AI, the results are compared to those with detailed chemistry and equilibrium boundary conditions, and for FGM-LF, to those with laminar flame boundary conditions with heat loss in the coflow. The results obtained with FGM-AI are in remarkably good agreement to the results obtained using detailed chemistry for the mean mass fractions of major species such as CH_4 and CO_2. For the mean mass fractions of CO and OH, the FGM-AI calculations are generally within 10% of the values from the calculation with detailed chemistry; FGM-AI slightly overpredicts the mass fractions of these species, which would suggest that diffusive processes are responsible for the slightly lower mass fractions of CO and OH observed in the calculations with detailed chemistry. The performance of FGM-LF is similar in terms of the mean mass fraction of CH_4 and CO_2, and is slightly more consistent with the calculations with detailed chemistry than that

of FGM-AI, in terms of the mean mass fractions of CO and OH. Figure 3.8 also shows that the differences between FGM-AI and FGM-LF are caused by both the combustion modeling as well as by the different boundary conditions. This thorough comparison of the simplified combustion models to detailed chemistry shows that the combustion in these calculations is not particularly sensitive in terms of the major species such as CH_4, O_2, H_2O, and CO_2, but for the species in smaller concentrations, like CO and OH, the results are slightly more sensitive to the combustion modeling.

The same calculations are performed in PM1-200, and the agreement in the mean and RMS species mass fractions between the calculations using detailed mechanisms and those using FGM-based modeling is of similar quality to that in PM1-50. However, the reaction progress in the calculations of PM1-200 is overpredicted using both chemistry models, so no strong conclusions about the adequacy of FGM-based models in PM1-200 can be drawn from that comparison.

With respect to other studies of the PPJB using simplified combustion modeling [51], these comparisons assist in validating the use of those models for the major species and density, and provide an explanation for the observed discrepancies in the mass fractions of CO and OH in those studies. One deficiency of the FGM investigated here is the inability to account for the heat loss in the coflow stream, which is one advantage of the approach used in [51]. This could be accounted for by adding an additional variable into the formulation. However, the objective of this part of the study is to describe the reaction progress as simply as possible; based on the previously discussed findings regarding the effect of the coflow temperature on the overall combustion in the flame, the re-

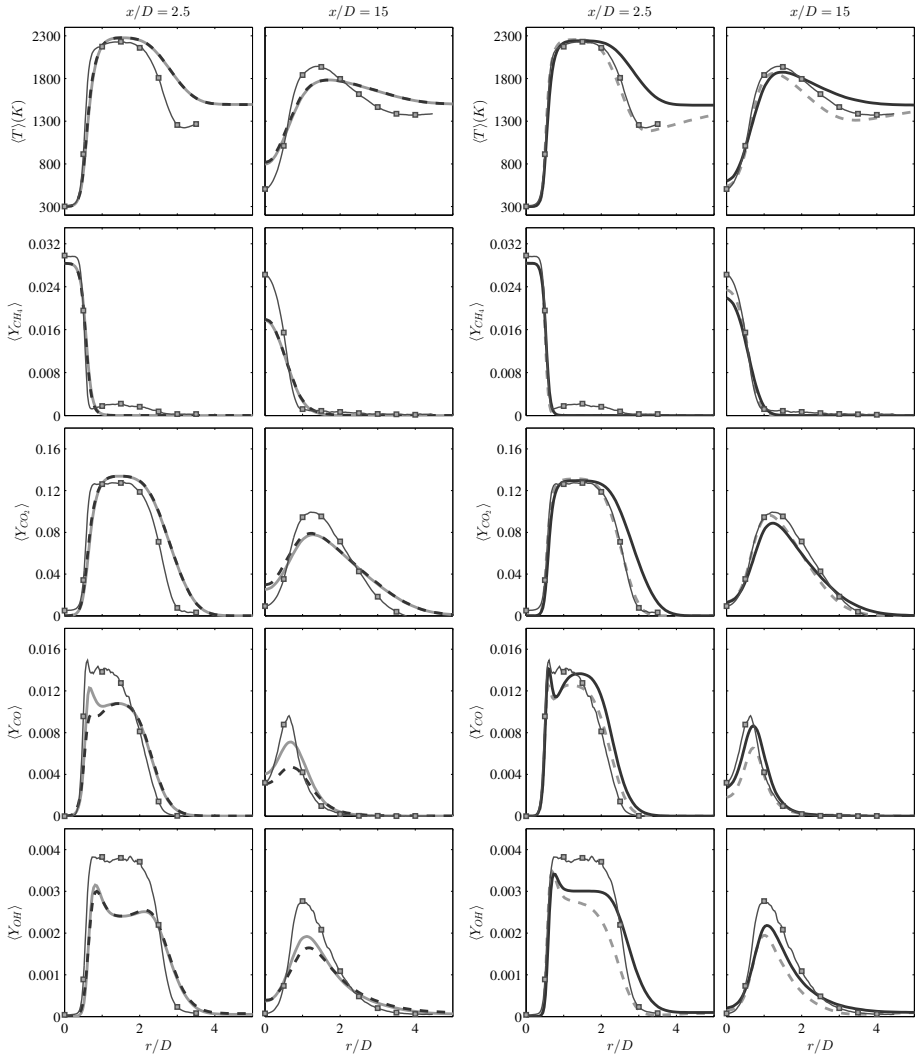

Figure 3.8: Radial profiles of (from top to bottom) time-averaged mass-weighted mean temperature, and time-averaged mass-weighted mean mass fractions of species CH_4, CO_2, CO, and OH in the RANS-PDF calculations of PM1-50 using different chemistry models and boundary conditions. Left-most two columns: equilibrium boundary conditions and chemistry modeled with: detailed chemistry using ARM-1 and ISAT (dark dashed lines) and FGM-AI (light solid line); Right-most two columns: laminar flame boundary conditions using: ARM-1 and ISAT (light dashed line) and FGM-LF (dark solid line); Lines with squares: experimental data [12].

sults using the FGM provide acceptable results. The FGM-LF model is selected to be used in the first LES-PDF in this work, before advancing to the calculations with detailed chemistry.

3.3 LES-PDF Calculations

The results from Sec. 2 show how the treatment of molecular diffusion, inflow boundary conditions, and chemistry modeling affect the calculations of the PPJB flames in the context of the RANS-PDF method, and the results demonstrate much more accurate calculations of PM1-50 than any previous study. However, none of these components of the modeling yield calculations of PM1-150 and PM1-200 in much better agreement to the experimental data. Therefore, the more complete modeling methodology of LES-PDF is next considered so that the effects of molecular diffusion can be examined in greater detail, and with a more complete level of turbulence modeling.

The LES-PDF methodology is a hybrid method in which large-eddy simulation (LES) and probability density function (PDF) methods are used together to model a turbulent reactive flow. In LES, the large scales of the turbulence are resolved, and the small scales must be modeled. Since the large scales contain most of the kinetic energy of the flow, most of the large-scale features of the flow can be resolved. However, most chemical reaction occurs at very small scales, so the sub-model used to describe this process is a very important part of the overall model. There are a number of existing sub-models for chemical reaction, among which is the PDF method. The primary advantage of the PDF method is that chemical reaction can be treated exactly through elemen-

tary reactions in a detailed chemical mechanism, and therefore can represent turbulence-chemistry interactions most effectively. Various formulations of the LES-PDF methodology have recently been used to perform calculations of turbulent flames [61–67]. The approach taken in this work is based on that used in [66,67] and is next described.

3.3.1 Computational Methodology for the LES-PDF Calculations

The LES-PDF approach used to study these flames is based on the LES framework of self-conditioned fields [68] and the two-way coupled hybrid method developed in [66,69,70]. The LES transport equations for mass and momentum are solved with overall second-order accuracy using the methodology of [71]; continuity is enforced through solving the pressure Poisson equation. The turbulent viscosity is computed using an algebraic sub-grid scale model [72], and the turbulent diffusivity is computed from the turbulent viscosity using a turbulent Schmidt number of 0.4. The effect of the turbulent Schmidt number on the calculations has been examined in PM1-150, and it is found that a 25% variation in this parameter has little effect on the calculations.

An additional equation for the specific volume is solved in the LES, and the source term for this equation is obtained from the particle solver [73]. The LES solver provides the particle solver with the filtered velocity, density, turbulent viscosity, turbulent diffusivity, molecular diffusivity, and mixing frequency.

As opposed to the RANS-PDF method, which considers the joint PDF of ve-

locity, turbulence frequency, and compositions, the LES-PDF method used here considers the joint PDF of compositions. In the particle solver, the particles evolve in physical space and in composition space. A splitting scheme with second-order accuracy [69] is used to advance the particles over each time step. The quantities from the LES solution are used to advance the particles in physical space as developed in [70] and also used in [66,67]. The particle composition evolves by Eq. 3.5,

$$\frac{d\phi^*(t)}{dt} = -\Omega_M^* \left(\phi^* - \tilde{\phi}^*\right) + \left(\frac{1}{\bar{\rho}} \nabla \left(\bar{\rho}\tilde{\alpha}\nabla\tilde{\phi}\right)\right)^* + \dot{S}\left(\phi^*\right), \tag{3.5}$$

where ϕ is the particle composition vector, Ω_M is the mixing frequency, $\bar{\rho}$ is the filtered density, $\tilde{\alpha}$ is the mass-weighted filtered diffusivity, and $\dot{S}$ is the reaction source term. The superscript "$*$" denotes a quantity evaluated at the particle position. The first two terms in Eq. 3.5 represent the modeling of mixing, the first term being molecular mixing, and the second term being molecular transport. This treatment of molecular diffusion allows differential diffusion to be accounted for in the model, and it produces no spurious scalar variance [57,58]. The mixing frequency is computed from Eq. 3.6,

$$\Omega_M = C_M \left(\tilde{\alpha} + \alpha_T\right) / \Delta^2, \tag{3.6}$$

where α_T is the turbulent diffusivity, Δ is the filter width, and the constant mechanical-to-scalar timescale ratio, C_M, is set to a value of 5.0 for the base case, as in [67]. The constant C_M is often denoted by C_ϕ. However, here the symbol C_M is used to differentiate this constant from the mechanical-to-scalar timescale ratio used in the RANS-PDF calculations, C_ϕ.

The third term in Eq. 3.5 represents chemical reaction, and here it is evalu-

ated using the ISAT storage and retrieval algorithm [20,21] for computational efficiency. Upon completion of the current time step, the particle solver then provides the LES solver with the volume-weighted mean density, mass-weighted mean temperature, and source term for specific volume. The two-way coupled hybrid method proceeds in this way throughout the calculation. After a statistically stationary state has been reached, the statistics of interest are time-averaged until temporal convergence is attained.

3.3.2 Computational Configuration of the LES-PDF Calculations

The computational domain for the LES-PDF calculations is a cylinder of size $75D \times 25D \times 2\pi$ in the axial, radial, and circumferential directions. A sketch is shown in Figure 3.9. At the pilot and coflow inflow plane, the velocity boundary conditions are prescribed based on the laminar flow identical to the mean velocity used in the RANS-PDF calculations. At the jet inflow plane, the velocity is taken from a separate turbulent pipe-flow simulation at the appropriate value of Re.

The same chemical mechanism used in the RANS-PDF calculations, the 16-species ARM-1 mechanism [26], is used to describe the detailed chemical kinetics in the base case. The compositions provided at the inlet are taken from the laminar flame inflow conditions in Table 3.3; however, the temperature and density at the inlet are specified using the boundary conditions with heat loss in the coflow. The viscosity is obtained from a curve-fit to data from the FGM. For each composition realized in the FGM, the kinematic viscosity, ν, is evaluated

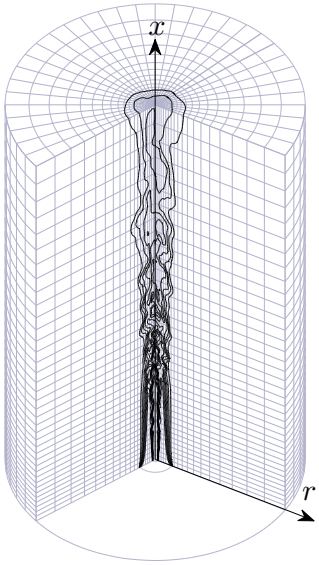

Figure 3.9: Computational domain for the LES-PDF calculations. The axial and radial directions are indicated by the arrows, and the vertical arrow coincides with the centerline of the jet. Only one fifth of the grid points from grid G3 are shown in each axial and radial direction. The cutaway in the $x - r$ plane shows a contour of the instantaneous resolved CO_2 mass fraction from a calculation of PM1-100. In the plane at the bottom of the cutaway, the diameter of the pilot and jet are shown.

with Chemkin, and a curve-fit is made as a function of temperature by

$$\nu(T) = \nu_0 \, (T/T_0)^b \, , \tag{3.7}$$

where the reference temperature, T_0, is 300 K, and the reference viscosity is, ν_0, 1.60×10^{-5} m^2/s. The exponent b is obtained from the curve-fit and is equal to 1.69. The base case is set up with unity Lewis number in all the species, and the diffusivity is evaluated in the same way as described for the RANS-PDF equations, using Eq. 3.2 and all the same parameter values. The case of differential

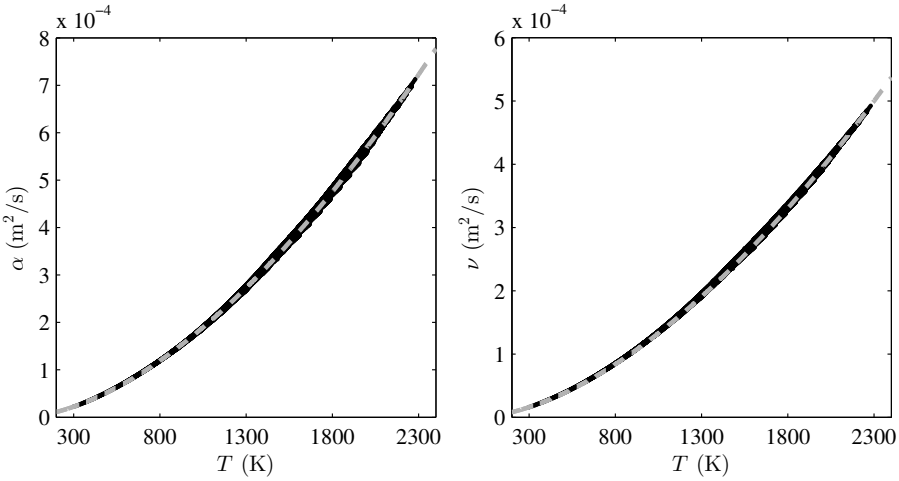

Figure 3.10: Molecular transport properties as prescribed in LES-PDF calculations as functions of temperature. The thermal diffusivity is shown in the left plot, and the kinematic viscosity is shown in the right plot. In both plots, the black dots indicate the transport properties as evaluated on the FGM, and the gray dashed lines indicate the curve-fits used to Eqs. 3.2 and 3.7 that are prescribed in the LES-PDF calculations.

diffusion is discussed in Sec. 3.4.1. Figure 3.10 shows both the molecular diffusivity and the kinematic viscosity as evaluated on all the compositions throughout the FGM as functions of temperature. Both the viscosity and the diffusivity are well-described as a function of only the temperature, and the curve-fits provided to Eq. 3.2 and Eq. 3.7 represent these transport properties well.

The calculations are performed for all four PPJB flames using this formulation of the base case. Figure 3.11 shows contours of instantaneous resolved mass fraction of CO from these calculations. As the jet velocity increases, the coflow and pilot streams are more rapidly entrained by the central jet, and the length of the flame generally increases.

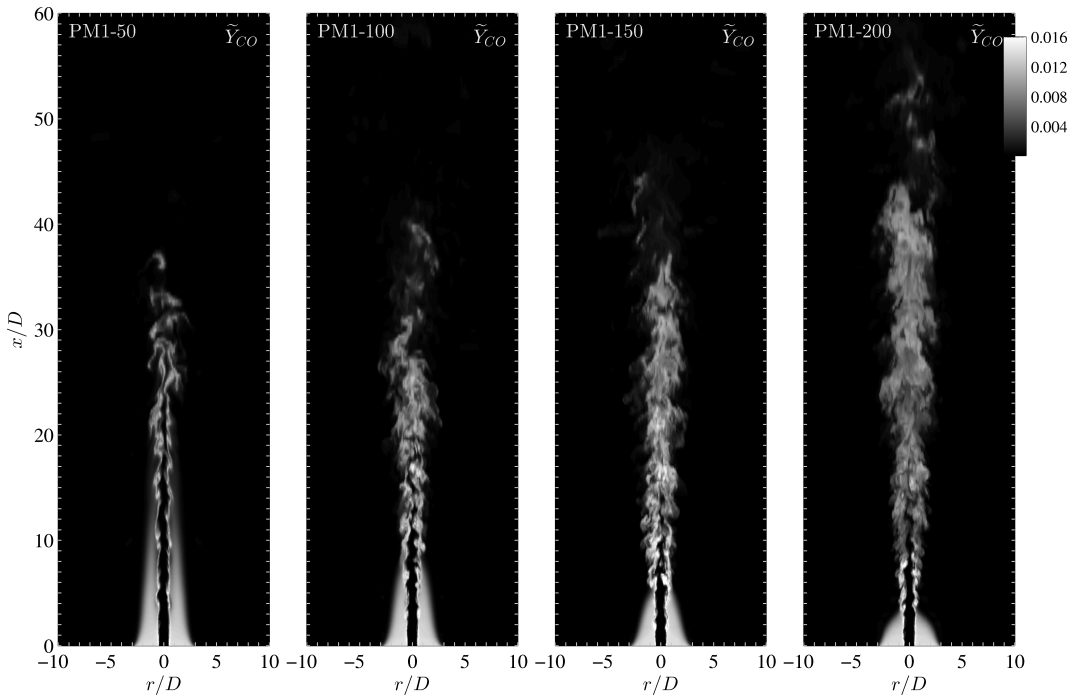

Figure 3.11: Contour plots of instantaneous fields of resolved *CO* mass fraction from LES-PDF calculations of all four PPJB flames on grid G4 using the mechanism ARM-1 to describe the chemistry.

3.3.3 Numerical Accuracy of the LES-PDF Calculations

In the LES-PDF calculations, the primary sources of numerical error include the grid discretization, the finite number of particles, the finite duration of time-averaging, and the error tolerance associated with the chemistry tabulation in ISAT. All of these parameters are investigated through convergence studies, and it is found that the largest source of numerical error is the grid resolution. The grid resolution is especially important in the context of LES, where the resolution directly affects the filter width, and thus, how much of each quantity is either resolved or unresolved. A number of different criteria exist for determining the grid quality for a LES, and there is still no universal standard criterion

by which to assess the quality. This remains an important topic for future study, but is beyond the scope of this work, other than to ensure that the investigated quantities do not exhibit significant sensitivity to the grid resolution beyond that used. Therefore, to establish the level of numerical accuracy of the calculations with respect to the grid resolution, several convergence studies are performed on progressively refined grids. The statistics of interest for each calculation are then compared to those statistics on the most highly resolved grid and the error for each statistic on each grid is measured.

The first set of convergence studies is conducted on a non-reacting flow based on the same configuration as the PPJB. Only a single LES is necessary for these calculations; there is no chemical reaction source term, and the density can be obtained directly from the mixture fractions. The grid sizes used for these calculations are shown in Table 3.5. The relative number of cells in each direction is chosen based on the configuration which yields the most rapid grid convergence. The results of this convergence study are summarized in Table 3.5 for the flow NR-200, which is based on PM1-200, the PPJB flame with the highest jet bulk velocity. Among all the flows considered in this work, NR-200 has the largest numerical error from grid resolution. The error in the time-averaged statistics for each calculation is computed by taking the difference between the statistics in that calculation and the statistics on the most highly resolved grid; the maximum error in time-averaged mass-weighted statistics at an axial location of x/D of 30 is shown in Table 3.5. On grid G4, The maximum error at x/D of 30 is about 5% for the resolved mean axial velocity, 1% for RMS of the resolved axial velocity, 4% for the resolved mean jet mixture fraction, and 1% for the RMS of the resolved jet mixture fraction.

Grid Name	n_x	n_r	n_θ	n_T (MCells)	NR-200 $\widetilde{U}$	NR-200 u_{RMS}	NR-200 $\widetilde{\xi}_j$	NR-200 $\widetilde{\xi}_j''$
G1	96	48	24	0.11	0.104	0.102	0.130	0.041
G2	128	64	32	0.26	0.152	0.031	0.128	0.033
G3	192	96	48	0.88	0.108	0.022	0.082	0.024
G4	256	128	64	2.1	0.044	0.006	0.040	0.011
G5	384	192	96	7.1	–	–	–	–

Table 3.5: Grid sizes for LES and LES-PDF calculations. Shown in each column are the grid name, the number of cells in the axial, radial, and angular directions (n_x, n_r, and n_θ), and the total number of cells (n_T), in millions of cells. The next four columns show the errors in the time-averaged mass-weighted resolved mean axial velocity, resolved RMS axial velocity, resolved mean jet mixture fraction, and resolved RMS of the jet mixture fraction for the grid convergence study of the non-reacting flow based on PM1-200. The final six columns show the error in the time-averaged mass-weighted resolved mean jet and pilot mixture fractions, resolved RMS jet and pilot mixture fractions, and the resolved mean and RMS temperature. All errors are evaluated as the maximum difference at x/D of 30 between statistics on the evaluated mesh and the finest mesh examined.

A grid convergence study is also performed for the reacting flows. The results of the grid convergence study for PM1-50 are also summarized in Table 3.5. These reacting flow calculations have considerably less numerical error from the grid resolution than do the non-reacting cases; due to the heat-release in the reacting flows, the pilot and coflow streams are not entrained as strongly into the jet as they are in the non-reacting flows. Grid G3 exhibits errors of around 2% for the mean and RMS of the resolved temperature and jet and pilot mixture fractions. Figures 3.12 (a) and (b) show the radial profiles of the mean and RMS statistics for this convergence study. Besides grid G1, the other grids all yield reasonably similar statistics. The largest numerical errors occur in the RMS statistics of the resolved scalar fields around the centerline. It is observed

that as the jet velocity increases, the requirements for numerical accuracy also increase. Grid G3 is used as the base case grid for the calculations of PM1-50, while both grids G3 and G4 are used to perform calculations of the other flames, PM1-100, PM1-150, and PM1-200.

Figures 3.13 (a) and (b) show the mean and RMS statistics in the base case calculations of PM1-50. The figures demonstrate good consistency between the mean scalar fields in the RANS-PDF and LES-PDF calculations, and an improvement in the calculations of the RMS statistics in the LES-PDF calculations in the near-field region of the pilot-coflow mixing layer. The use of the boundary condition with heat loss significantly improves the calculations of the temperature throughout the flame, and does yield a small improvement in the amount of fuel burned near the centerline farther down in the flame, as is also seen in the RANS-PDF study. The total RMS as obtained from the particles and is shown in Figure 3.13 (b). At the jet-pilot interface, the unresolved component of the RMS accounts for about 30% of the total RMS at x/D of 2.5, and about 20% of the total RMS at x/D of 7.5. Beyond x/D of 7.5, the unresolved component of the RMS is generally less than 10% of the total RMS.

3.3.4 The Effects of Modeling Molecular Diffusion in the LES-PDF Calculations

In LES-PDF, modeling is required to treat the conditional diffusion term in the PDF transport equation. This is done through the mixing model described above in Eqs. 3.5 and 3.6, and entails one of the largest sources of modeling uncertainty in the calculations. For that reason, a thorough investigation is per-

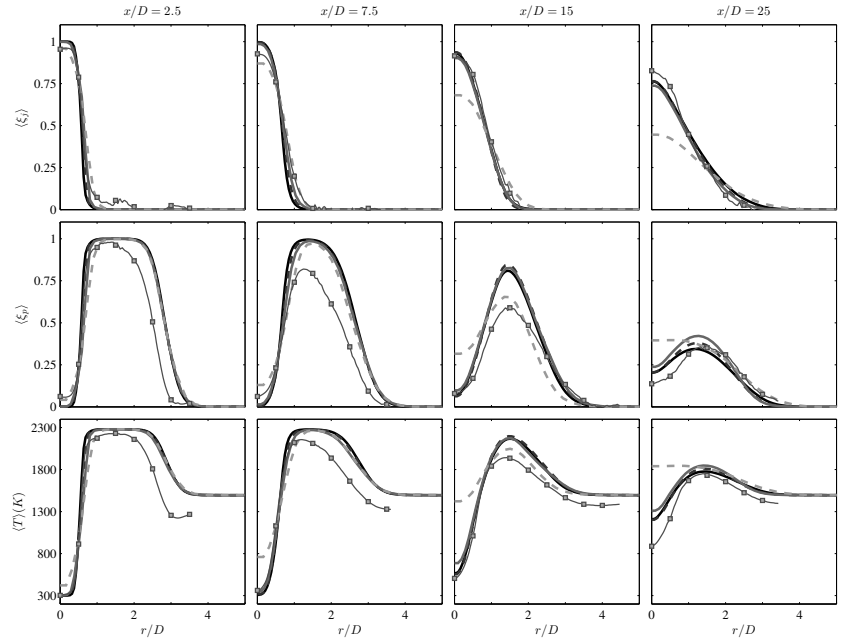

(a)

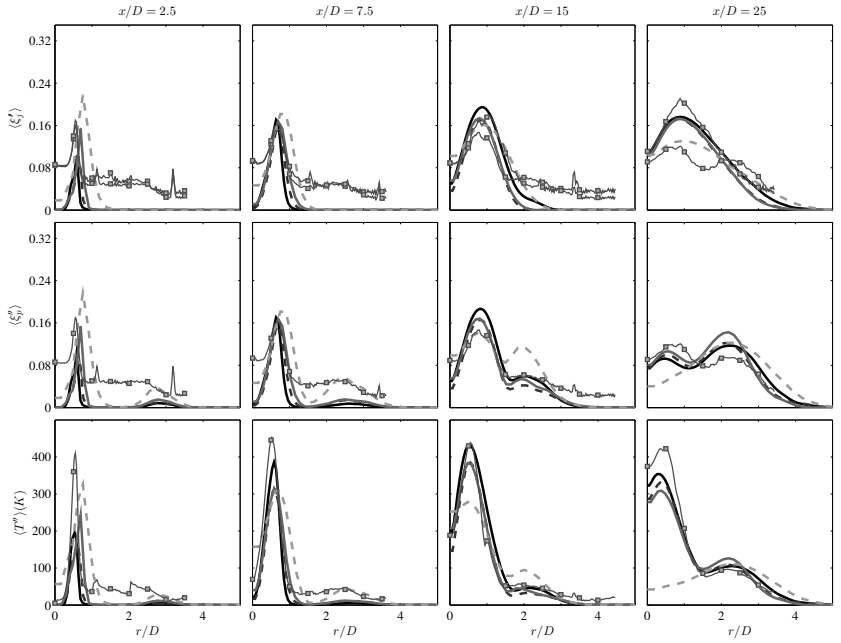

(b)

Figure 3.12: Radial profiles of the time-averaged mass-weighted resolved mean (a) and RMS of the resolved scalar (b) for the jet mixture fraction (top row), pilot mixture fraction (middle row), and temperature (bottom row) in the convergence study of the LES-PDF calculations of flame PM1-50. The axial location is indicated at the top of each column. Dashed light gray: G1; Solid gray: G2; Dashed dark gray: G3; Solid black: G4; Lines with squares: experimental data [12].

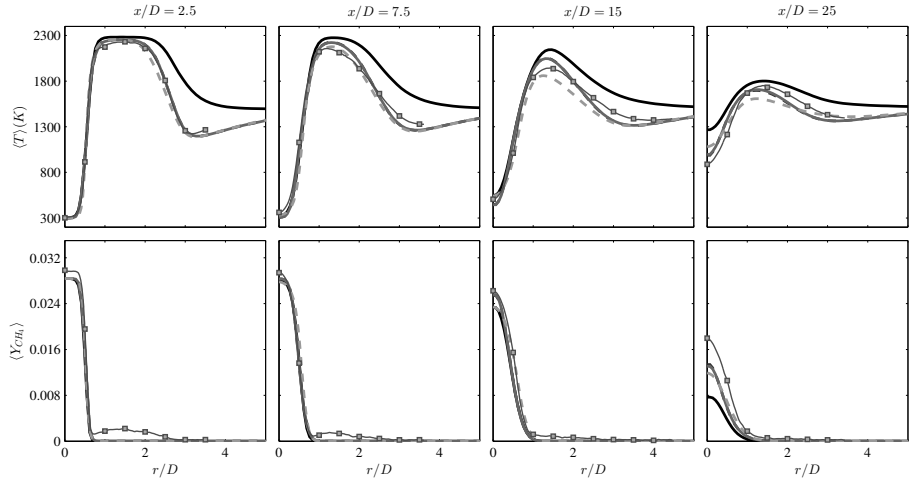

(a)

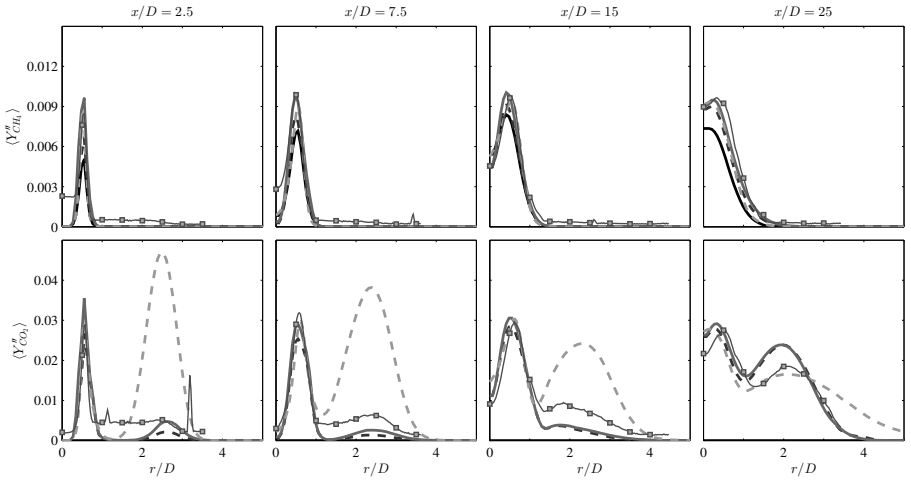

(b)

Figure 3.13: Radial profiles of the time-averaged mass-weighted resolved mean (a) and RMS statistics in the base case LES-PDF and RANS-PDF calculations of flame PM1-50. Dark solid line: LES-PDF without heat loss; Gray solid line: LES-PDF with heat loss (total RMS); Gray dashed line: LES-PDF with heat loss (RMS of resolved scalar); Light gray dashed line: base case RANS-PDF; Lines with squares: experimental data [12].

formed with respect to two aspects of the mixing model. The first aspect investigated is the effect of differential diffusion, and the second aspect investigated is the value of the parameter, C_M, which represents the mechanical-to-scalar timescale ratio.

The Effects of Differential Diffusion

A major assumption made in the base-case calculations, as well as in the previously discussed RANS-PDF calculations, is that the Lewis number is unity for all chemical species. In reality, this is not the case, as lighter species generally have a higher diffusivity, and heavier species generally have a lower diffusivity. In the configuration of the PPJB, there are significant concentrations of light species such as OH, H_2, and H in both the pilot and coflow. Furthermore, it has already been shown that molecular diffusion is important in modeling the pilot-coflow mixing due to the low velocities and high temperatures of the pilot and coflow streams. Therefore, a careful investigation of the effect of differential diffusion in these flames is important in understanding their behavior.

Figure 3.14 shows the molecular diffusivity of each chemical species in the ARM-1 mechanism evaluated throughout the entire FGM manifold, as well as the thermal diffusivity. From the figure, it is clear that there is a large range in the diffusivity of the different species. The lightest species, H, has a diffusivity larger than the thermal diffusivity by a factor of about eight, and that of H_2 is about four times greater than the thermal diffusivity. Figure 3.14 also shows that the diffusivity of each species is well-described as a function of only the temperature.

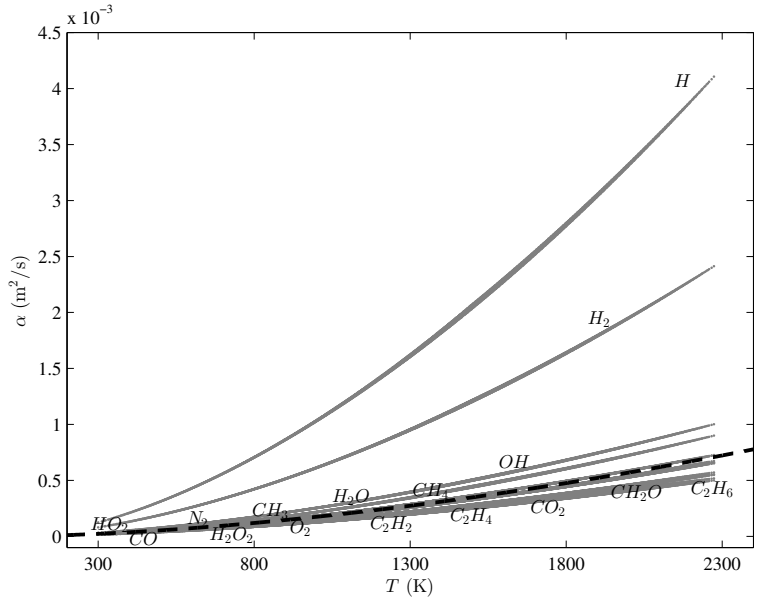

Figure 3.14: Molecular diffusivity of the chemical species in the ARM-1 mechanism as evaluated from compositions on the FGM and plotted as functions of temperature. The curve-fit to Eq. 3.2 for the thermal diffusivity is shown by the black dotted line.

Using the diffusivities evaluated on the FGM, as shown in Figure 3.14, curve-fits are made as functions of temperature in the form of Eq. 3.8,

$$\alpha^i(T) = \alpha_0^i \, (T/T_0)^{b^i} \,, \tag{3.8}$$

which is identical in form to Eq. 3.2, but the superscript "i" denotes a quantity for species i. The values obtained from the curve-fit for each species are shown in Table 3.6.

A comparison between calculations with and without differential diffusion in flame PM1-50 is shown in Figure 3.15. The general conclusion is that the effects of differential diffusion are limited to the near-field of the flow (around x/D of 2.5 and 7.5) and to the species H_2, CO, and OH, as well as other species in smaller concentrations. There is interesting behavior observed in the near-

Species	$\alpha_0(\mathrm{m}^2/\mathrm{s})$	b
H_2	8.00×10^{-5}	1.69
H	12.4×10^{-5}	1.75
O_2	2.03×10^{-5}	1.73
OH	3.22×10^{-5}	1.71
H_2O	2.27×10^{-5}	1.85
HO_2	2.09×10^{-5}	1.72
H_2O_2	2.07×10^{-5}	1.72
CH_3	2.26×10^{-5}	1.73
CH_4	2.30×10^{-5}	1.71
CO	2.08×10^{-5}	1.71
CO_2	1.58×10^{-5}	1.75
CH_2O	1.56×10^{-5}	1.80
C_2H_2	1.67×10^{-5}	1.74
C_2H_4	1.61×10^{-5}	1.76
C_2H_6	1.48×10^{-5}	1.75
N_2	2.17×10^{-5}	1.70

Table 3.6: Coefficients in Eq. 3.8 for the diffusivity of each chemical species, relating the mixture-averaged diffusivity of each species to the temperature, as evaluated from curve-fits evaluated on compositions throughout the entire flamelet manifold.

field of the flow to which the differential diffusion gives considerable insight. The most notable difference in the calculations with and without differential diffusion is in the mean mass fraction of CO. When differential diffusion is included in the calculations, the amount of CO in the pilot-coflow mixing layer decreases to a value closer to that measured. This occurs not because of the diffusivity of CO (which is roughly equal to the thermal diffusivity), but rather because of the diffusivity of the other light species in the coflow and pilot. When differential diffusion is included, a greater concentration of these lighter species react with CO to form CO_2 in the pilot-coflow mixing layer, and thus the mass fraction of CO there is reduced. In addition to flame PM1-50, the same study of differential diffusion is applied in flame PM1-150; this yields a similar effect, but

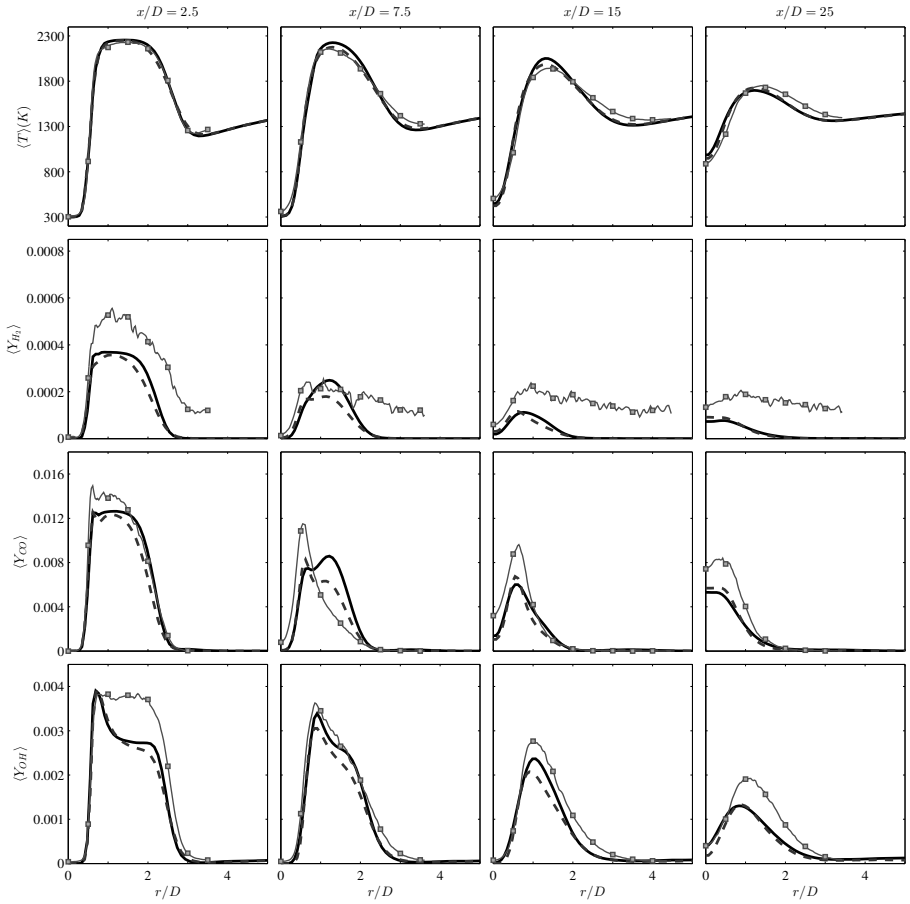

Figure 3.15: Radial profiles of time-averaged mass-weighted resolved scalars in calculations of PM1-50 with and without differential diffusion. The first row shows the temperature, the next three rows show the mass fraction of the species H_2, CO, and OH. Solid dark line: Without differential diffusion; Dashed gray line: with differential diffusion; Lines with squares: experimental data [12].

of smaller magnitude. This observation is reasonable because the pilot-coflow region is much smaller in flame PM1-150 due to the more rapid entrainment by the jet, and the effect of differential diffusion is primarily limited to this region.

The Effect of the Model Constant C_M

The second important aspect of modeling molecular diffusion is the value of the parameter C_M. The mixing frequency, from Eq. 3.6, is directly proportional to C_M. In previous RANS-PDF calculations of the PPJB, it is found that the value of C_ϕ had two main effects: larger values of C_ϕ result in decreased scalar variance [12, 46] and a decreased spreading rate of the jet [46]. In this study, the value of C_M is varied over values of {2, 5, 10, 20, 50, 100} for flame PM1-150. The numerical implementation with a second-order scheme where the boundedness for ϕ is guaranteed [58, 69] ensures that there are no numerical accuracy or stability issues for large values of C_M. Contour plots of the instantaneous CO mass fraction from this parameter study are shown in Figure 3.16. As C_M increases, the flame length increases and the spatial variance of the resolved fields decreases.

Figure 3.17 shows the effect of C_M on the fraction of the time-averaged mass-weighted total RMS of the CO mass fraction which is unresolved. In the base case calculations of PM1-150, the maximum unresolved RMS is about 30% of the total RMS in the near-field (from $x/D = 0$ to $x/D = 15$), and less than 20% beyond $x/D = 15$. As C_M increases, the unresolved portion of the total RMS decreases; for $C_M \geq 20$, the unresolved RMS is less than 5% of the total RMS at all locations at which the total RMS is significantly large (values of the total RMS at least 2% of the RMS at the centerline). The observations about the unresolved RMS made for the CO mass fraction generally hold true for the mass fractions of other species. A second observation from Figure 3.17 is that as the constant C_M increases, the total RMS decreases and its distribution in physical space changes. As C_M increases, the peak in the total RMS of the CO mass fraction moves out

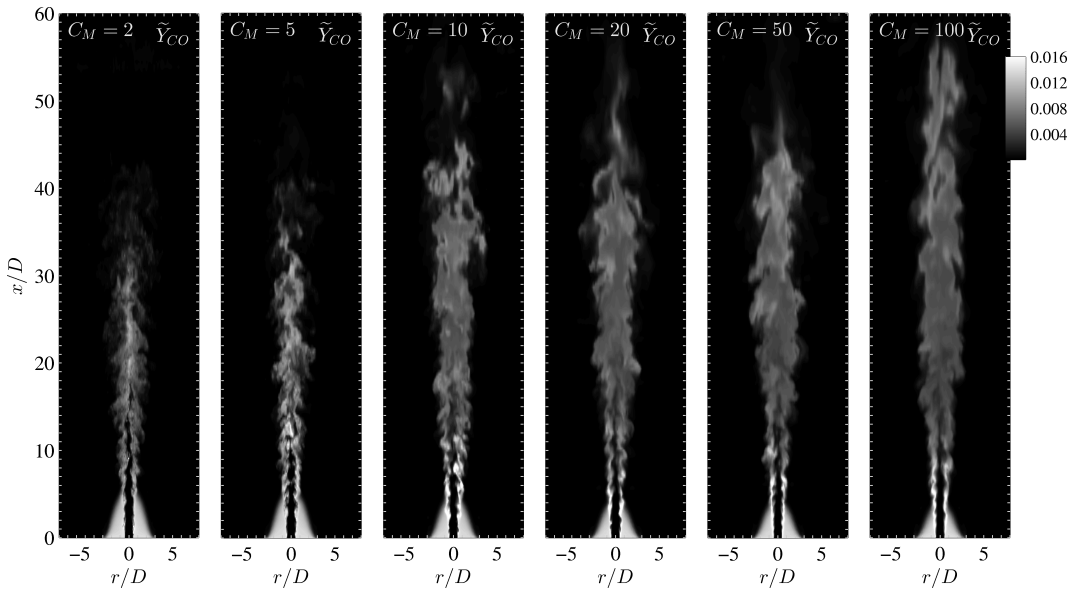

Figure 3.16: Contour plots of instantaneous resolved mass fraction of CO in the parametric study of C_M for flame PM1-150. The value of C_M used in each calculation increases from 2 to 100 going from left to right, and is indicated in the top left corner of each plot. The value of the resolved CO mass fraction is indicated by the colorbar in the top right corner.

from the centerline. This is a result of the changing shape of the flame caused by C_M. With larger C_M, the flame has more homogeneity near the centerline due to the increased intensity of mixing. Most of the strong gradients in physical space move outward from the centerline, and most mixing takes place at these locations.

The results of this parameter study are illustrated quantitatively in Figures 3.18 and 3.19. Figure 3.18 shows the time-averaged mass-weighted mean of the resolved temperature and species mass fractions for values of C_M of 5, 20, and 50. As C_M increases, the fuel mass fraction increases at x/D of 15 and 30. When C_M is increased to around 50 or 100 (not shown), very good agreement in the overall reaction progress is obtained by x/D of 15 and 30. This includes both

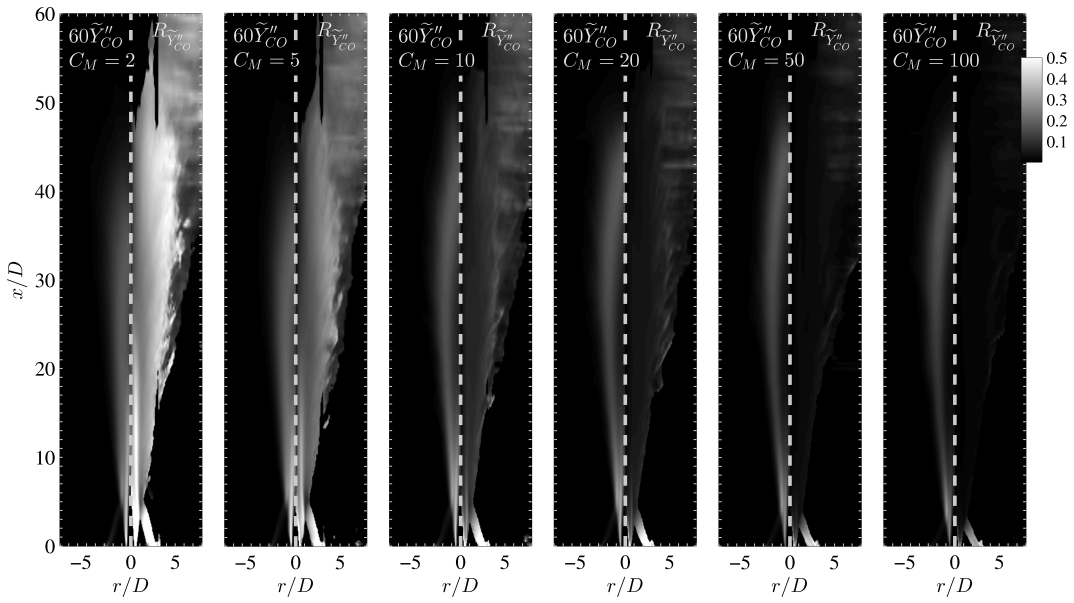

Figure 3.17: Contour plots of time-averaged mass-weighted total RMS of CO mass fraction (left side) and portion of the total RMS which is residual, $R_{\widetilde{Y}''_{CO}}$, (right side) in the parametric study of C_M for flame PM1-150. The quantity $R_{\widetilde{Y}''_{CO}}$ is defined as the time-averaged mass-weighted residual RMS mass fraction of CO divided by the time-averaged mass-weighted total RMS mass fraction of CO. The magnitude of the total RMS (left side) is multiplied by a factor of 60 so one colorbar is used to show the magnitude of both quantities.

the mean and RMS statistics. However, for the near-field region, smaller values around 5 or 10 yield results in better agreement with the experimental measurements. For axial locations beyond x/D of 30, it appears that even larger values of the mixing frequency are required; however, simply using a larger value of C_M does not improve the accuracy of the calculations beyond x/D of 30 due to the adverse effect of larger values of C_M in the near-field of the jet.

Increasing the mixing frequency (via increasing C_M) effectively reduces the residual variance. Figure 3.19 shows that the unresolved portion of the RMS is significant in the near-field when C_M is 5, and the total RMS is overpredicted

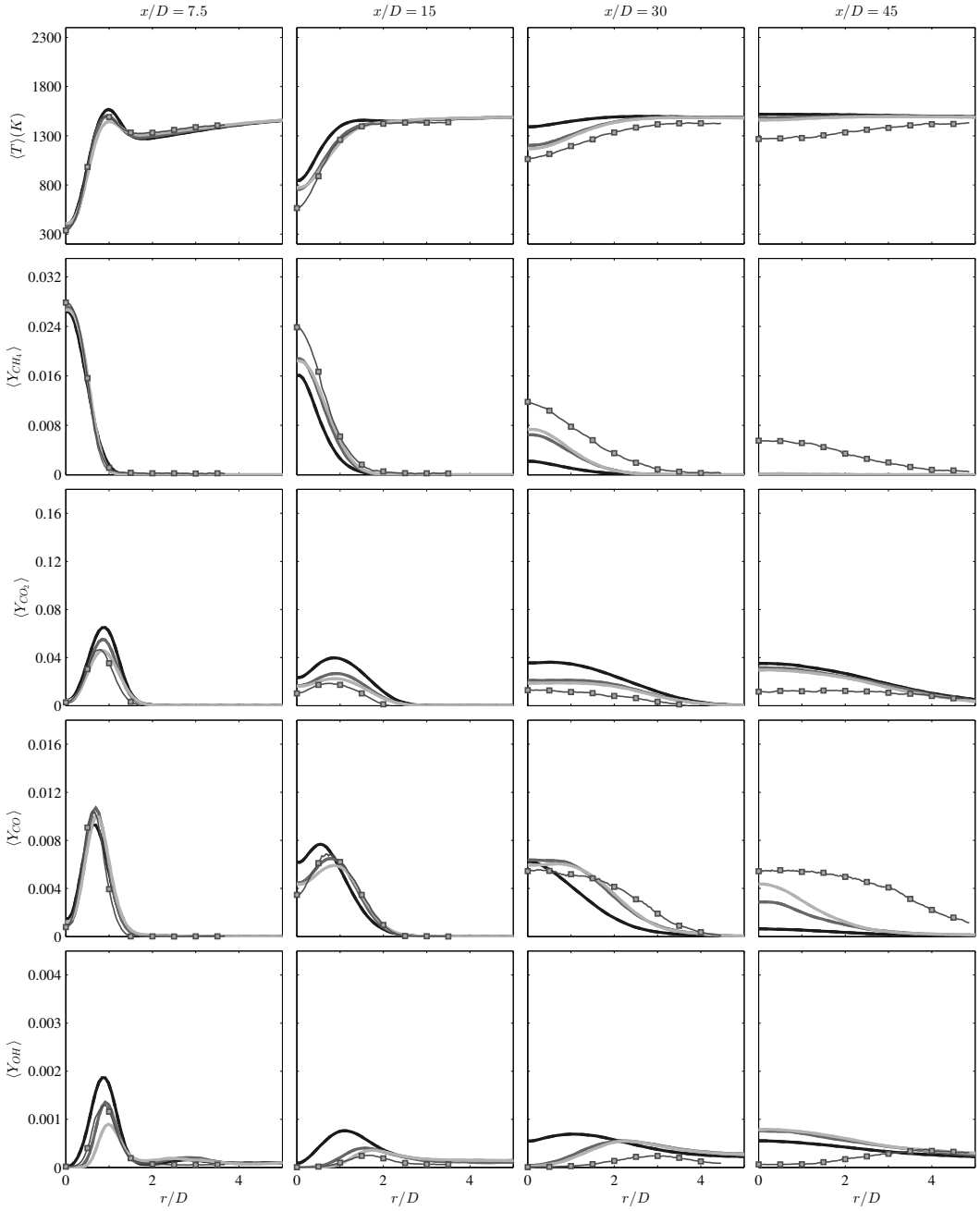

Figure 3.18: Radial profiles of time-averaged mass-weighted mean resolved scalars in the parametric study of C_M in flame PM1-150. The plotted scalars are, from top row to bottom row, temperature and mass fractions of the species CH_4, CO_2, CO, and OH. Black line: C_M = 5; Dark gray line: C_M = 20; Light gray line: C_M = 50; Lines with squares: experimental data [12].

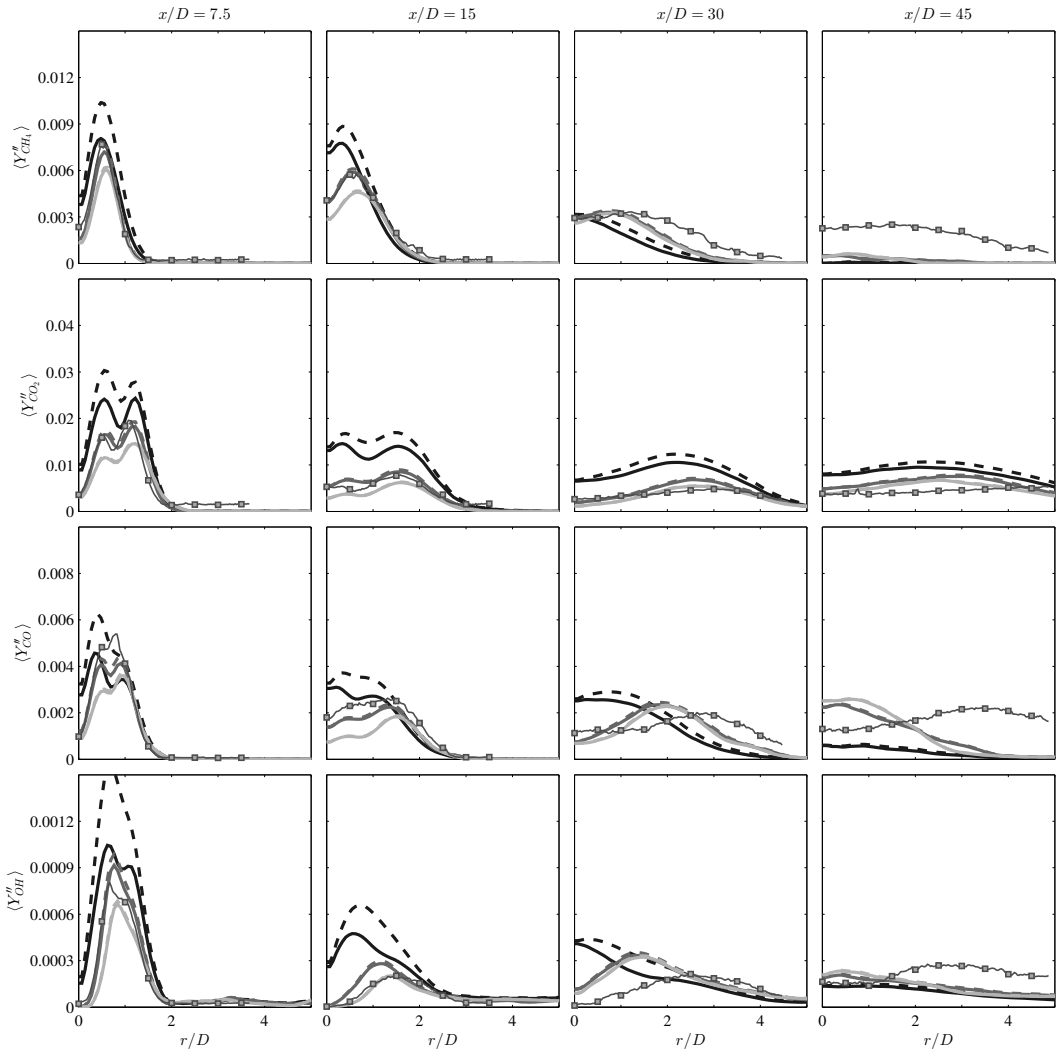

Figure 3.19: Radial profiles of time-averaged mass-weighted RMS of resolved scalars and total RMS (RMS of resolved fields and residual RMS) in the parametric study of C_M in flame PM1-150. The plotted scalars are, from top row to bottom row, temperature and mass fractions of the species CH_4, CO_2, CO, and OH. Black line: $C_M = 5$; Dark gray line: $C_M = 20$; Light gray line: $C_M = 50$; Solid lines: RMS of resolved scalars; Dashed lines: total RMS; Lines with squares: experimental data [12].

for the mass fractions of all these species in the near-field. As C_M increases, the unresolved portion of the RMS decreases, and larger values of C_M produce results of the total RMS much more consistent with the experimental data.

Figure 3.20 shows particles from a single row of cells in this parametric study. When C_M is 5, the base case, there is a very large amount of residual variation in the temperature, with variation as large as 500 K near the jet-pilot reaction zone. As C_M increases, this residual variation in the particle quantities clearly decreases, as shown in Figure 3.20. When C_M is 20, the maximum variation in the pilot-jet reaction zone is only about 300 K, and when C_M is increased to 100, the maximum variation at this location further diminishes to about 200 K. The framework used in the LES calculations in [48] should be examined carefully in light of the significant amount of subgrid-scale variation observed here.

3.4 Comparison of RANS-PDF and LES-PDF for all Flames

One of the major deficiencies of previous calculations is the overprediction of the reaction progress, particularly in the flames with higher jet velocities (i.e., PM1-150 and PM1-200) [12, 46]. Even in calculations of PM1-100, all previous studies report the flame length being calculated as shorter than measured experimentally [12,46,48–51]. This discrepancy is generally manifested in the calculations by accurate mean mixture fractions, underpredicted mass fractions of fuel and oxidizer, and overpredicted mass fractions of products (CO_2 and H_2O) and mean temperature. Considering that one of the main features of these flames is the reduced reaction progress in PM1-150 and PM1-200 around x/D of 30, the ability to predict the reaction progress rate accurately at this location is ex-

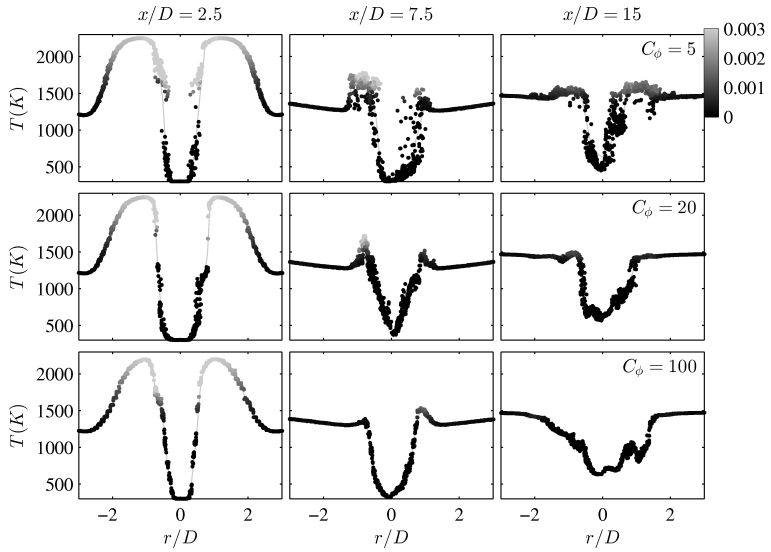

(a)

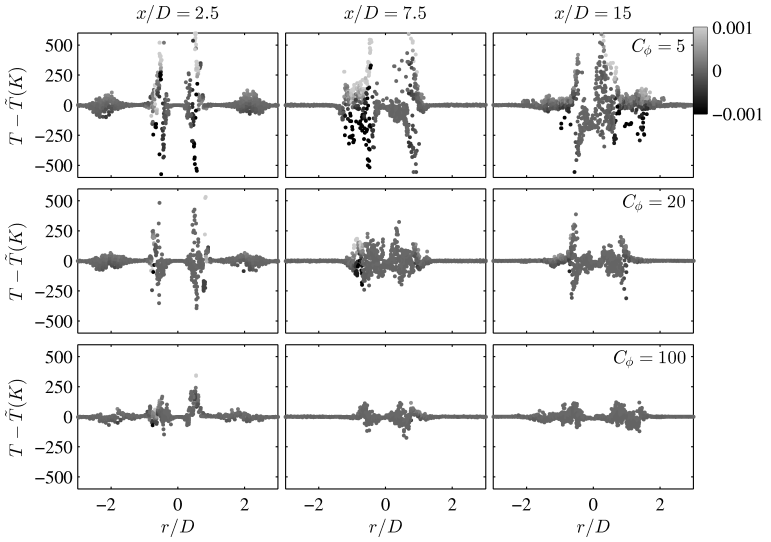

(b)

Figure 3.20: Radial profiles of instantaneous particle quantities from the parametric study of C_M from flame PM1-150. The topmost three rows (a) show the temperature of the particles, and the bottommost three rows (b) show the temperature deviation from the cell mean temperature for the same particles. Each row shows results from calculations using a different value of C_M: 5 (top), 20 (middle), and 100 (bottom). The particles in (a) are colored by the particle CO mass fraction, and the particles in (b) are colored by the deviation of the CO mass fraction from the cell mean CO mass fraction.

tremely important in assessing the quality of the numerical methods used to model these flames.

Some previous studies [12,46] identify the mixing models as the most likely cause of the observed discrepancy in reaction progress. However, neither of those previous studies shows, quantitatively, that a different model of mixing yields the observed reaction progress in PM1-150 or PM1-200. One of the major reasons is that, in those previous RANS-PDF studies based on the joint PDF of velocity, turbulence frequency, and composition [46], variation of C_ϕ affected not only the reaction progress, but also the scalar flux. Thus, the jet spreading rate is altered by the change in C_ϕ and quantitative agreement with the experimental measurements is not achieved for larger values of C_ϕ. However, in the LES-PDF parameter study of C_M performed in this work, the scalar flux is not directly affected by the value of C_M. For sufficiently large C_M, excellent quantitative agreement can be achieved at x/D of 30 in PM1-150 for mean and RMS statistics. These results demonstrate a clear link between the mixing frequency and the reaction progress. Given that such large values of C_M are required to achieve the correct reaction progress, this study is highly suggestive that the mixing frequency in this region of the PPJB flames is dominated by scales other than those in Eq. 3.6.

To quantify the amount of reaction progress in a way that allows an efficient comparison to experimental data, a mean Fuel Consumption Index (FCI) is introduced, which is defined as

$$FCI(x,r) = 1 - \frac{\langle Y_{fuel}(x,r)\rangle / \langle \xi_j(x,r)\rangle}{Y_{fuel}(x_0,r_0)/\xi_j(x_0,r_0)}, \tag{3.9}$$

where Y_{fuel} is the mass fraction of the fuel, and x_0 and r_0 are the axial and radial location of the origin of the fuel stream. The quantity FCI represents the mean

mass fraction of fuel that has burned relative to the amount the jet has been mixed. So, a value of 0 represents an entirely unburned composition, and a value of 1 represents a fully burned composition. One disadvantage of using the FCI as defined in Eq. 3.9 is that it is only defined on the centerline, so it only represents a small portion of the flow domain and it is subject to considerable statistical error in the measurements. Therefore, comparisons of this quantity must consider these factors as well. The experimental data demonstrates errors around 10-20% in FCI at some locations, based on unrealizable mass fractions and mixture fractions.

Figure 3.21 shows the evolution of this quantity along the jet centerline in the RANS-PDF calculations, LES-PDF calculations, and experiments. The obvious deficiency observed in many of the previous studies, as well as in this study, is observable in Figure 3.21 as the excessively rapid consumption of fuel in the calculations of PM1-150 and PM1-200. The improvement obtained through larger values of C_M is observable in Figure 3.21 (c) for PM1-150, although it is clear that there is still room for improvement in the prediction of this quantity.

The primary benefits of using the LES-PDF methodology over RANS-PDF in this work have been to model the molecular diffusion without spurious variance production, to examine the effect of differential diffusion, and to investigate the effect of C_M without significant effect on the scalar flux. The more complete turbulence modeling of LES-PDF yields slightly more accurate spreading of the pilot stream, and there is no dependence on turbulence model parameters such as $C_{\omega 1}$; but generally in this jet flow of simple geometry, both the RANS-PDF and LES-PDF calculations yield similar descriptions of the velocity fields. The computational costs of each approach is outlined in Table 3.4 for various case

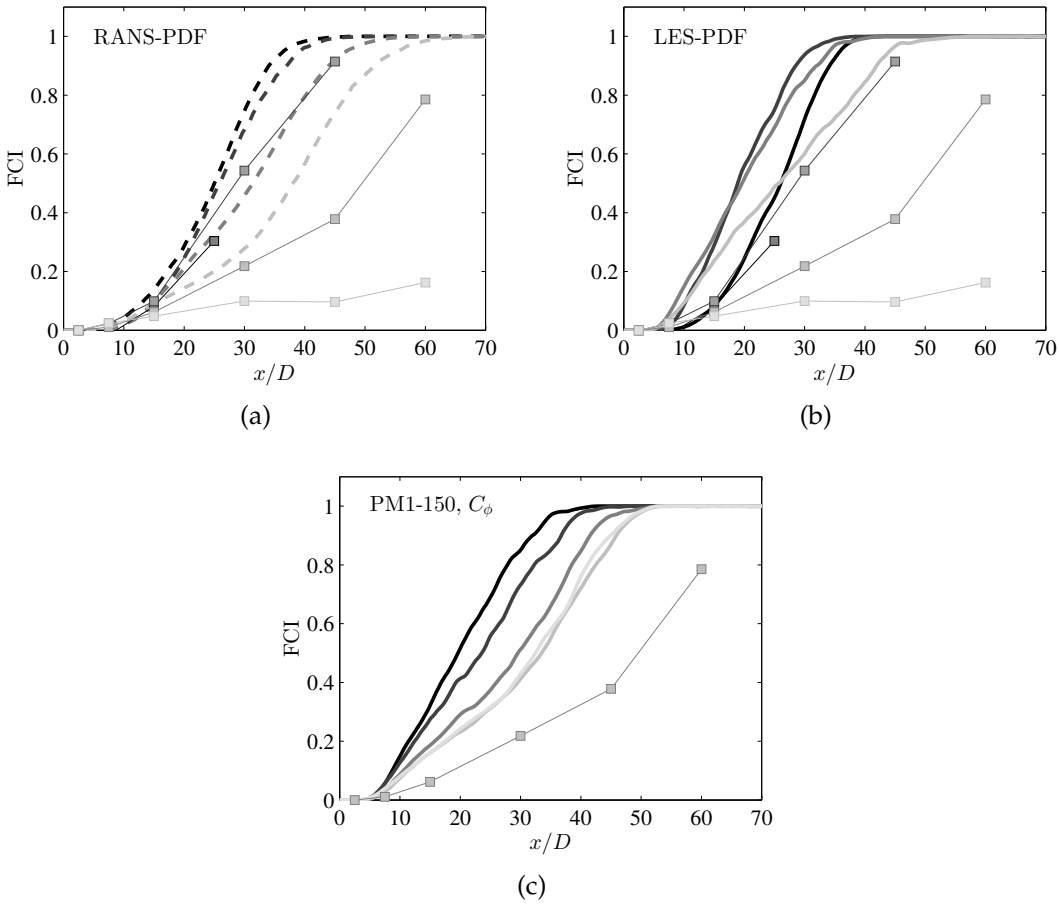

Figure 3.21: Fuel Consumption Index (FCI) on the centerline of the jet ($r/D = 0$) as a function of axial position (x/D) from the experimental measurements of the PPJB flames and various calculations from this study. In all plots, the experimental measurements are denoted by the lines with square markers. The leftmost plot (a) shows the results from the RANS-PDF calculations in the dashed lines. The rightmost plot (b) shows the results from the LES-PDF calculations in the solid lines. In both (a) and (b), the color of the line denotes the flame. The darkest line is for PM1-50, the second darkest is for PM1-100, the second lightest is for PM1-150, and the lightest is for PM1-200. In the rightmost plot (c), the results from the parameter study of C_M in the LES-PDF calculations of PM1-150 are shown. The line colors, from dark to light, denote values of C_M of 5, 10, 20, 50, and 100.

Methodology	Chemistry Model	Molecular Diffusion	CPU Hours
RANS-PDF	3-FGM	–	1,700
	17-ISAT	–	2,300
	17-ISAT	1-RW	2,400
	54-ISAT	–	3,800
LES-PDF	3-FGM	1-MT	18,000
	17-ISAT	1-MT	52,000
	17-ISAT	17-MT	190,000

Table 3.7: Table of computational cost for several different modeling approaches for flame PM1-50. The number of variables used to describe the thermochemistry and the number of unique diffusivities are both indicated before the name of each respective model. The molecular diffusion models are (RW) the random walk in position space (Eq. 3.1), and (MT) full molecular transport with interaction-by-exchange-with-the-mean mixing and mean drift (Eq. 3.5).

configurations of PM1-50. The LES-PDF calculations are generally more expensive by a factor of about 20 compared to the RANS-PDF calculations. So, in this flow, the advantages of LES-PDF are somewhat under-realized; in more practical applications to combustion devices, where the flow is much more complex, the benefits of using LES-PDF would provide greater justification to its higher cost.

3.5 Conclusions

In this study, both RANS-PDF and LES-PDF computational methodologies have been employed to investigate thoroughly the PPJB flames. The most crucial aspects of modeling these flames successfully have been identified in this work in the following five conclusions:

1. Molecular diffusion is important in the pilot-coflow region of the near-field. This process is implemented into the RANS-PDF method using a crude random-walk model and is tested for accuracy. The resulting mean fields of mixture fractions, temperature, and species are much improved through these calculations. The spurious production of variance from the random walk model, however, results in poor predictions of the RMS fields near the pilot-coflow mixing layer. A newly developed implementation of molecular diffusion [57, 58] is used in the LES-PDF calculations, which yields much improved RMS statistics without a spurious production of variance.

2. A simple FGM three-variable chemistry model based on two conserved scalars (mixture fractions) and one reaction progress variable is implemented and tested for accuracy. The results indicate predictions of fuel consumption in good agreement with calculations using detailed chemistry for all four PPJB flames. The mass fractions of major species in these flames appear relatively insensitive to the chemistry modeling, as noted in previous studies. Comparisons to identical calculations using full chemistry give a good quantitative comparison between the two approaches. Although good agreement between the calculations with detailed chemistry and FGM-based chemistry is obtained for all four PPJB flames, the reaction progress is overpredicted in PM1-150 and PM1-200. Therefore, strong conclusions about the accuracy of the FGM-based approach hold only for PM1-50 and PM1-100.

3. Boundary conditions considering the heat loss in the coflow, the curved geometry of the pilot-coflow interface, and compositions taken from fully burnt laminar flames in the pilot and coflow streams, yield calculations

in very good agreement with the measurements near the burner exit. The heat loss has a small effect on the amount of fuel consumed downstream. The curved geometry of the pilot-coflow interface shifts the pilot and coflow mixture fractions toward the centerline. The laminar flame boundary conditions yield slightly better predictions of CO and OH in the pilot than compared to equilibrium conditions, but do not significantly affect the mass fractions of major species throughout the flame.

4. For the low velocity flames (PM1-50 and PM1-100), good results can be obtained through both RANS-PDF and LES-PDF methods using the above boundary conditions and treatment of molecular diffusion. This is quantified by reasonable agreement in the mean and RMS statistics of temperature and species mass fractions throughout all measured locations.

5. For the high velocity flames (PM1-150 and PM1-200), the RANS-PDF calculations overpredict the reaction progress beyond x/D of 15, as observed in previous studies of these flames [12,46]. The LES-PDF calculations yield excellent agreement in the mean and RMS statistics of temperature and species mass fractions at x/D of 15 and 30 when the value of C_M is increased to around 50 or 100, whereas previous RANS-PDF studies of C_ϕ did not achieve quantitative agreement with larger C_ϕ due to the affect of C_ϕ on the scalar flux, the level of turbulence modeling, and the boundary conditions. The LES-PDF calculations provide a strong link between the larger values of mixing frequency, and the observed improvement in the reaction progress. The results indicate the mixing frequency being dominated by scales different that that in Eq. 3.6 for these conditions.

Most future work in calculations of the PPJB ought to be devoted to determining a more suitable scaling for the mixing frequency in LES-PDF calcula-

tions, and exploring a framework for the RANS-PDF calculations where C_ϕ does not significantly alter the scalar flux. Future studies ought to focus comparison on the regions of the flow which have been most challenging to model; the fuel consumption index shown in Figure 3.21 is introduced to provide an efficient way to compare the quality of calculations. This figure, which succinctly summarizes the calculations of the entire flame series, highlights the remaining challenges that lie ahead in understanding these flames.

Since the mixing models are the greatest source of modeling uncertainty in these and previous calculations, further experimental study focused on characterizing the mixing processes in these flames would be insightful. The most direct way to characterize the mixing is to measure the conditional diffusion of chemical species, which then need to be compared to the conditional diffusion obtained from each mixing model. Additionally, measurements of the scalar dissipation rate of chemical species would be useful in a comparison to the scalar dissipation rate implied by each mixing model.

Future calculations ought to seek improvement where the current calculations and previous calculations have shortcomings, that is, in predicting the fuel consumption in PM1-150 and PM1-200 at x/D of 30 and beyond. It is emphasized here that the mixing models play a critical role in determining the reaction progress in these regions. A thorough understanding of the sensitivity of each calculation to all aspects of the mixing models ought to be demonstrated in future studies and compared to the sensitivities observed here. While this work and the previously mentioned studies have all advanced the understanding of these flames and the performance of the models in these conditions, there still remains work to be done in formulating a robust computational framework

which performs well in this interesting, challenging, and practical combustion regime.

3.6 Acknowledgements

This work was supported in part by NSF Award No. CBET-1033246. This research was made with Government support under and awarded by DoD, Air Force Office of Scientific Research, National Defense Science and Engineering Graduate (NDSEG) Fellowship, 32 CFR 168a.

CHAPTER 4

AN INVESTIGATION OF MIXING IN A THREE-STREAM TURBULENT JET

4.1 Introduction

The probability density function (PDF) method [2, 74] is a useful tool for modeling turbulent reacting flows because the chemical source term is closed, and therefore, can be treated without any additional modeling. Because of this ability to account for the highly non-linear chemical source term, the PDF method has yielded successful calculations of turbulent flames, including those which exhibit turbulence-chemistry interactions such as extinction and re-ignition [5–9]. However, the PDF method depends on mixing models to account for the effects of molecular diffusion. Chemical reaction and molecular diffusion are inherently highly-coupled physical processes, so the mixing models incur one of the largest sources of modeling uncertainty in PDF calculations. Therefore, in order to develop sound computational methodologies based on the PDF method, it is essential to have a good understanding of (i) the fundamental mixing process, (ii) the ability of mixing models to represent this process, and (iii) the sensitivity of calculations to the mixing models.

In PDF methods, a transport equation for the PDF of composition or the joint PDF of velocity, turbulence frequency, and composition is solved. For example, in the composition PDF method for constant-property flow, the PDF transport equation is

$$\frac{\partial f_\phi}{\partial t} + \frac{\partial}{\partial x_j}\left(f_\phi\left(U_j + \langle u_j|\psi\rangle\right)\right) = -\frac{\partial}{\partial \psi}\left(f_\phi\left(\langle \Gamma\nabla^2\phi|\psi\rangle + S(\psi)\right)\right) \tag{4.1}$$

where f_ϕ is the PDF of the composition, ϕ, U_j and u_j are the mean and fluctuating velocities, S is the reaction source term, Γ is the molecular diffusivity, and ψ is the sample-space variable corresponding to ϕ.

The first term on the right-hand side, $\langle \Gamma \nabla^2 \phi | \psi \rangle$, is the conditional diffusion of ϕ which represents the effects of molecular diffusion. The transport equation for the joint PDF of velocity, turbulence frequency, and composition is similar in form to Eq. 4.1, with the conditional diffusion term still being one of the unclosed terms. In both PDF methodologies, the reaction source term S is in closed form, while a mixing model is needed to account for the conditional diffusion.

4.1.1 Mixing models

Several mixing models have been developed to model the unclosed conditional diffusion term. Three of the most-widely used mixing models are: (i) the Interaction by Exchange with the Mean (IEM) [29, 30] model, (ii) the Modified Curl (MC) [27, 28] model, and (iii) the Euclidean Minimum Spanning Tree (EMST) [19] model. In the IEM model, particle compositions relax linearly toward the cell mean; in the MC model, particles within a cell are paired randomly and instantaneously mix; in the EMST model, an EMST is formed in composition space; particles mix with neighboring particles in the EMST so that the mixing remains local in composition space. The constant mechanical-to-scalar time scale ratio C_ϕ determines the mixing rate in all of these mixing models. The significance of C_ϕ here is that in the simple case of a statistically homogeneous conserved passive scalar, all mixing models yield the same rate of decay of the scalar variance. The development of novel mixing models is an area of active re-

search, and several promising new models are being developed as well [75–77].

The effects of mixing models have been studied in PDF calculations of a wide variety of reacting flows, including non-premixed lifted flames [8, 78], piloted non-premixed flames [9], bluff-body non-premixed flames [79], opposed-flow premixed flames [80], piloted premixed jet flames [14, 46], and even high-pressure, premixed, homogeneous charge compression ignition engines [81]. Given the highly coupled nature of molecular diffusion and chemical reaction, these studies generally show significant sensitivity of the calculated flows to the choice of mixing model and value of C_ϕ. Typically, in parametric studies of mixing models such as these, calculations are performed using a variety of mixing models and values of C_ϕ, and the mean and RMS scalar fields are compared to experimental data.

4.1.2 Multiple scalar mixing

While studying the mixing processes and the effects of mixing models in the context of reacting flows is both interesting and practical, studying more fundamental mixing problems in non-reacting flows is also necessary. Much experimental research has been performed on the mixing of a single passive scalar [82–88] including characterization of the mean and RMS statistics, as well as the PDF of the scalar. Direct numerical simulation (DNS) has also been employed to study single passive scalar mixing [89–93] and in these studies, more complete information about the flow is extracted, in some cases including the conditional diffusion term.

In reacting flows, the mixing processes involve multiple scalars. The flows

in most practical combustion devices require a combination of a fuel stream, an oxidizer stream, a pilot stream, and at least one coflowing stream. So, the fundamental studies of single-scalar mixing have been expanded upon. The mixing of two scalars has been studied experimentally [94,95] and computationally using DNS [96–98] and PDF methods [99]. In [99], the DNS of the temporally-evolving mixing layer [98] is studied using the joint velocity-composition PDF for several different mixing models. It is found here that the IEM mixing model conditioned on velocity (IECM) [52, 101, 102] and a mixing model based on parameterized scalar profiles (PSP) [75,77] both outperform the standard IEM mixing model. The joint PDFs of the two scalars and the conditional diffusion from these two models show substantially better agreement with the DNS data.

Recent advances in experimental techniques, such as high-resolution planar laser-induced fluorescence (PLIF) imaging, have enabled experiments in which statistics more insightful than mean and RMS measurements can be extracted. The experiment in [95] considers the mixing of two scalars in a turbulent coaxial jet; this experiment utilizes PLIF and Rayleigh scattering to obtain high-resolution images of instantaneous mixture fractions, enabling the conditional diffusion and conditional scalar dissipation rate to be computed experimentally.

In multiple scalar mixing problems, the arrangement of the scalars plays an important role in determining the mixing process. The turbulent coaxial jet in [95] is useful because the configuration mimics that in combustion devices and many rudimentary turbulent jet flames: Two streams (the jet and the coflow) are initially separated by a third stream (the annulus), so that the mixing between two of the three streams (the jet and the coflow) can only occur through interaction with the other stream (the annulus). The turbulent coaxial

jet of [95] is the basis for this study, and the detailed experimental configuration and procedure are described are Sec. 4.2.

4.1.3 Objectives

The goals of this work are (i) to perform PDF calculations of the coaxial jet studied experimentally in [95], (ii) to evaluate the efficacy of three standard mixing models (IEM, MC, and EMST) by calculating the conditional diffusion in the PDF calculations and comparing it to the experimentally observed conditional diffusion, (iii) to assess the two-dimensional measurements of conditional diffusion and scalar dissipation rate through LES of varying resolution, and lastly, (iv) to examine the behavior of the mixing models used in LES-PDF calculations by evaluating the sensitivity to model parameters and examining a new model for the turbulent diffusivity redistribution.

While Reynolds-Averaged Navier-Stokes (RANS)-based PDF methods have been studied carefully in the past, there remain many open questions about the performance of mixing models in LES-PDF calculations. Objective (iv) listed above is directed to address some of these issues by carefully examining calculations of this flow and comparing the results to the experimental data. The approach used in this study has advantages over the other parametric studies of mixing models in reacting flows [8, 9, 14, 46, 78–81] because the conditional diffusion term can be explicitly compared to the experimental data; additionally, the flow can be studied apart from the complexities associated with chemical reaction. And although the configuration is similar to PDF comparison to the DNS data in [99], here the configuration is a coaxial jet (as opposed to a mix-

ing layer); furthermore, here the results can be compared to experimental data, which is important in ensuring that all the real physical processes are accounted for correctly in the model.

The remainder of this chapter is outlined as follows: In Sec. 4.2, the configuration of the flow and the experimental procedures used in [95] are described. Next, in Sec. 4.3, the RANS-PDF framework is presented, the calculations are described, and the results are shown for different mixing models. In Sec. 4.4 and 4.5, the LES and LES-PDF calculations are presented. Lastly, a comparison between all three calculation methodologies is discussed in Sec. 4.6, and conclusions are drawn in Sec. 4.7.

4.2 Flow configuration

The flow studied in this work is based on the experiment conducted in [95], and consists of three concentric streams: a jet, an annulus, and a coflow. The central jet consists of acetone-doped air (7% acetone by volume) at a high velocity (34.5 m/s); surrounding the central jet is an annular flow of pure ethylene, also at a high velocity (32.5 m/s); surrounding the annulus is a coflow of air at a low velocity (0.4 m/s). The outer diameter of the coflow is sufficiently large so that the jet and annulus streams do not interact with the ambient air. Detailed properties of the configuration are shown in Table 4.1. The diameter of the jet, D, is 5.54 mm and is used as a reference length scale throughout this study. The maximum density ratio is 1.11, and the Reynolds number (based on the jet composition, diameter, and bulk velocity) is 14,300.

In the experiment, simultaneous measurements of the acetone and ethylene

Stream Name	Jet	Annulus	Coflow
Inner Diameter (mm)	–	6.35	9.50
Outer Diameter (mm)	5.54	8.38	150
Bulk Velocity (m/s)	34.5	32.5	0.4
Density (kg/m^3)	1.26	1.14	1.17
Viscosity (m^2/s$\times 10^{-6}$)	13.4	8.3	15.9
$Y_{C_3H_6O}$	0.132	0	0
$Y_{C_2H_4}$	0	1	0
Y_{N_2}	0.666	0	0.767
Y_{O_2}	0.202	0	0.233

Table 4.1: Properties of inflowing streams in the three-stream mixing jet. The density and kinematic viscosity are computed using Chemkin based on the mass fractions, Y, indicated here.

mass fractions are made using two-dimensional planar imaging. The mass fraction of the acetone is obtained using PLIF, while the mass fraction of ethylene is obtained from Rayleigh scattering. The measurements are made with a spatial resolution of 55 μm. Time-averaged means and RMS statistics of the acetone and ethylene mass fractions are computed from the high-resolution images.

We denote by ξ_1, ξ_2, and ξ_3 the mixture fraction based on the jet, the annulus, and the coflow, respectively. Only two of these are independent (since $\xi_1 + \xi_2 + \xi_3 = 1$), and henceforth we consider ξ_1 and ξ_2. The jet mixture fraction, ξ_1, represents the fraction of mass originating from the central jet. It is approximated here as $\xi_1 = Y_{C_3H_6O}/Y^1_{C_3H_6O}$, where $Y_{C_3H_6O}$ is the mass fraction of acetone, and $Y^1_{C_3H_6O}$ is the mass fraction of acetone in the jet. It is only approximated to be the actual mixture fraction because of differential diffusion. The annulus mixture fraction, ξ_2, represents the fraction of mass originating from the annulus. Because the annulus contains only pure ethylene, ξ_2 is defined simply as $\xi_2 = Y_{C_2H_4}$, where $Y_{C_2H_4}$ is the mass fraction of ethylene.

The scalar dissipation rate, $\chi = 2\Gamma\,(\partial\xi/\partial x_i)\,(\partial\xi/\partial x_i)$, and the scalar diffu-

sion term, $D = \Gamma\nabla^2\xi$, are both computed for ξ_1 and ξ_2 in the two components of the sampled images using a tenth-order central difference scheme. The term Γ is the molecular diffusivity of the scalar. In the evaluation of χ and D in the experiment, a constant value is used for the diffusivity of each scalar: $\Gamma_1 = 10.39\times10^{-6}\text{m}^2/\text{s}$ and $\Gamma_2 = 14.69\times10^{-6}\text{m}^2/\text{s}$. The conditional scalar dissipation rate, $\langle\chi|\xi = \hat{\xi}\rangle$, where the angle brackets denote an ensemble average and $\hat{\xi}$ is a sample-space variable, and the conditional diffusion, $\langle D|\xi = \hat{\xi}\rangle$, are recorded from between 3,000 and 5,400 sampled images.

An uncertainty analysis performed in [95] shows the RMS fluctuations in the combined noise and uncertainty are around 2% for the mean and RMS scalar statistics. The scalar dissipation rate is corrected for measurement noise, and by examining finite-difference schemes of varying order, it is estimated that the scalar dissipation rate is at least 98% resolved in the experimental measurements.

4.3 RANS-PDF calculations

4.3.1 RANS-based joint PDF methodology

This flow is first investigated computationally using the joint velocity-turbulence frequency-composition PDF method with RANS-level turbulence closure [2, 16]. Throughout this paper, this method is referred to simply as the RANS-PDF method. In the implementation of this method [23], a finite-volume solver evaluates the mean equations of mass, momentum, energy, and state while a Lagrangian Monte Carlo particle solver advances particles in veloc-

ity, turbulence frequency, and composition to solve for the joint PDF of velocity, turbulence frequency, and composition.

In the particle solver, the particle velocity evolves via the simplified Langevin model (SLM) [17], while the particle turbulence frequency evolves by a stochastic frequency model [18]. The stochastic frequency model relies on a number of parameters, and the standard values are used for each parameter as in many previous studies [8, 9, 46, 79]; for the constant $C_{\omega 1}$, which essentially controls the spreading rate of the jet, a value of $C_{\omega 1} = 0.65$ is used based on a parametric study made to achieve the correct jet spreading rate. This value is well within the range of values (from $C_{\omega 1} = 0.56$ [79] to $C_{\omega 1} = 0.70$ [46]) used in similar studies, and is identical to the value used in [8, 9].

The composition will generally evolve due to both molecular diffusion and chemical reaction. The main advantage of the PDF method is that the chemical reaction can be treated without modeling; in this case, the flow is inert, so there is no chemical reaction term. The density of a particle, ρ^* is computed through the relation

$$\rho^* = 1/\left(\xi_1^* \left(1/\rho_1\right) + \xi_2^* \left(1/\rho_2\right) + \xi_3^* \left(1/\rho_3\right)\right) \tag{4.2}$$

where ξ_1^*, ξ_2^*, and ξ_3^* are mixture fractions for the particle, and ρ_1, ρ_2, and ρ_3 are the densities of the three streams from Table 4.1. Eq. 4.2 essentially states that the specific volume of the mixture is equal to the mass-fraction-weighted specific volume of each component of that mixture, as the fluid is considered to be an ideal gas. The effect of molecular diffusion on the particle composition is treated by a mixing model. Here, the IEM, MC, and EMST mixing models are examined, with the IEM being used for the base case.

In the implementation of this method, finite-volume and particle solvers are

coupled. The finite-volume solver provides the mean velocity, density, and pressure to the particle solver, while the particle solver provides the turbulent fluxes and the reaction source term (which in this case is zero, since the flow is non-reacting). When a statistically stationary state is reached in the calculations, the statistics are time-averaged until sufficient temporal convergence of the statistics is reached.

4.3.2 Computational configuration

To model this flow, a rectangular computational domain extending $54D$ in the axial (x) direction and $13.5D$ in the radial (r) direction is used. Figure 4.1 shows a sketch of the computational domain. This size is chosen based on a parametric study of domain sizes, where the statistics of interest (mean and RMS mixture fractions at x/D of 30, near the farthest-downstream measurement in the experiment) are not significantly affected by the outlet boundary condition and the lateral boundary condition.

The lateral boundary condition ($r/D = 13.5$) is treated as a perfect-slip wall, and symmetry conditions are applied at the axis ($r/D = 0$). For the outlet boundary condition ($x/D = 54$), the mean pressure is specified to be uniform, and the density and velocities are extrapolated from the interior. At the inflow boundary ($x/D = 0$), the mean velocities, Reynolds stresses, and turbulence frequency are specified from a separate calculation using a 5-equation Reynolds-stress equation turbulence model. These calculations extend upstream beyond the inflow plane, and the flow of the pipe and the annulus are fully developed flows. Figure 4.2 shows the mean axial velocity and three of the Reynolds-stresses at the

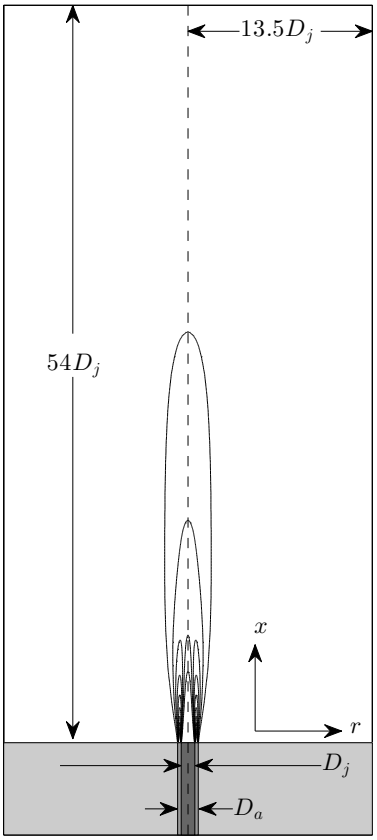

Figure 4.1: Computational domain for RANS-PDF calculations.

inflow plane. The composition at the inflow boundary is specified as in Table 4.1.

At 64 locations throughout the flow domain, the joint PDF of ξ_1 and ξ_2 and the conditional diffusion of ξ_1 and ξ_2 are calculated. The sampled locations include 32 points along the jet centerline ($r/D = 0$), and 16 points each along radial profiles at $x/D = 3.29$ and $x/D = 6.99$. Each location at which measurements are made in [95] is accounted for. At every time step during the statistically stationary period during which statistics are collected, particles within a rectangle extending 275μm (about $0.05D$) in the radial direction and 495μm (about $0.09D$) in the axial direction centered about a sampling location are sampled at that lo-

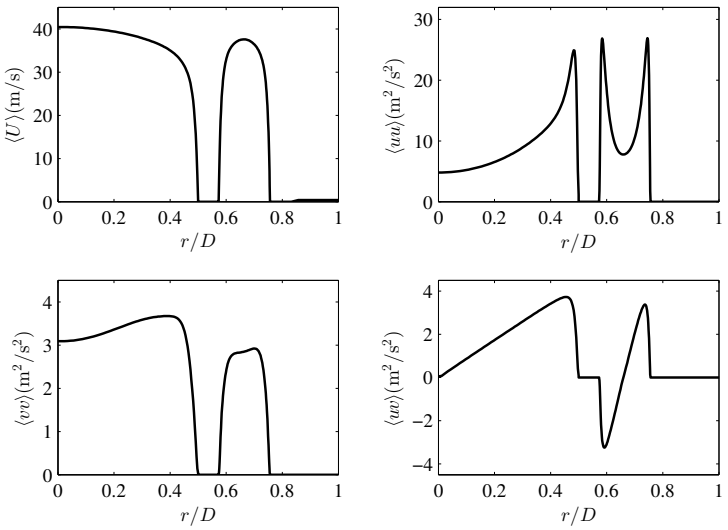

Figure 4.2: Boundary conditions for RANS-PDF calculations: the mean axial velocity, $\langle U \rangle$, (top-left) and the Reynolds stresses $\langle uu \rangle$ (top-right), $\langle vv \rangle$ (bottom-left), and $\langle uv \rangle$ (bottom-right).

cation. The spatial extent of this sampling range is equivalent to the resolution used in the experiments for computing the conditional statistics. Each sampled particle is binned into 1 of 400 equally-spaced bins, for each component of the two-dimensional mixture fraction space ranging from 0 to 1. The conditional diffusion for ξ_1 and ξ_2 is calculated as the change in ξ_1 and ξ_2 over the mixing sub-step, divided by the time step.

4.3.3 Numerical accuracy and comparison with experimental data

Grid convergence

The numerical accuracy of the calculations is affected by (i) the grid size, (ii) the number of particles per cell, (iii) the duration over which time-averaging is performed, and (iv) the time step. The first three of these error sources are systematically tested, and a numerical error is computed for statistics of interest. The fourth error source, the time step, is tested indirectly as the grid is refined. In these tests, an error is evaluated for the statistics $\langle\widetilde{\xi_1}\rangle$, $\langle\widetilde{\xi_2}\rangle$, $\langle\widetilde{\xi_1''}\rangle$, and $\langle\widetilde{\xi_2''}\rangle$. In the notation used here, the angle brackets $\langle\rangle$ denote a time-averaged quantity, the tilde $\tilde{}$ denotes a mass-weighted quantity, and the double-prime $''$ denotes the RMS; so $\langle\widetilde{\xi_1}\rangle$ is the time-averaged mass-weighted mean of ξ_1 and $\langle\widetilde{\xi_1''}\rangle$ is the time-averaged mass-weighted RMS of ξ_1. The errors defined for each of these four quantities are denoted by ϵ_{M1}, ϵ_{M2}, ϵ_{R1}, and ϵ_{R2}, respectively. The error for each statistic is defined as the maximum value of the difference between that statistic and the value of that statistic in the most numerically accurate solution for the range $3.29 \leq x/D \leq 6.99$.

Grid Name	n_x	n_r	n_T	ϵ_{M1}	ϵ_{M2}	ϵ_{R1}	ϵ_{R2}
G-1	64	64	4.1	0.125	0.175	0.089	0.043
G-2	96	96	9.2	0.091	0.086	0.065	0.029
G-3	128	128	16.4	0.061	0.043	0.044	0.021
G-4	192	192	36.9	0.024	0.016	0.020	0.009
G-5	256	256	65.5	0.016	0.010	0.013	0.008
G-6	384	384	147.5	–	–	–	–

Table 4.2: Grid sizes (number of cells in x and r, n_x and n_r, and total number of cells in thousands, n_T) and errors from convergence tests of the RANS-PDF calculations.

Tests are performed with 25, 50, 100, and 200 particles per cell, with grids ranging from 64×64 to 384×384, and for durations of time-averaging between 1,000 and 20,000 iterations. In the tests, the IEM mixing model is used with a value of C_ϕ of 1.5. These tests show that the largest source of error is in the grid resolution. The grid sizes and corresponding numerical errors are shown in Table 4.2. As the grid is refined, the errors for all statistics are successively reduced. For grid G-4, the numerical error in all statistics is around 2%, which is close to the experimental error. Based on these convergence tests, the parameters chosen for the base case calculations are 100 particles per cell, a grid size of 192×192, and a minimum of 10,000 iterations of time-averaging.

Comparison with experimental data

Figure 4.3 shows statistics of mean and RMS quantities on the jet centerline ($r/D = 0$) for four of the grids in Table 4.2 and the experimental data [95]. On the finest grids, $\langle\widetilde{\xi_1}\rangle$ and $\langle\widetilde{\xi_2}\rangle$ exhibit good agreement with the experimental data. The largest discrepancy between the experimental data and the numerically accurate calculations is about 6% at $x/D = 6.99$, where the initial spreading of the jet is slightly more rapid in the calculations than in the experiments. For the RMS statistics, the agreement on the centerline is also reasonable; here too, the largest disagreement occurs in the near-field of the jet, where the RMS is slightly overpredicted in the calculations.

Figure 4.3 also shows the fluctuation intensities, $\langle\widetilde{\xi_1''}\rangle$ / $\langle\widetilde{\xi_1}\rangle$ and $\langle\widetilde{\xi_2''}\rangle$ / $\langle\widetilde{\xi_2}\rangle$. In the PDF calculations, the peak fluctuation intensity of ξ_1 is captured well. However, the measurements indicate the fluctuation approaching an asymptotic value near 0.21 downstream, in accord with the self-similar region in bi-

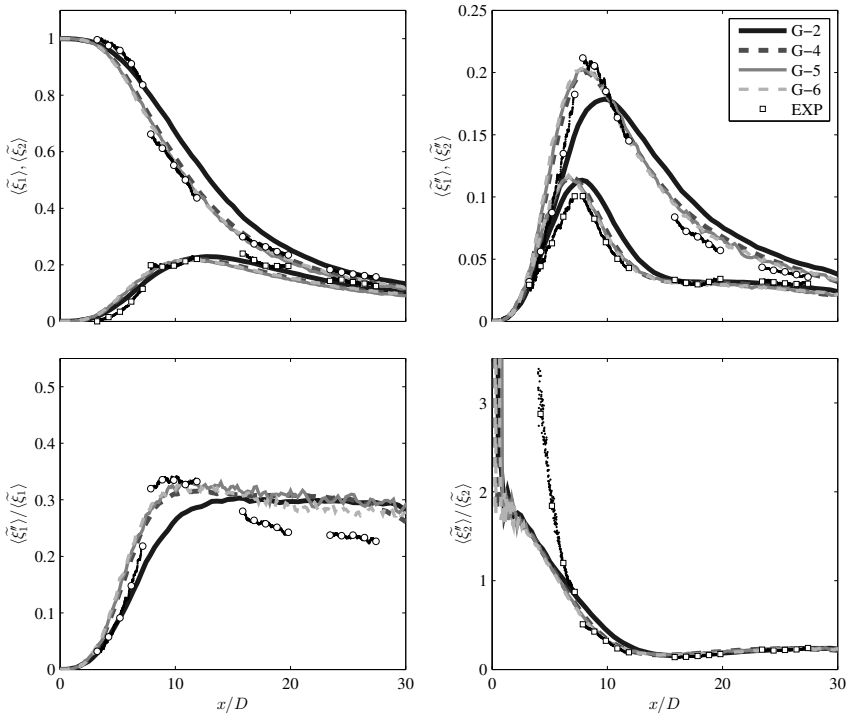

Figure 4.3: Centerline profile of time-averaged mass-weighted mean mixture fractions (top left), RMS mixture fractions (top right), and fluctuation intensities (bottom) in the RANS-PDF grid convergence study. Solid dark line: G-2; Dashed dark line: G-4; Solid gray line: G-5; Dashed light gray line: G-6; Circles: experimental data for ξ_1 [95]; Squares: experimental data for ξ_2 [95].

nary jet mixing [86,94]. Here, the PDF calculations over-estimate the fluctuation intensity, due to the values of both C_ϕ and $C_{\omega 1}$ used in the calculations. A slightly larger value of C_ϕ leads to decreased variance and hence decreased fluctuation intensity, while a slightly larger value of $C_{\omega 1}$ leads to a decreased spreading rate of the jet, an increased mean ξ_1 downstream, and consequentially a decreased fluctuation intensity. The fluctuation intensity of ξ_2, on the other hand, demonstrates good consistency with the experimentally observed values downstream, and does approach the value observed in the self-similar region of binary jet mixing, around 0.21. In the near-field, however, there is considerable variation

among the calculations and the experimental data, due to the small values of $\langle\widetilde{\xi_2}\rangle$ and the sensitivity to the inflow boundary conditions. There is also more numerical error observed in the calculations of the fluctuation intensities here, mostly arising from the combination of insufficient time-averaging and low values of the mean farther downstream.

Figure 4.4 shows the radial profiles of $\langle\widetilde{\xi_1}\rangle$, $\langle\widetilde{\xi_2}\rangle$, $\langle\widetilde{\xi_1''}\rangle$, and $\langle\widetilde{\xi_2''}\rangle$ for the same PDF calculations and the experimental data. As noted from Figure 4.3, $\langle\widetilde{\xi_1}\rangle$ decays slightly faster in the PDF calculations than as measured experimentally. However, Figure 4.4 shows that this is limited to a small region near the jet centerline. The agreement in $\langle\widetilde{\xi_2}\rangle$ is also reasonable, although the peak value, which occurs around $r/D = 0.6$ is slightly under-predicted in the calculations due to the annulus spreading slightly faster in the calculations.

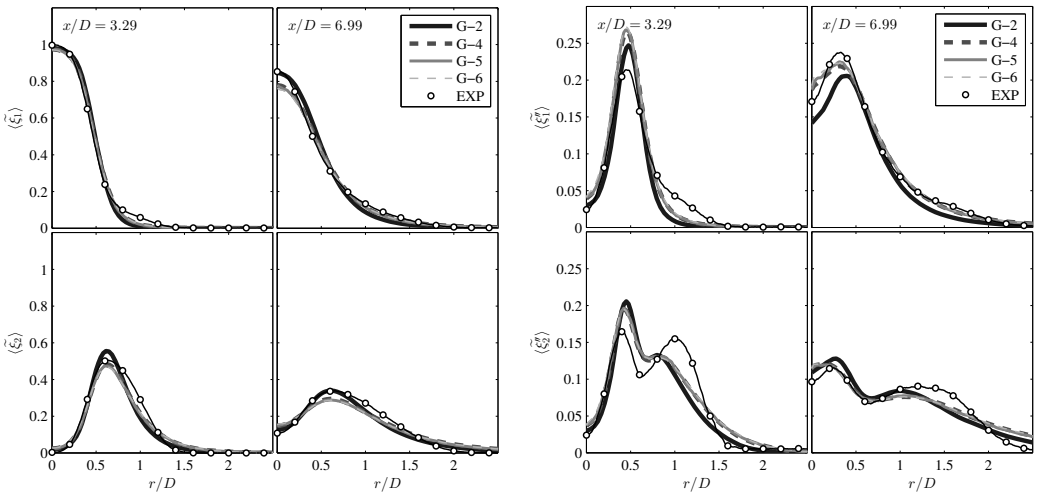

(a) (b)

Figure 4.4: Radial profiles of time-averaged mass-weighted mean (a) and RMS (b) mixture fractions in the RANS-PDF grid convergence study. Solid dark line: G-2; Dashed dark line: G-4; Solid gray line: G-5; Dashed light gray line: G-6; Circles: experimental data [95].

The RMS statistics, shown in Figure 4.4 (b), indicate the peak RMS of both ξ_1

and ξ_2 being overpredicted at $x/D = 3.29$, but farther downstream at $x/D = 6.99$ the agreement in the peak RMS is good for both ξ_1 and ξ_2. The overprediction at $x/D = 3.29$ is a result of both the inlet boundary conditions, which are sensitive to the value of ω, the turbulence frequency, and the mixing model. The values of $\langle\widetilde{\xi_1''}\rangle$ from the calculations are in very good agreement with that from the experiments at $x/D = 6.99$. The values of $\langle\widetilde{\xi_2''}\rangle$ from the calculations are in reasonable agreement with the experimental data at $x/D = 6.99$ in the region of jet-annulus mixing ($0 \leq r/D \leq 1$), but not in the region of annulus-coflow mixing ($r/D \leq 1$). In the region of annulus-coflow mixing for all these axial locations, the profile of $\langle\widetilde{\xi_2''}\rangle$ is much sharper in the experimental data; in the regions where $\langle\widetilde{\xi_2''}\rangle$ is large, the calculations yield a smaller value; in the regions where $\langle\widetilde{\xi_2''}\rangle$ is small, the calculations yield a larger value. This behavior is primarily due to the mixing models; in this region of the flow, molecular diffusion is important due to the very low velocity of the coflow; additionally, the mixing process is velocity dependent, so these mixing models, which do not consider the velocity, are likely to encounter difficulties where there is a large velocity gradient, as there is here.

4.3.4 Comparison of mixing models in the RANS-PDF calculations

Shown in Figure 4.5 are the results of calculations using the IEM mixing model and different values of C_ϕ, namely, C_ϕ of 0.5, 1.5, and 4.5. There is a small sensitivity of $\langle\widetilde{\xi_1}\rangle$ to the value of C_ϕ; larger values of C_ϕ result in a decreased jet spreading rate due to the decreased scalar flux. There is a much larger sensi-

tivity to the RMS statistics, $\langle\widetilde{\xi_1''}\rangle$ and $\langle\widetilde{\xi_2''}\rangle$; larger values of C_ϕ yield a decreased RMS, which is expected since C_ϕ directly impacts the scalar variance. Figure 4.5 convincingly shows that in these calculations, a value of $C_\phi = 1.5$ yields both mean and RMS fields in the best agreement with the measurements. This value is in close agreement with the experimentally measured values, around 1.5 in inert round jets [88] and in the range 1.5–2.5 in shear flows [83].

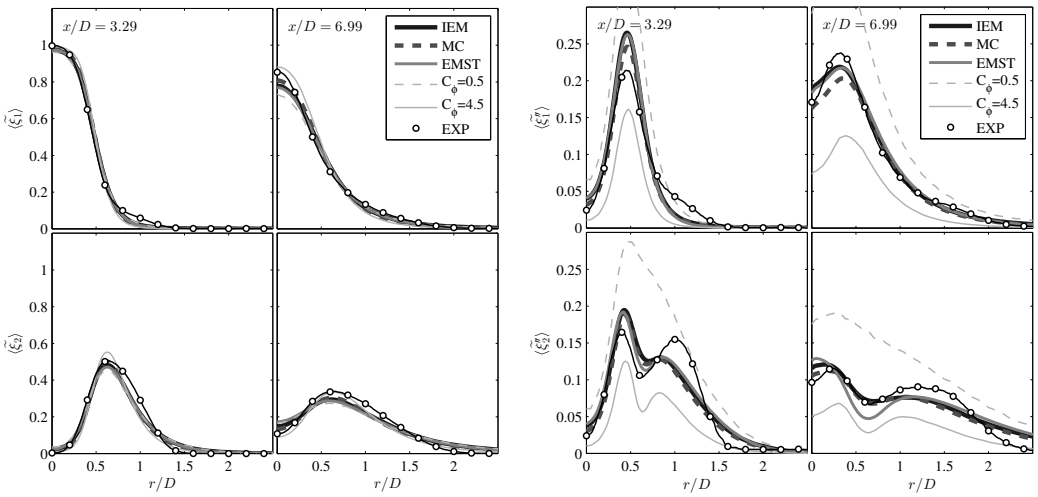

(a) (b)

Figure 4.5: Radial profiles of time-averaged mass-weighted mean (a) and RMS (b) mixture fractions in the RANS-PDF mixing model study. Solid dark line: IEM, $C_\phi = 1.5$; Dashed dark line: MC, $C_\phi = 1.5$; Solid gray line: EMST, $C_\phi = 1.5$; Dashed light gray line: IEM, $C_\phi = 0.5$; Light gray solid line: IEM, $C_\phi = 4.5$; Circles: experimental data [95].

The other two mixing models (MC and EMST) are also used to make calculations of this flow, and the resulting centerline and radial profiles of the mean and RMS statistics are very similar to those using the IEM model. Figure 4.5 demonstrates the similarity of the radial profiles of the statistics $\langle\widetilde{\xi_1}\rangle$, $\langle\widetilde{\xi_2}\rangle$, $\langle\widetilde{\xi_1''}\rangle$, and $\langle\widetilde{\xi_2''}\rangle$ in the calculations with these three mixing models, all using a value of $C_\phi = 1.5$. The value of C_ϕ has a very similar effect among all three of these mixing models.

The correlation coefficient between the two mixture fractions, ρ_{12}, is defined as

$$\rho_{12} = \frac{\langle \xi_1 \xi_2 \rangle - \langle \xi_1 \rangle \langle \xi_2 \rangle}{\sqrt{\langle \xi_1^2 \rangle - \langle \xi_1 \rangle^2} \sqrt{\langle \xi_2^2 \rangle - \langle \xi_2 \rangle^2}} \tag{4.3}$$

and is shown in Figure 4.6 for these calculations and the experimental measurements. Around the centerline, ρ_{12} is approximately -1, since the mixture fraction of the coflow is very small. With a negligible coflow mixture fraction, the sum $\xi_1 + \xi_2$ is approximately unity, so ξ_1 and ξ_2 are nearly perfectly anti-correlated. All mixing models yield similar values of ρ_{12} near the centerline, and the agreement with the experimental data is good, considering the measurement noise evident on the centerline. Going away from the centerline, the differences between the calculations are more pronounced. With EMST, the correlation coefficient increases at a faster rate (compared to the measurements and calculations with other mixing models) with increasing r/D beginning at about $r/D = 0.75$. The values of ρ_{12} with IEM and MC are very similar to one another, and at large values of r/D, both are much lower than that from EMST and the experimental measurements. At large values of r/D, both the mean and RMS of ξ_1 and ξ_2 are very low, so there is greater numerical uncertainty in these statistics. Figure 4.6 shows that as C_ϕ is increased, the radial profiles of the correlation coefficient become sharper. This observation is consistent with the fact that increasing C_ϕ decreases the scalar variance, and consequently reduces the spreading of the mixing layers. Figure 4.6 also shows the resolved ρ_{12} from LES calculations on the fine Grid-F. These calculations yield a correlation coefficient in very good agreement with the experimental data and are discussed more in detail in Sec. 4.4.

Despite the similarity in the mean and RMS statistics, there is considerable difference in the higher-order statistics for different mixing models. The joint

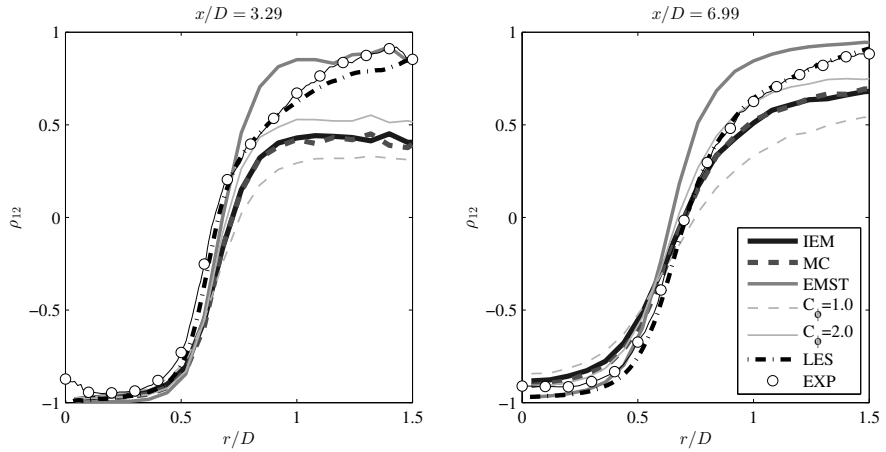

Figure 4.6: Radial profiles of the correlation coefficient. Solid dark line: IEM, $C_\phi = 1.5$; Dashed dark line: MC, $C_\phi = 1.5$; Solid gray line: EMST, $C_\phi = 1.5$; Dashed light gray line: IEM, $C_\phi = 1.0$; Light gray solid line: IEM, $C_\phi = 2.0$; Dashed-dotted line: LES on Grid-F; Circles: experimental data [95].

PDFs and conditional diffusion of ξ_1 and ξ_2 yielded by each mixing model are markedly different. Figures 4.7 and 4.8 show the joint PDF and conditional diffusion from the experiments and calculations, with each figure from a different location: Figure 4.7 is from $(x/D = 3.29, r/D = 0.536)$, and Figure 4.8 is from $(x/D = 6.99, r/D = 0.635)$. These particular locations are chosen such that there is significant mixing of all three streams at those locations.

Compared to the experimental data, the IEM model yields a joint PDF which is more compact in composition space. At $x/D = 6.99$, the joint PDF from the calculations using IEM indicates a bimodal PDF, instead of the unimodal PDF as observed experimentally. This indicates the IEM producing a flapping behavior between the jet and coflow at this location; so even though the mean and RMS statistics are calculated reasonably accurately with the IEM model, the higher-order statistics are not. The shapes of the PDFs from the calculations with IEM are similar in form to what is observed in the joint PDF calculations using the

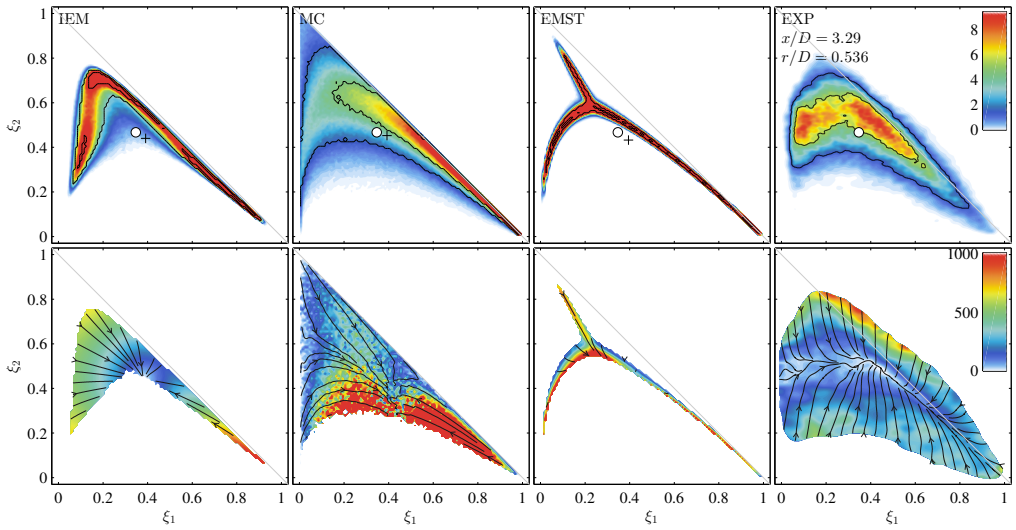

Figure 4.7: Contour plots of the joint PDF of mixture fractions (top) and the magnitude of conditional diffusion (bottom) at $(x/D, r/D) = (3.29, 0.536)$ from the experimental data [95] (right) and RANS-PDF calculations using different mixing models, from left to right: IEM, MC, and EMST. The circle is the experimental mean, and the plus sign is the mean from the PDF calculation. In the top plots, the two solid lines are isocontours which enclose regions with probability 0.5 and 0.9. In the lower plots, the lines with arrows are streamlines, everywhere parallel to the conditional diffusion vector. Color online only.

IEM mixing model in the three-stream mixing layer studied in [99]; in both calculations, the IEM model yields less spreading of the joint PDF in composition space. The conditional diffusion from the IEM model indicates values linearly proportional to the distance from the mean. This is consistent with the model formulation and helps to validate the calculation of the conditional diffusion in the PDF calculations. Although the conditional diffusion is quite different in form to the measured conditional diffusion (as it is expected for the IEM model), the magnitude of the conditional diffusion is of the same order of magnitude in both the calculations and the experiments.

The MC model yields a joint PDF which is qualitatively the most similar to

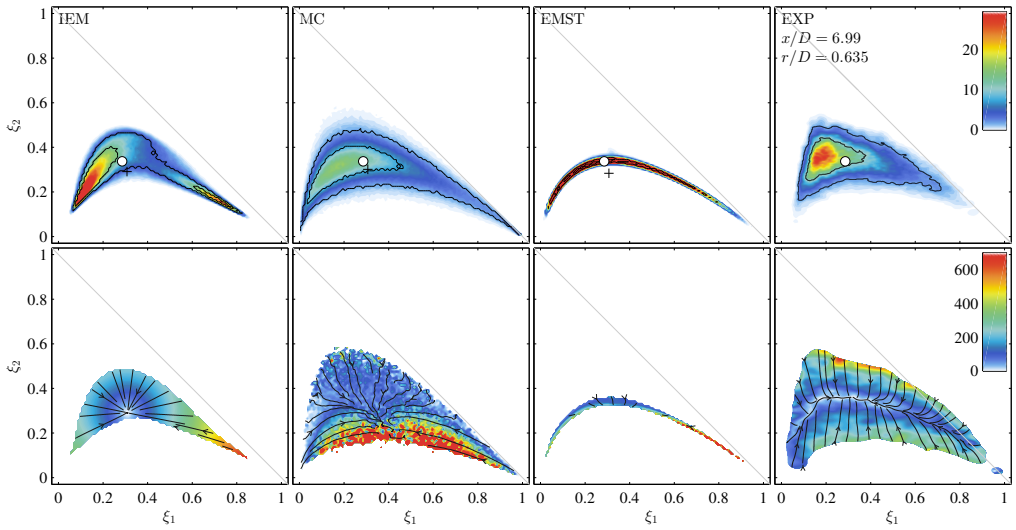

Figure 4.8: Contour plots of the joint PDF of mixture fractions (top) and the magnitude of conditional diffusion (bottom) at $(x/D, r/D) = (6.99, 0.635)$ from the experimental data [95] (right) and RANS-PDF calculations using different mixing models, from left to right: IEM, MC, and EMST. The circle is the experimental mean, and the plus sign is the mean from the PDF calculation. In the top plots, the two solid lines are isocontours which enclose regions with probability 0.5 and 0.9. In the lower plots, the lines with arrows are streamlines, everywhere parallel to the conditional diffusion vector. Color online only.

the joint PDF observed experimentally at $x/D = 6.99$ (Figure 4.8). The main difference between the calculations with the MC model and the experimental data is that MC model yields a joint PDF that is distributed more broadly over the composition space. As with the IEM model, the conditional diffusion yielded by the MC model is quite different from the experimentally observed conditional diffusion, particularly in the locations in which the fast manifolds are observed experimentally.

The EMST mixing model yields the most interesting joint PDFs of all the mixing models studied here. With EMST, the joint PDFs are very compact, much more so than those from the IEM model or any of the mixing models studied

in [99]. The behavior observed is similar to that observed in the initial EMST development studies [19]. More interesting, however, is the location in composition space at which the dense PDFs occur. The PDFs are concentrated in the region of the slow manifold identified experimentally. Figure 4.9 demonstrates this through a scatter plot of particles from the calculations using EMST, onto which is overlaid the streamlines of conditional diffusion from the experiment. At all measured locations, the compositions yielded by the calculations using EMST lie almost directly on the slow manifold. This behavior suggests that the slow manifold exists at least in part due to mixing being local in composition space. Previous calculations of reacting flows in which the EMST mixing model yields more accurate calculations than the other mixing models [8, 9] are partially attributed to this behavior of the EMST mixing model, along with the sensitivity of the chemistry to the location in mixture fraction space. The PDFs and conditional diffusion also show a complete lack of the fast manifold observed in the experiments. This suggests that other physical processes not accounted for in the EMST model, for example, differential diffusion, molecular transport, and velocity-conditioned mixing, are possibly responsible for the fast manifolds.

One of the drawbacks of the EMST mixing model is that it does not satisfy the condition of linearity [19]; in the EMST mixing model, the evolution equations for the particle properties of scalars are changed when the scalars are linearly transformed. The calculations of this coaxial jet are found to be sensitive to how the composition is described when the EMST model is used. Typically, in these types of RANS-PDF calculations, the composition is described by the specific mole fractions (the mass fraction divided by the molecular weight) and the sensible enthalpy. However, this formulation results in scalar fields vastly different than what is observed with the other mixing models (IEM and MC).

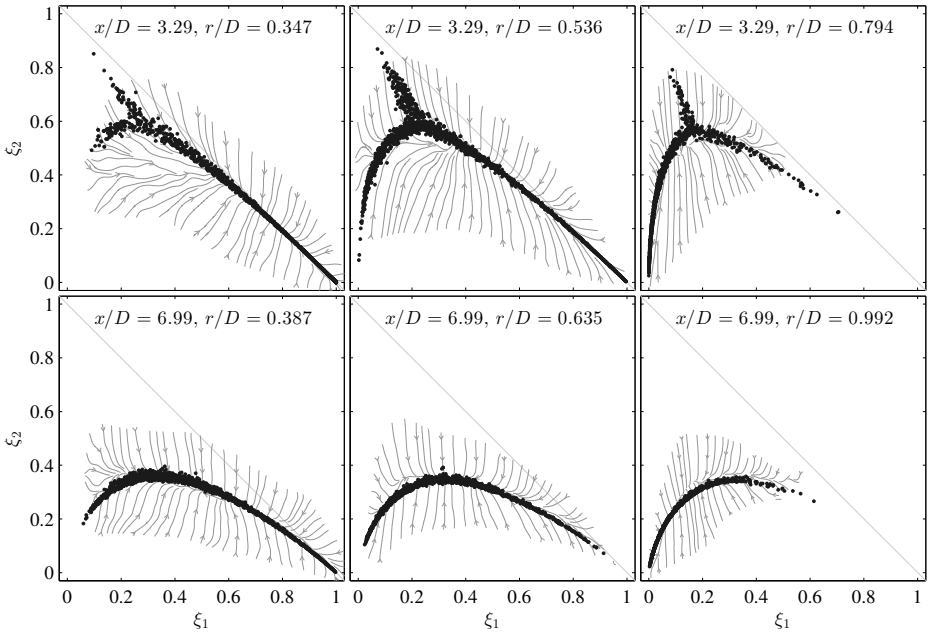

Figure 4.9: Particle scatter plots in mixture fraction space from the RANS-PDF calculations using the EMST mixing model overlaid onto the conditional diffusion streamlines from the experimental data.

This occurs because, in the specific mole composition space, the jet and coflow compositions are much closer to one another than to the annulus composition (as measured by the Euclidean norm). This biases the mixing between the jet and the coflow when the EMSTs are formed. To remedy this problem, the composition which undergoes mixing is defined to be the three mixture fractions. Figure 4.10 demonstrates why the latter formulation is more appropriate: when an EMST is formed using the original formulation (species specific moles), the EMSTs bias jet-coflow mixing; with the formulation used here (three mixture fractions), there is no bias between any pair of the three streams because the composition of each stream is equidistant in composition space from each other stream. This deficiency of the EMST mixing model must be called into consideration for multiple-stream mixing problems, particularly when the composition

of one stream is far in composition space from that of the other streams.

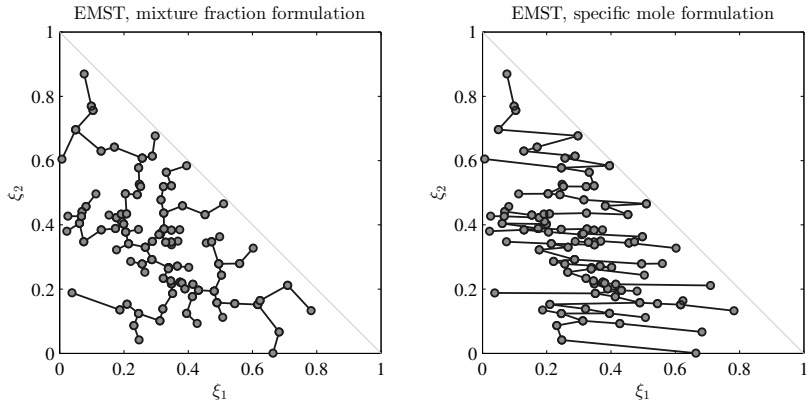

Figure 4.10: Example of EMSTs formed in mixture fraction space using the two different EMST formulations: On the left, the mixed composition variables are the three mixture fractions; On the right, the mixed variables are the specific moles of the four chemical species, C_3H_6O (acetone), C_2H_4 (ethylene), N_2, and O_2.

The RANS-PDF studies of these three mixing models demonstrate the strengths and weaknesses of each model in this flow. All three models yield mean and RMS statistics in good agreement with the experimental data, but only the EMST mixing model yields compositions on the slow manifold identified in the experimental study. There is room for improvement in the predictions of the joint PDFs; based on the comparisons between the results here and those in [99], the newly-developed IECM and PSP mixing models appear to be good candidates for improved performance.

4.4 LES calculations

In addition to RANS-based approaches, Large Eddy Simulation (LES) can also be used in conjunction with PDF methods. In LES, the large scales of the tur-

bulence are resolved, and the small scales must be modeled. Since the large scales contain most of the kinetic energy of the flow, most of the large-scale features of the flow can be resolved. The LES-PDF methodology has many benefits over RANS-PDF in that it can more robustly treat flows with complex geometry, recirculating or swirling flows, and unsteady flows. Additionally, an advantage of the LES-PDF methodology over pure LES is that chemical reaction can be treated without modeling; this is especially important for LES, where most chemical reaction takes place on the unresolved scales.

The primary purpose of this study is to examine the effects of modeling the molecular diffusion in LES-PDF; the LES calculations are used to set up the LES-PDF calculations, to gauge the significance of the grid resolution on the results, and to provide an intermediate comparison between the LES-PDF calculations and the experimental measurements. This intermediate comparison is particularly valuable here, where challenging experimental measurements (including the conditional diffusion and scalar dissipation rate) are made and must be evaluated carefully with respect to their own resolution.

4.4.1 LES methodology

In the LES performed here, a system of equations is solved for the resolved density-weighted velocity, $\widetilde{\mathbf{U}}$, and the resolved density, $\bar{\rho}$ [68]. These are the resolved equations for conservation of mass,

$$\frac{\partial \bar{\rho}}{\partial t} + \frac{\partial \bar{\rho} \widetilde{U}_j}{\partial x_j} = 0, \tag{4.4}$$

and conservation of momentum,

$$\frac{\partial \bar{\rho} \widetilde{U}_i}{\partial t} + \frac{\partial \bar{\rho} \widetilde{U}_i \widetilde{U}_j}{\partial x_j} = -\frac{\partial \bar{P}}{\partial x_i} + 2\frac{\partial}{\partial x_j}\left(\bar{\rho}\,(\widetilde{\nu} + \nu_T)\left(\widetilde{S}_{ij} - \frac{1}{3}\widetilde{S}_{kk}\delta_{ij}\right)\right). \tag{4.5}$$

where $\widetilde{\nu}$ is the resolved molecular viscosity, ν_T is the turbulent viscosity, and $\widetilde{S}_{ij}$ is the resolved strain rate. In this flow, there are two independent conserved scalar variables (the jet and the annulus mixture fractions, ξ_1 and ξ_2, respectively), so an additional transport equation,

$$\frac{\partial \bar{\rho}\widetilde{\xi}}{\partial t} + \frac{\partial \bar{\rho}\widetilde{U}_j\widetilde{\xi}}{\partial x_j} = \frac{\partial}{\partial x_j}\left(\bar{\rho}\left(\widetilde{\Gamma} + \Gamma_T\right)\frac{\partial \widetilde{\xi}}{\partial x_j}\right), \tag{4.6}$$

is solved for each density-weighted resolved mixture fraction, $\widetilde{\xi}$. In Eq. 4.6, $\widetilde{\Gamma}$ is the resolved molecular diffusivity of the mixture fraction, and Γ_T is the turbulent diffusivity. An additional transport equation for the variance of each mixture fraction, $V_\xi = \widetilde{\xi^2} - \left(\widetilde{\xi}\right)^2$, in the form of

$$\frac{\partial \bar{\rho}V_\xi}{\partial t} + \frac{\partial \bar{\rho}\widetilde{U}_j V_\xi}{\partial x_j} = \frac{\partial}{\partial x_j}\left(\bar{\rho}\left(\widetilde{\Gamma} + \Gamma_T\right)\frac{\partial V_\xi}{\partial x_j}\right) - \bar{\rho}\widetilde{\chi} + 2\bar{\rho}\left(\widetilde{\Gamma} + \Gamma_T\right)\frac{\partial \widetilde{\xi}}{\partial x_j}\frac{\partial \widetilde{\xi}}{\partial x_j}, \tag{4.7}$$

is solved for each scalar as well. In Eq. 4.7, $\widetilde{\chi}$ is the scalar dissipation rate, which is modeled here in a similar way as in [104, 108],

$$\widetilde{\chi} = 2\widetilde{\Gamma}\frac{\partial \tilde{\xi}}{\partial x_j}\frac{\partial \tilde{\xi}}{\partial x_j} + C\left(\frac{\Gamma_T + C_D\widetilde{\Gamma}}{\Delta^2}\right)V_\xi, \tag{4.8}$$

where Δ is the characteristic turbulence resolution scale. The standard value of 2.0 is used for the constant C as in [104], and a value of 2.0 is used for the constant C_D. The resolved density is computed from Eq. 4.2 based on the resolved mixture fractions. The turbulent viscosity is computed according to the dynamic procedure in [105, 106]; although the algebraic model in [72] is also assessed in this flow. The turbulent diffusivity is computed from the turbulent viscosity using a turbulent Schmidt number, Sc_T, of 0.4 as in other similar studies [104, 107, 109]. The molecular viscosity and molecular diffusivities are evaluated from second-order polynomial curve-fits to data from Chemkin's Tranlib, in the form of

$$\nu = \nu_0\left(a_1 + a_2\xi_1 + a_3\xi_2 + a_4\xi_1^2 + a_5\xi_2^2 + a_6\xi_1\xi_2\right) \tag{4.9}$$

for the molecular viscosity, and

$$\Gamma = \Gamma_0 \left(a_1 + a_2\xi_1 + a_3\xi_2 + a_4\xi_1^2 + a_5\xi_2^2 + a_6\xi_1\xi_2 \right) \tag{4.10}$$

for each molecular diffusivity. The fitting error is less than 2%. The coefficients used in the curve-fits are shown in Table 4.3.

		a_1	a_2	a_3	a_4	a_5	a_6
ν	$\nu_0 = 15.9\times10^{-6}$ m^2/s	1.00	-0.165	-0.618	0.009	0.179	0.087
Γ_1	$\Gamma_{10} = 9.79\times10^{-6}$ m^2/s	1.00	-0.067	-0.363	-0.001	0.099	-0.015
Γ_2	$\Gamma_{20} = 16.1\times10^{-6}$ m^2/s	1.00	-0.079	0.041	0.002	-0.019	-0.037

Table 4.3: Coefficients to curve-fits for molecular viscosity and molecular diffusivities of jet and annulus mixture fractions.

In the experimental work, constant values are used for the diffusivity of acetone, Γ_1^e, and ethylene, Γ_2^e to evaluate the conditional diffusion and scalar dissipation rates. These values, which are obtained from experimental correlations, are $\Gamma_1^e = 10.4\times10^{-6}$ m^2/s and $\Gamma_2^e = 14.7\times10^{-6}$ m^2/s. For acetone, Γ_1^e is in reasonable agreement with the value computed here numerically at the composition of the coflow (air), where $\Gamma_1(\xi_1{=}0, \xi_2{=}0) = 9.79\times10^{-6}$ m^2/s. Elsewhere in composition space, there is as much as 30% variation in Γ_1. For ethylene, Γ_2^e is in very good agreement to the numerically computed value at the composition of the jet (air and acetone), where $\Gamma_2(\xi_1{=}1, \xi_2{=}0) = 14.8\times10^{-6}$ m^2/s. The variation of Γ_2 in composition space is less than that of Γ_1, with a maximum variation of about 10%.

Contour plots of the density, molecular kinematic viscosity, and molecular diffusivities of both mixture fractions are shown in Figure 4.11 as functions of mixture fraction. The variation of each property in composition space is evident, with the molecular viscosity varying by as much as 80%.

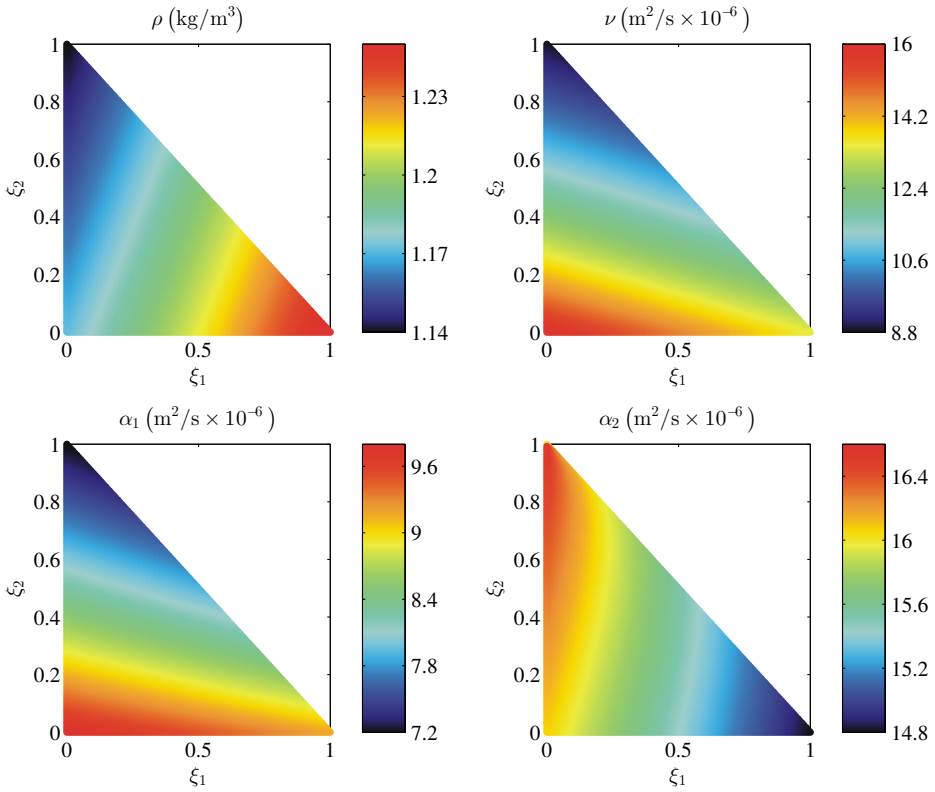

Figure 4.11: Contour plots of density, kinematic viscosity, and molecular diffusivity as functions of mixture fraction for the LES calculations. Color online only.

4.4.2 Computational configuration

The system of equations described in Sec. 4.4.1 is solved on a cylindrical computational domain of size $54D\times13.5D\times2\pi$ in the axial, radial, and circumferential directions (with dimensions in the axial and radial directions equivalent to those in the RANS-PDF calculations). The equations are solved using a second-order accurate numerical method [71]. A sketch of the computational domain is shown in Figure 4.12. As illustrated in the figure, the domain begins at the jet exit plane and extends downstream in the axial direction.

Inflow boundary conditions for the central jet are provided from separate

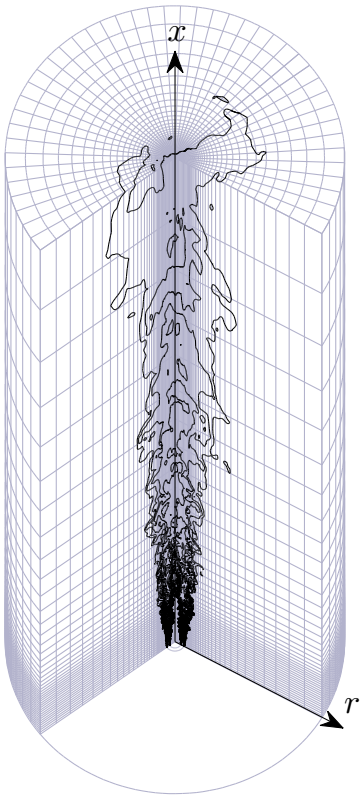

Figure 4.12: Sketch of the LES domain. In the axial and radial directions, only one eighth of the grid cells from grid G-D are shown. Contour lines of the resolved annulus mixture fraction are shown in the cutaway.

high-resolution LES calculations of a fully-developed pipe flow at a Reynolds number of 14,300, based on the jet bulk velocity, diameter, and viscosity as in Table 4.1. For the annulus stream, the same procedure is performed using an annular geometry, with the properties of the annulus stream in Table 4.1. For the coflow, a laminar boundary condition is prescribed identical to that in the RANS-PDF calculations. At the other boundaries, convective boundary conditions are employed for scalar and velocity fields.

One important modeling difference is that the jet wall, whose width is reasonably large at $0.073D$, is instead modeled as having zero thickness; the dimensions of the jet width remain unchanged, and the effective inner radius of the annulus is decreased. This decision is made based on convergence studies performed in both geometries. In the calculations including the jet wall thickness, the calculations fail to reach satisfactory numerical convergence on all of the examined grid sizes. In the calculations with the infinitesimally thin jet wall, the calculations reach sufficient convergence of the mean fields on moderate grid sizes. This modeling assumption results in predictions of the annulus mixture fraction being slightly too large at some locations. However, in these calculations it is more desirable to have sufficient numerical convergence in light of the type of comparisons being made.

In the LES calculations, the joint PDF of the resolved mixture fractions is computed at the same locations as in the RANS-PDF calculations. The resolved and modeled scalar dissipation rates for both mixture fractions are computed as in Eq. 4.8 using second-order central differences in both the two components (as performed in the experiment [95]) and in the full three components. Both the total conditional diffusion,

$$D_T = \langle (1/\bar{\rho}) \nabla \left(\bar{\rho} \left(\widetilde{\Gamma} + \Gamma_T \right) \nabla \widetilde{\xi} \right) | \widetilde{\xi} = \hat{\xi} \rangle, \tag{4.11}$$

and the constant-property resolved conditional diffusion,

$$D_R = \langle \widetilde{\Gamma} \nabla^2 \widetilde{\xi} | \widetilde{\xi} = \hat{\xi} \rangle, \tag{4.12}$$

are computed at the same locations for both mixture fractions using second-order central differences, again in both two and three components. The calculations are run at a constant CFL number of 0.2 and the statistics of interest are time-averaged over at least 10 flow-through times after a statistically stationary

state is reached; a flow-through time is based on the jet bulk velocity and the entire extent of the domain in the axial direction.

4.4.3 Numerical accuracy

The LES solution depends strongly on the resolution with which it is computed. Therefore, it is important to quantify the extent to which the solution is resolved, and to understand how the resolution affects the statistics of interest. To examine the numerical accuracy of the calculations, a grid resolution study is conducted on six grids, named from Grid-A to Grid-F, whose sizes range from 0.5 million cells to 33 million cells. Contours of the instantaneous resolved jet and annulus mixture fractions are shown from calculations on three of the grids in Figure 4.13, alongside an instantaneous image obtained experimentally in [95].

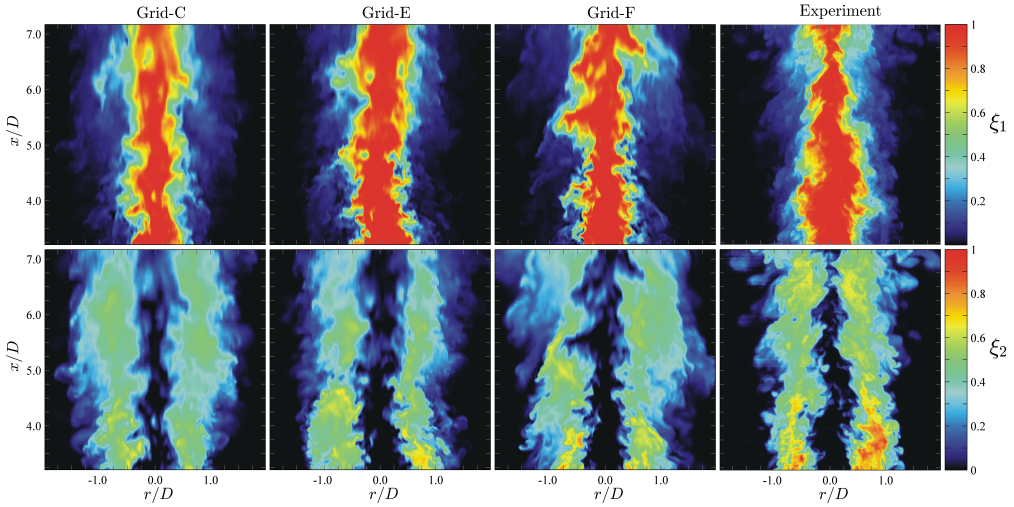

Figure 4.13: Contour plots of instantaneous resolved mixture fractions of the jet (top plots) and pilot (bottom plots) in the LES convergence study and from experimental data. Color online only.

While the large-scale features of the flow are similar among the three grids

and the experimental data, there is a clear difference in the resolution of the small-scale features of the flow. On the finest grid, Grid-F, the resolution is similar to that of the experiment for the region near the exit plane (around x/D=3.5), but farther downstream it is evident that even the finest grid does not fully resolve the small-scale structures observed at the experimental resolution. Figure 4.14 illustrates the large dependence of the resolved scalar dissipation rate (here for the annulus mixture fraction) on the grid resolution.

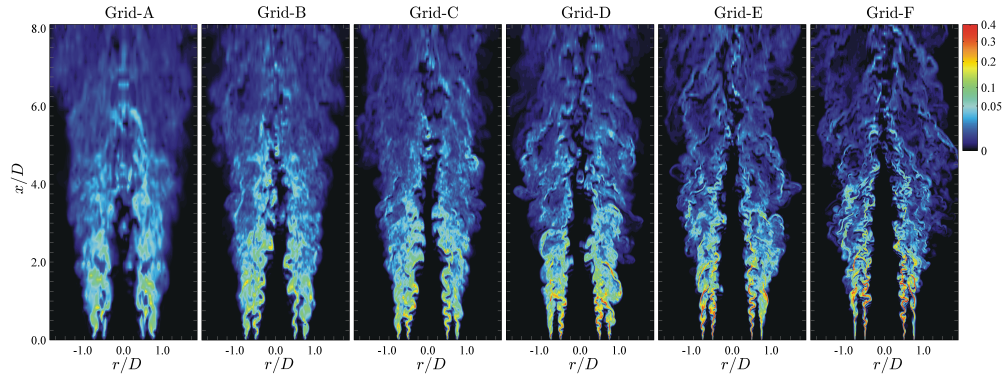

Figure 4.14: Contour plots of instantaneous resolved scalar dissipation rate of the annulus mixture fractions for each grid used in the LES convergence study. Units are in s^{-1}. Color online only.

Each grid used in the LES calculations is a structured, tensor-product grid. In the region of the near-field ($0 \leq x/D \leq 4.0, 0 \leq r/D \leq 1.4$), the grid spacing is uniform. From the outer boundary of this region, the grid is stretched to each edge of the computational domain with a constant stretching ratio of 4 % in each direction. Table 4.4 shows the size of each grid, along with the error in the resolved mixture fractions (ϵ_{M1} and ϵ_{M2}), the error in the resolved RMS (ϵ^R_{R1} and ϵ^R_{R2}), and the error in the total RMS (ϵ^T_{R1} and ϵ^T_{R2}). These errors are computed for each grid by taking the maximum value of the difference between the statistics on that grid, and the statistics on the most highly-resolved grid within the region of interest ($3.29 \leq x/D \leq 6.99$). The convergence is relatively slow, and not until Grid-E do the

statistics reach roughly the same numerical error as in the experiment, around 2%.

Grid Name	n_x	n_r	n_θ	n_T	ϵ_{M1}	ϵ_{M2}	ϵ^R_{R1}	ϵ^R_{R2}	ϵ^T_{R1}	ϵ^T_{R2}
G-A	128	128	32	0.524	0.132	0.087	0.151	0.124	0.073	0.058
G-B	192	192	96	1.77	0.073	0.075	0.098	0.102	0.072	0.041
G-C	256	256	64	4.19	0.053	0.060	0.064	0.066	0.062	0.032
G-D	320	320	80	8.19	0.022	0.034	0.029	0.030	0.044	0.020
G-E	384	384	96	14.2	0.008	0.010	0.025	0.017	0.019	0.012
G-F	512	512	128	33.6	–	–	–	–	–	–

Table 4.4: Grid sizes (number of cells in x, r, and θ, and total number of cells in millions, n_T) and errors in the mixture fraction statistics (resolved means, RMS of resolved fields, total RMS) from convergence tests of the LES-PDF calculations.

The results of the LES grid convergence study are summarized in Figure 4.15, where the radial profiles of time-averaged density-weighted mean and RMS statistics of both mixture fractions are shown for three grids and for the experimental data. The agreement between the most highly resolved LES calculations (Grid-F) and the experimental data is very good. The mean annulus mixture fraction is slightly overpredicted due to the thin-wall modeling assumption discussed in Sec. 4.4.2. The total RMS on Grid-F is slightly overpredicted, mostly in the near-field around the jet-annulus mixing layer. This occurs due to both the modeling of the scalar dissipation rate and the high resolution requirements in the near-field of the jet. As the grid is refined, the statistics generally converge monotonically to the values on the finest grid. The total RMS decreases toward the resolved RMS as the grid is refined.

The results of the grid convergence study are further analyzed through Figures 4.16–4.19, which show statistics at various points as functions of the local grid resolution for all six grids, Grid-A to Grid-F, and the experimental data.

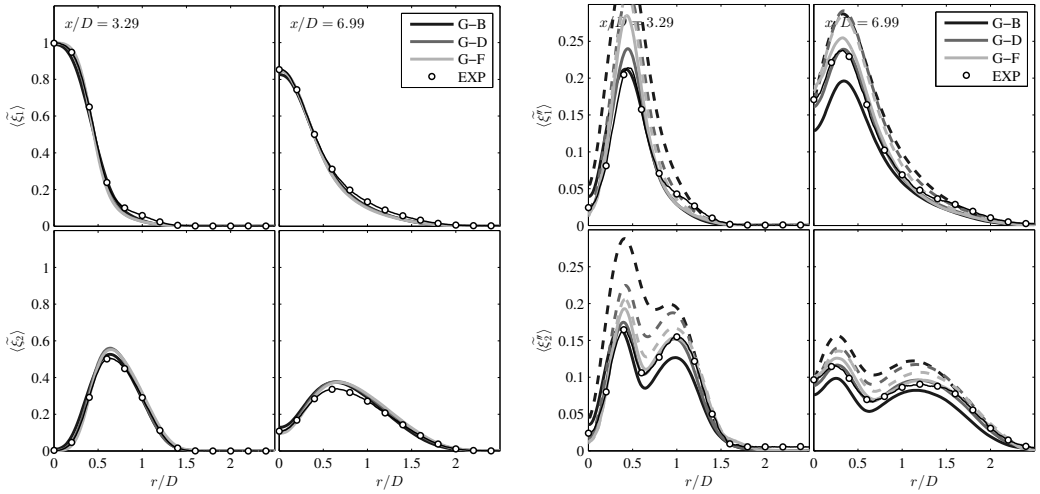

Figure 4.15: Radial profiles of time-averaged mass-weighted mean (a) and RMS (b) mixture fractions in the LES grid convergence study. Dark line: Grid G-B; Dark gray line: Grid G-D; Light gray line: Grid G-F; Solid lines: resolved statistics; Dashed lines: Total (resolved plus modeled) statistics; Circles: experimental data [95].

The resolution, Δ, used in the plots is defined equivalently for the experimental data and calculations: in both cases, $\Delta = \sqrt{\Delta x^2 + \Delta r^2}$, where the local grid spacing (or image resolution) in the axial direction is Δx, and in the radial direction is Δr. This definition of Δ is used in these plots so that the experiments and calculations can be compared to one another with an equivalent definition for the resolution. It must be noted that the Δ defined here is not equal to the turbulence resolution scale used in the LES calculations (although they are closely related).

Figure 4.16 shows the mean resolved mixture fractions as a function of the grid resolution. These statistics are generally not very sensitive to the grid resolution beyond the most coarse grid, Grid-A. Besides the slight overprediction of the annulus mixture fraction, these statistics are all in good agreement with

the experimental data for Grid-B and finer. The resolution of the calculations for Grid-F is higher than that of the calculations at x/D=3.29; due to the grid stretching that occurs beyond x/D=4, the calculations on Grid-F are at a lower resolution than the experiments farther downstream at x/D=6.99. These quantitative assessments of the resolution are consistent with the qualitative comparisons of the instantaneous resolved fields in Figure 4.13.

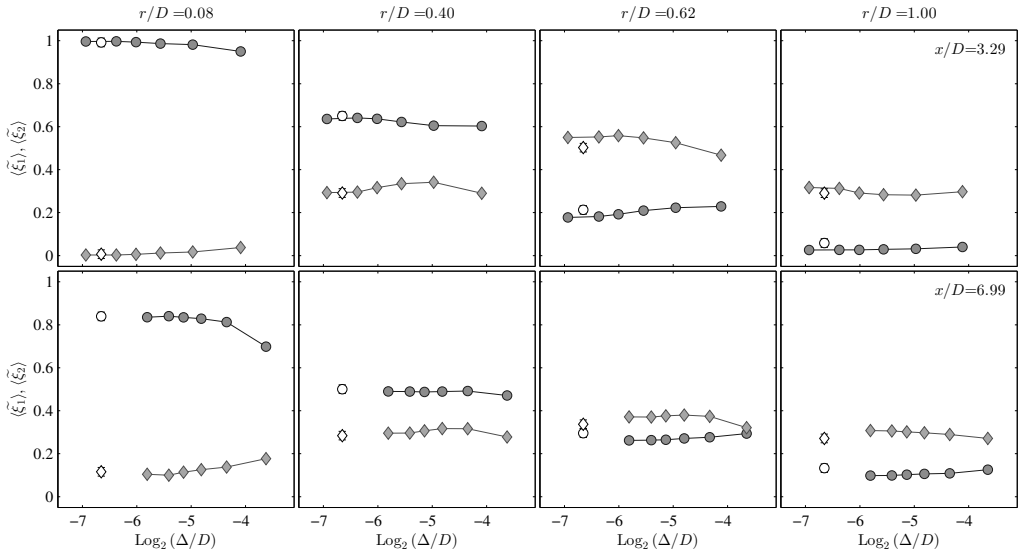

Figure 4.16: Convergence of the time-averaged density-weighted mean resolved mixture fractions at eight locations in the flow. Circles: jet mixture fraction; Diamonds: annulus mixture fraction; Solid symbols: LES calculations; Open symbols: experimental data [95].

The next figures, Figures 4.17-4.18, show the RMS of the jet and annulus mixture fractions, respectively. As the grid is refined, the portion of the RMS which is modeled approaches zero, and the total RMS is nearly equal to the resolved portion of the RMS. As observed in Figure 4.15, the RMS of the jet mixture fraction is overpredicted at the jet-annulus mixing layer, $(x/D, r/D)$ =(3.29, 0.40). At this location, the modeled portion of the RMS is about 10% of the total RMS and the total RMS has changed little between the three finest grids. Therefore,

this overprediction in the RMS is not necessarily caused by under-resolution. Modeling errors which can affect the calculations in the near-field, such as the modeling of the inflow boundary conditions, are also a likely cause of this overprediction. Farther downstream at x/D=6.99, the agreement between the RMS of the jet mixture fraction in the calculations and the experiments is better, even though the resolution in the calculations is comparatively lower. This shows that the LES is performing well in this region of the flow. For the RMS of the annulus mixture fraction in Figure 4.18, the agreement with the experimental data is slightly better and indicates convergence toward the experimentally measured values. In general, the convergence of the RMS statistics is slower than that of the mean statistics, with reasonable convergence being achieved not until Grid-D or Grid-E.

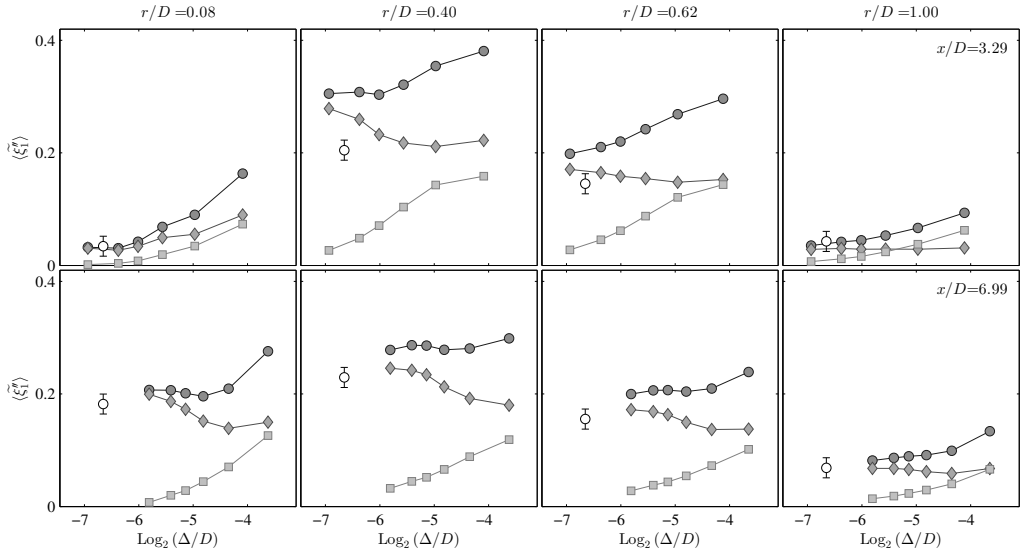

Figure 4.17: Convergence of the time-averaged density-weighted RMS jet mixture fraction at eight locations in the flow. Circles: total RMS; Diamonds: resolved RMS; Squares: modeled RMS; Solid symbols: LES calculations; Open symbols: experimental data [95].

Figure 4.19 shows the time-averaged molecular viscosity and molecular dif-

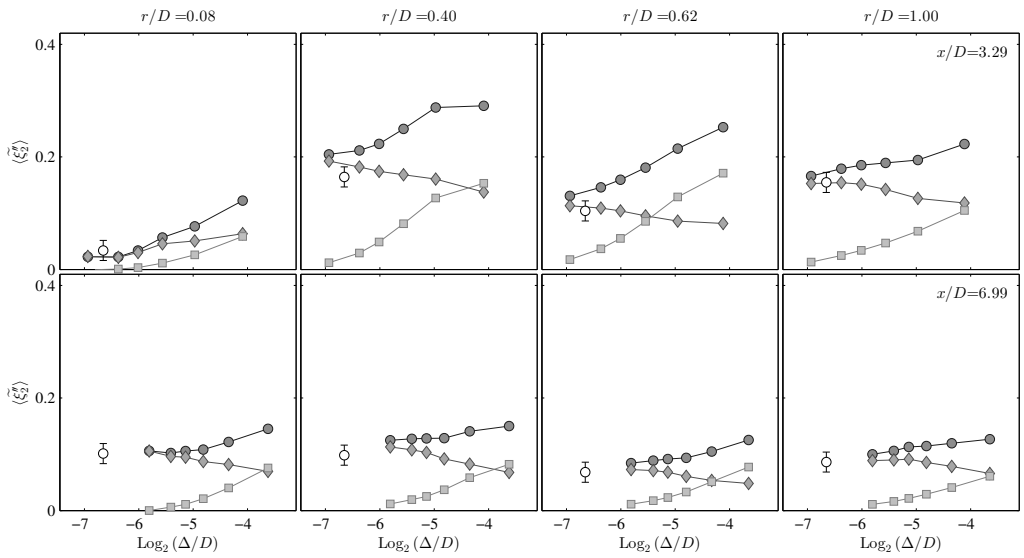

Figure 4.18: Convergence of the time-averaged density-weighted RMS annulus mixture fraction at eight locations in the flow. Circles: total RMS; Diamonds: resolved RMS; Squares: modeled RMS; Solid symbols: LES calculations; Open symbols: experimental data [95].

fusivities as fractions of the total viscosity and diffusivity. At the centerline of the inflow boundary, the Kolmogorov scale, η, is estimated to be 63 μm (equivalent to $\log_2(\eta/D) = -6.5$ on the horizontal axis of Figure 4.19) in the experimental work [95] based on extrapolation from experimental data. This is reasonably close to the grid resolution at which the turbulent diffusivity goes to zero at a location of $(x/D, r/D)$=(3.29, 0.08). Classical scaling of the flow's smallest length scales based on the Reynolds number of the jet, $\eta/D \sim Re^{-3/4}$, yields η on the order of 4.2 μm (or $\log_2(\eta/D) \sim -10.4$ on the horizontal axis of Figure 4.19). This is far smaller than any of the resolution scales encountered in either the experiment or the calculations; based on linear extrapolation from the grid resolution study, it appears to be a reasonable approximation around r/D=0.62 and r/D=1.00, near the middle of the jet-annulus and annulus-coflow mixing layers.

Figure 4.19, in conjunction with Figures 4.16-4.18, conveys the efficacy of

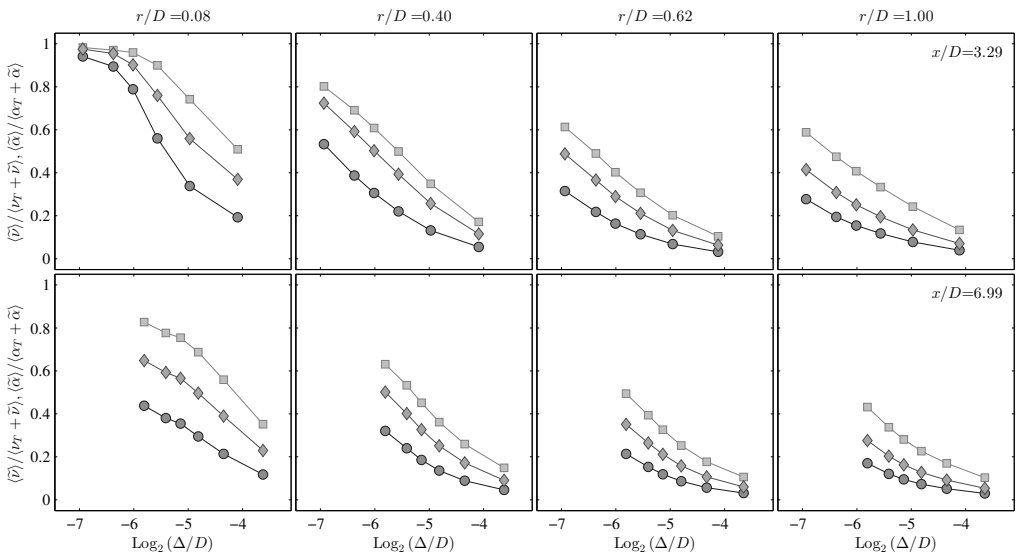

Figure 4.19: Convergence of the time-averaged molecular viscosity and molecular diffusivities as fractions of the total (molecular plus turbulent) viscosity and diffusivity, plotted as functions of the grid length scale. Squares: molecular viscosity; Circles: molecular diffusivity of acetone; Diamonds: molecular diffusivity of ethylene.

LES: with less than 20% of the molecular diffusivity resolved, accurate calculations of the mean statistics are achieved; with less than 40% of the molecular diffusivity resolved, accurate calculations of the RMS statistics are achieved; accurate calculations of these statistics are achieved with a grid resolution scale more than 10 times greater than the order estimate of the smallest Kolmogorov scales.

4.4.4 Scalar dissipation rate and conditional diffusion

As mentioned in Sec. 4.2, one of the highlights of the experimental work is performing the challenging measurements of the scalar dissipation rate and conditional diffusion. In the experiment, the resolved conditional scalar dissipation

rate,

$$\widetilde{\chi}_R = 2\Gamma \frac{\partial \tilde{\xi}}{\partial x_j} \frac{\partial \tilde{\xi}}{\partial x_j}, \tag{4.13}$$

is computed in two-dimensions from the planar imaging measurements. This same quantity is also calculated from the LES as mentioned in Sec. 4.4.2. Figure 4.20 compares this quantity for calculations on all six LES grids and the experimental measurements. It is clear from the figure that this quantity is extremely dependent on the grid resolution, which is expected since Eq. 4.13 depends on the square of gradient fields. The form of $\widetilde{\chi}_R$ is qualitatively the same in the experiments and in the calculations; for the jet mixture fraction, there is a peak in the scalar dissipation rate near the jet-annulus mixing layer; for the annulus mixture fraction, there are two peaks, corresponding to the jet-annulus and annulus-coflow mixing layers.

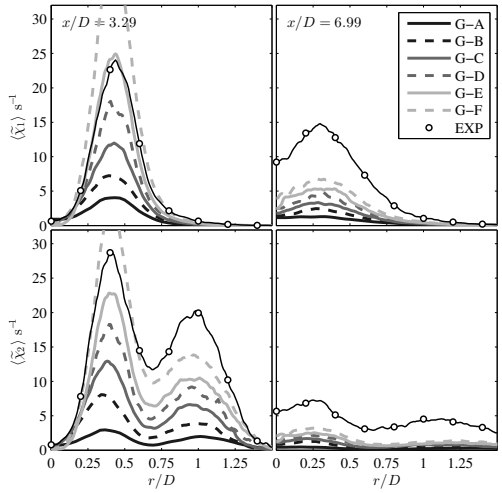

Figure 4.20: Radial profiles of the time-averaged two-dimensional scalar dissipation rates of resolved jet (top) and annulus (bottom) mixture fractions: Solid and dashed lines: LES calculations on all six grids; Open circles: experimental measurements [95].

The differences that occur between the experimental measurements and the calculations on Grid-F are attributed to a number of factors. These factors in-

clude:

1. *Under-resolution of the calculations* – Keeping in mind the resolution quality as discussed in Sec. 4.4.3, at $x/D = 6.99$, the resolution scale of the calculations on Grid-F is more coarse than that of the experiments by a factor of about two. The scalar dissipation rate here is under-estimated in the calculations.
2. *Under-resolution of the experimental measurements* – At $x/D = 3.29$, where the scalar dissipation rate in the experiments is less than that of the LES on Grid-F, the resolution scale of the calculations on Grid-F is finer than that of the experiments by a factor of 1.4.
3. *Additional numerical procedures undertaken in the experiments* – In the experiments, high order differences are used to calculate the scalar dissipation (tenth-order versus second-order), conditional sampling techniques are used to improve the resolution, and noise-correction procedures are performed on the experimental data. Based on the sensitivity of this quantity to the grid resolution, this factor is not a likely cause of the differences observed.
4. *Experimental noise* – The experimental measurement noise is clearly evident from the non-realizable values of mixture fraction in the plots of conditional diffusion later in this section. The contribution of the experimental noise to the differences observed here is most likely small, as [95] has shown the effects of noise-reduction applied to the measurements and it is far less than the differences observed here.

Figure 4.21 shows total scalar dissipation rate, $\widetilde{\chi}$, from Eq. 4.8 from the LES calculations. Compared to $\widetilde{\chi}_R$, there is much less sensitivity of $\widetilde{\chi}$ to the grid res-

olution. The modeled portion of the total scalar dissipation rate is large; even on Grid-F, as much as 90% of the total dissipation is from the model. The time-averaged scalar dissipation rate from the RANS-PDF equations, which is modeled by

$$\langle \chi \rangle = C_\phi \langle \omega \rangle V_\xi^T \tag{4.14}$$

where $\langle \omega \rangle$ is the time-averaged turbulence frequency, and V_ξ^T is the variance of the mixture fraction, is also shown in Figure 4.21. Both models for the total scalar dissipation rate are considerably larger than the values measured experimentally. Along with the observation from Figure 4.20 that the resolved portion of the scalar dissipation rate is still sensitive to the grid resolution on the finest grid and giving no indication of convergence, Figure 4.21 suggests that the scalar dissipation rates measured experimentally are not fully resolved. Even with the fine resolution used in the experiments, Figures 4.20 and 4.21 indicate that assessments of these measurements need to take into account the resolution at which the measurements are made.

A second observation from Figure 4.21 is the very sharp peak in the total scalar dissipation rate from the LES calculations at the centerline, r/D=0. This is observed when using both the dynamic model [105, 106] and the algebraic model [72] (not shown) for the turbulent viscosity, ν_T. An inspection of each calculation shows that this behavior occurs due to the quantity Γ_T/Δ^2. This demonstrates the need for improved models in LES for ν_T (which, in this study, is directly proportional to Γ_T by the turbulent Schmidt number) or the scalar dissipation rate. As this observed behavior is most likely a numerical artifact caused by the very small filter widths at the centerline, an alternate definition of the filter width used in the model for the scalar dissipation is a potential remedy.

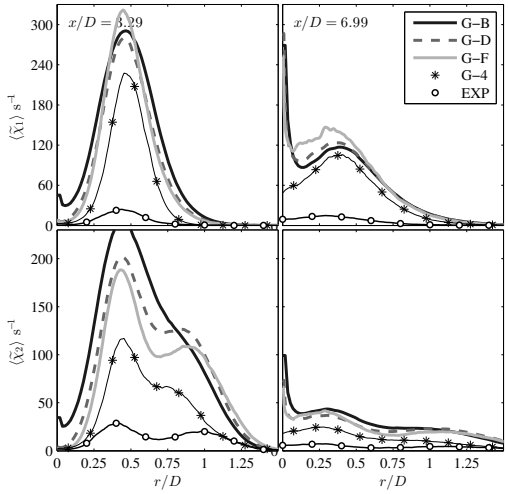

Figure 4.21: Radial profiles of the time-averaged total scalar dissipation rates of the jet (top) and annulus (bottom) mixture fractions: Solid and dashed lines: LES calculations on three grids; Stars: RANS-PDF calculations; Open circles: experimental measurements [95].

The LES study is concluded by presenting the calculations of the conditional diffusion and comparing these to the experimentally measured values. In the experimental work, the constant-property resolved conditional diffusion from Eq. 4.12 is computed in the two-dimensional image plane. This same measurement is made in the LES calculations (although using only second-order central differences to calculate the gradients, instead of tenth-order, as in the experiment). The results are shown in Figure 4.22 for three different LES grids at one location, $(x/D, r/D) = (3.29, 0.536)$. In the previous figures of the conditional diffusion (Figures 4.7 and 4.8), only the magnitude and streamlines are shown; here contour plots show each component of the conditional diffusion. This allows a more direct comparison to be made regarding the form of the conditional diffusion in composition space.

As expected, there is large grid dependency in this quantity as well. For all

grids, the qualitative form of the conditional diffusion is very similar; generally only the magnitude appears to be strongly influenced by the grid resolution. Note that the color scale in Figure 4.22 is different on the left two plots for the more coarse grids. On the finest grid, Grid-F, there is reasonable quantitative agreement in the values of conditional diffusion with the experimentally measured values. At some locations in composition space at which there are large differences between the experimental values and those computed on Grid-F, the measured composition is actually non-realizable (i.e., a sum of mixture fractions greater than unity); the only reason for a value of the conditional diffusion existing at these compositions is due to measurement noise. It is conceivable then, that at least some of the differences between the measurements of the conditional diffusion and the LES calculations on Grid-F are due to measurement error.

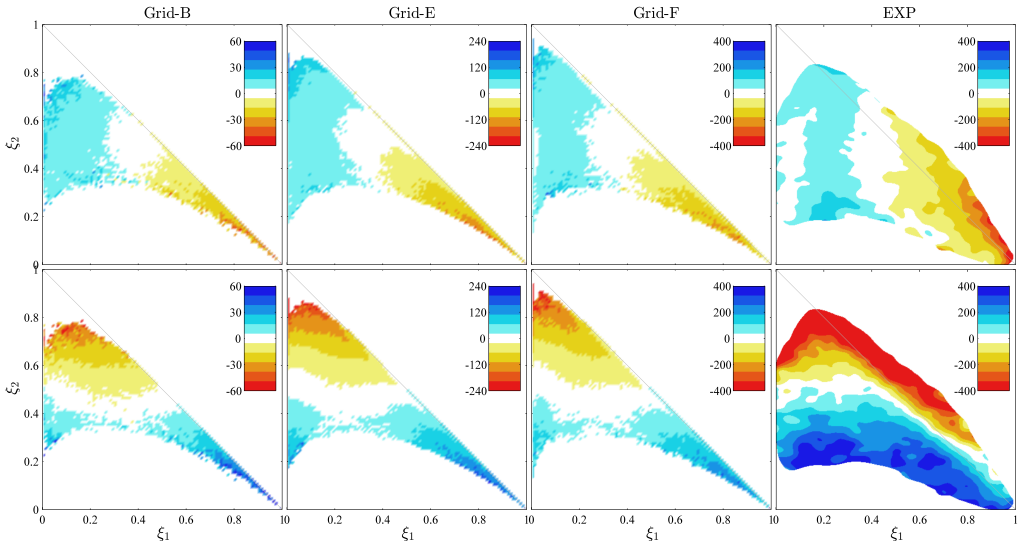

Figure 4.22: Contour plots of the constant-property resolved conditional diffusion, D_R, from LES calculations on three grid (leftmost three columns) and the experimentally measured conditional diffusion [95] (right column) for the jet (top) and annulus (bottom) mixture fractions. The units are s^{-1}, and the location is $(x/D, r/D) = (3.29, 0.536)$. Color online only.

Whereas Figure 4.22 examined only the resolved, constant-property, two-dimensional conditional diffusion, Figure 4.23 shows the total conditional diffusion, from Eq. 4.11 in all three dimensions with the same color scale on each plot. It is found from the calculations that the largest contribution to the differences between the values in Figure 4.22 and those in Figure 4.23 is the addition of the modeled portion of the conditional diffusion (by adding the turbulent diffusivity); the additional third-dimensional component and the inclusion of the variable properties (both of which are not considered in the experimental measurements) account for a difference of only about 10% at most.

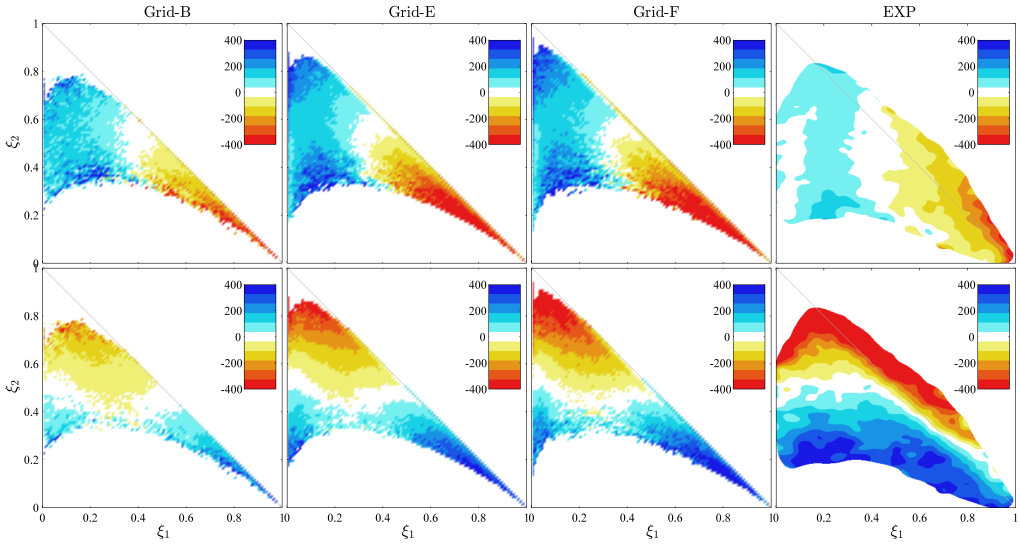

Figure 4.23: Contour plots of the total conditional diffusion, D_T, from LES calculations on three grid (leftmost three columns) and the experimentally measured conditional diffusion [95] (right column) for the jet (top) and annulus (bottom) mixture fractions. The units are s^{-1}, and the location is $(x/D, r/D) = (3.29, 0.536)$. Color online only.

There is much less sensitivity of the total conditional diffusion to the grid resolution since the modeled portion is accounted for. This allows even the coarse grids to yield a magnitude of the conditional diffusion which is close to

the experimental measurement. Due to the form of the turbulent diffusivity, the structure of the conditional diffusion in composition space changes slightly from that of the resolved conditional diffusion; for example, in the region of the jet composition, the turbulent diffusivity is large, which results in a calculation of the conditional diffusion being considerably larger than what is measured experimentally. It is not immediately clear whether the addition of the turbulent diffusivity results in inaccurate total conditional diffusion in the LES calculations due to its modeling, or if the experimental measurements (which do not consider any turbulent diffusivity because they only contain the resolved portion of the conditional diffusion) are under-resolved. The results from Figures 4.20 and 4.21 suggest the latter is more responsible, but more conclusive tests must be performed before concluding so.

4.5 LES-PDF calculations

4.5.1 LES-PDF methodology

The LES-PDF methodology, which combines many of the advantages of LES (discussed in Sec. 4.4) with the advantages of the PDF method (discussed in Sec. 4.1), is next applied to this non-reacting flow to study the modeling of mixing in LES-PDF. The LES-PDF methodology involves a hybrid finite-volume and particle solver. The finite-volume solver in this case is LES, and solves the same equations as described in Sec. 4.4.1, except for the density equation. The density in the LES is computed from the particle solver through the transported specific volume method [73]. In the particle solver, particles evolve in position

according to

$$d\mathbf{X}^*(t) = \left(\widetilde{\mathbf{U}} + \frac{1}{\bar{\rho}}\nabla\left(\bar{\rho}\Gamma_R\right)\right)^* dt + \sqrt{2\Gamma_R^*}d\mathbf{W}, \tag{4.15}$$

and in composition as

$$d\phi^*(t) = -\Omega_M^*\left(\phi^* - \tilde{\phi}^*\right)dt + \left(\frac{1}{\bar{\rho}}\nabla\cdot\left(\bar{\rho}\Gamma_M\nabla\tilde{\phi}\right)\right)^* dt, \tag{4.16}$$

where Ω_M, the mixing frequency, is defined as

$$\Omega_M = C_M\left(\frac{\Gamma_M + \Gamma_R}{\Delta^2}\right). \tag{4.17}$$

The terms Γ_R and Γ_M represent the diffusivities for the random walk and the mean drift, respectively. Typically, the diffusivity for the random walk, Γ_R, is taken to be equal to the turbulent diffusivity, Γ_T, while the diffusivity for the mean drift, Γ_M is taken be equal to the resolved molecular diffusivity, $\tilde{\Gamma}$. The position equation, Eq. 4.15, is solved with second-order accuracy in space and time [69]. The implementation of molecular diffusion in Eq. 4.16 [57, 58] is unique in that it yields no spurious production of variance from molecular diffusion, and it can include the effects of differential diffusion.

The mass-weighted LES PDF of the composition is denoted as $\tilde{f}_\phi(\psi;\mathbf{X},t)$, where ψ is a sample-space variable for the composition. Eqs. 4.15–4.17 correspond to an equation for the evolution of the PDF, $\tilde{f}_\phi$, as

$$\frac{\partial\bar{\rho}\tilde{f}_\phi}{\partial t} + \frac{\partial}{\partial x_j}\left(\bar{\rho}\tilde{f}_\phi\widetilde{U}_j\right) = \frac{\partial}{\partial x_j}\left(\bar{\rho}\Gamma_R\frac{\partial}{\partial x_j}\tilde{f}_\phi\right) + \frac{\partial}{\partial\psi}\left(\bar{\rho}\tilde{f}_\phi\Omega_M\left(\psi - \widetilde{\phi}\right)\right) - \frac{\partial}{\partial\psi}\left(\tilde{f}_\phi\frac{\partial}{\partial x_j}\left(\bar{\rho}\Gamma_M\frac{\partial\widetilde{\phi}}{\partial x_j}\right)\right). \tag{4.18}$$

Taking the first moment of Eq. 4.18, the transport equation for the resolved composition is

$$\frac{\partial\bar{\rho}\widetilde{\phi}}{\partial t} + \frac{\partial\bar{\rho}\widetilde{U}_j\widetilde{\phi}}{\partial x_j} = \frac{\partial}{\partial x_j}\left(\bar{\rho}\left(\Gamma_R + \Gamma_M\right)\frac{\partial\widetilde{\phi}}{\partial x_j}\right). \tag{4.19}$$

Similarly, taking the second moment of Eq. 4.18 gives the transport equation for

the resolved square of the composition to be

$$\frac{\partial \bar{\rho}\widetilde{\phi^2}}{\partial t} + \frac{\partial \bar{\rho}\widetilde{U}_j\widetilde{\phi^2}}{\partial x_j} = \frac{\partial}{\partial x_j}\left(\bar{\rho}\Gamma_R\frac{\partial \widetilde{\phi^2}}{\partial x_j}\right) + 2\widetilde{\phi}\frac{\partial}{\partial x_j}\left(\bar{\rho}\Gamma_M\frac{\partial \widetilde{\phi}}{\partial x_j}\right) - 2\bar{\rho}\Omega_M\left(\widetilde{\phi^2} - \left(\widetilde{\phi}\right)^2\right). \quad (4.20)$$

The transport equation for the modeled variance, $V_\phi = \widetilde{\phi^2} - \left(\widetilde{\phi}\right)^2$, is obtained from Eqs. 4.19 and 4.20, and it is

$$\frac{\partial \bar{\rho}V_\phi}{\partial t} + \frac{\partial \bar{\rho}\widetilde{U}_jV_\phi}{\partial x_j} = \frac{\partial}{\partial x_j}\left(\bar{\rho}\Gamma_R\frac{\partial V_\phi}{\partial x_j}\right) - 2\bar{\rho}\Omega_M V_\phi + 2\bar{\rho}\Gamma_R\frac{\partial \widetilde{\phi}}{\partial x_j}\frac{\partial \widetilde{\phi}}{\partial x_j}. \quad (4.21)$$

In this work, the diffusivities Γ_R and Γ_M are related to the turbulent diffusivity, Γ_T, and the molecular diffusivity, $\widetilde{\Gamma}$, through the model constant β ($0 \le \beta \le 1$) as

$$\Gamma_R = \Gamma_T - \beta\Gamma_T \quad (4.22)$$

and

$$\Gamma_M = \widetilde{\Gamma} + \beta\Gamma_T. \quad (4.23)$$

With these specifications, the transport equation for the resolved composition (Eq. 4.19) takes the standard form

$$\frac{\partial \bar{\rho}\widetilde{\phi}}{\partial t} + \frac{\partial \bar{\rho}\widetilde{U}_j\widetilde{\phi}}{\partial x_j} = \frac{\partial}{\partial x_j}\left(\bar{\rho}\left(\widetilde{\Gamma} + \Gamma_T\right)\frac{\partial \widetilde{\phi}}{\partial x_j}\right), \quad (4.24)$$

independent of the value of β; and the resolved variance equation (Eq. 4.21) can be written

$$\frac{\partial \bar{\rho}V_\phi}{\partial t} + \frac{\partial \bar{\rho}\widetilde{U}_jV_\phi}{\partial x_j} = \frac{\partial}{\partial x_j}\left(\bar{\rho}\Gamma_R\frac{\partial V_\phi}{\partial x_j}\right) + 2\bar{\rho}\Gamma_T\frac{\partial \widetilde{\phi}}{\partial x_j}\frac{\partial \widetilde{\phi}}{\partial x_j} - \bar{\rho}\widetilde{\chi}_M \quad (4.25)$$

where $\widetilde{\chi}_M$ is the implied model for the scalar dissipation

$$\widetilde{\chi}_M = 2\Omega_M V_\phi + 2\beta\Gamma_T\frac{\partial \widetilde{\phi}}{\partial x_j}\frac{\partial \widetilde{\phi}}{\partial x_j}. \quad (4.26)$$

The value of β affects the diffusion coefficient, Γ_R, but more importantly (for $\beta > 0$) it adds a contribution to the modeled dissipation, which is β times

the production of V_ϕ. In previous LES-PDF studies using a similar methodology [66, 67, 70], the value of β is simply zero, so this "production" contribution to the modeled dissipation is absent. The "production" contribution to $\widetilde{\chi}_M$ has been used in many previous LES studies (see e.g., [110]), but this is first time that it has been proposed and used in LES-PDF. We refer to the last term in Eq. 4.26 as the *attenuation of variance production* model for (part of) the scalar dissipation, since in Eq. 4.25 it has the overall effect of attenuating the production term by the factor β. Similarly, we refer to Eq. 4.15 as the *attenuated random walk* implementation of this model, since the diffusivity involved, Γ_R, is the turbulent diffusivity attenuated by the factor β.

4.5.2 Numerical accuracy

The computational configuration of the LES-PDF calculations is identical to that of the LES calculations, described in Sec. 4.4.2. The base case calculations use 20 particles per cell, a value of $C_M = 5$, and the standard value of $\beta = 0$. Convergence studies on the number of particles per cell shows little sensitivity compared to the sensitivity observed from the effect of the grid resolution. The numerical error due to the grid resolution is investigated through calculations on grids A–C from Table 4.4.

The radial profiles of the time-averaged mass-weighted mean and RMS statistics from the LES-PDF grid convergence study are shown in Figure 4.24. On the coarse grids, the LES-PDF solution is generally more accurate (compared to the most numerically accurate LES calculation) than that of the corresponding LES calculation, and convergence in most regions of the flow is achieved at

relatively more coarse grids. One exception is the area of the annulus-coflow mixing, near $r/D = 1.5$. The calculations in this region are found to be more sensitive to numerical errors from the velocity and turbulent diffusivity interpolation.

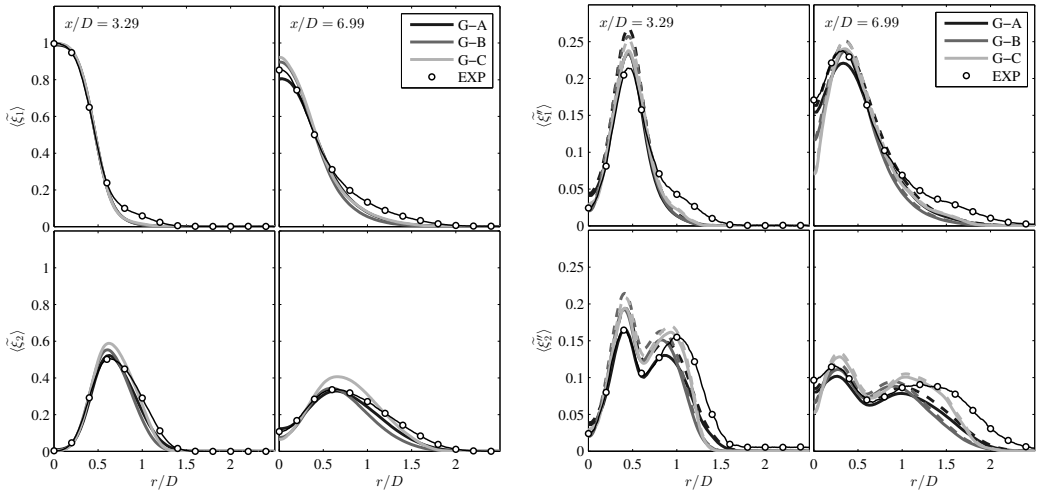

Figure 4.24: Radial profiles of time-averaged mass-weighted mean (a) and RMS (b) mixture fractions in the LES-PDF grid convergence study. Dark line: Grid G-A; Dark gray line: Grid G-B; Light gray line: Grid G-C. Solid lines: resolved statistics; Dashed lines: Total statistics; Circles: experimental data [95].

Joint PDFs are sampled from the particles in the LES-PDF calculations using the same procedure described in Sec. 4.3.2. Figure 4.25 shows the joint PDF at a location of $(x/D, r/D) = (6.99, 0.635)$ for LES-PDF calculations grids A–C. The quantitative agreement with the experimental measurements is very good, and improves as the grid resolution increases. There is a very large improvement in the accuracy compared to the previously discussed RANS-PDF calculations in Sec. 4.3.4.

Also shown in Figure 4.25 is the conditional diffusion from the LES-PDF calculations. The differences between the experimental measurements and the

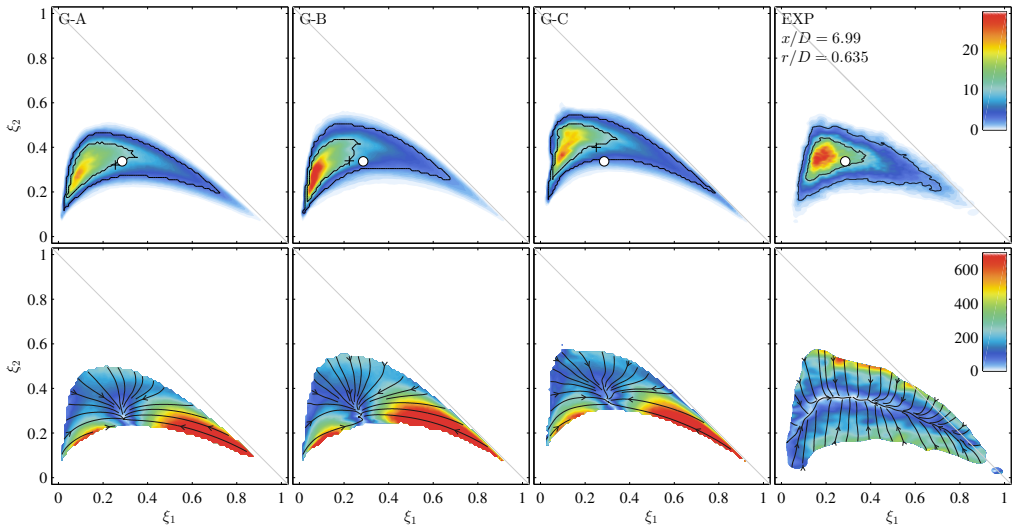

Figure 4.25: Contour plots of the joint PDF of mixture fractions (top) and the magnitude of conditional diffusion (bottom) at $(x/D, r/D) = (6.99, 0.635)$ from the experimental data [95] (right) and LES-PDF calculations on different grids, from left to right: G-A, G-B, and G-C. The circle is the experimental mean, and the plus sign is the mean from the PDF calculation. In the top plots, the two solid lines are isocontours which enclose regions with probability 0.5 and 0.9. In the lower plots, the lines with arrows are streamlines, everywhere parallel to the conditional diffusion vector. Color online only.

calculations can be explained by the observations made in Sec. 4.4.4 and an explanation of the terms in Eq. 4.16. The right-hand side of Eq. 4.16 is composed of two terms: first, the molecular mixing term, and second, the molecular transport term. The resolved conditional diffusion (which corresponds to molecular transport) is small compared to the total conditional diffusion, especially on the coarse grids examined in this section. The contribution of both molecular mixing and molecular transport have been examined in this study; on these grids, molecular transport generally contributes little more than 10% to the total conditional diffusion. As seen in 4.4.4, the addition of the turbulent diffusivity to the calculation of the conditional diffusion results in a departure from the exper-

imentally measured values; similarly here, the addition of the molecular mixing into the calculation of the conditional diffusion shows a difference in form to the measurements. Whether this difference is due to the form of the turbulent diffusivity and the mixing model, the resolution of the measurements, or both is not immediately clear.

4.5.3 Effect of the mixing models

Since the mixing models are the primary source of modeling uncertainty in these calculations, it is imperative to investigate the sensitivity of the calculations to the model constant C_M (which is analogous to, but not equivalent to, the model constant C_ϕ in the RANS-PDF calculations). Most other calculations using this LES-PDF methodology use values of C_M around 4–5 [66, 67], and values of $C_M = \{1, 2, 5, 10\}$ are investigated here.

Figure 4.26 shows radial profiles of the mean and RMS statistics for different values of C_M on Grid-B. There is very little effect of C_M on the mean statistics. This result is expected with the composition PDF method, since C_M only affects the mean through the feedback of the density into the velocity field, and in this flow the variation in density is small. The effect of C_M on the RMS is much stronger; the resolved RMS slightly decreases as C_M increases, and the total RMS decreases significantly as C_M increases. This is the expected behavior since increasing C_M directly increases the dissipation of the modeled variance as shown in Eq. 4.21.

The effect of C_M on the joint PDF is shown in Figure 4.27. As C_M increases, the variance in composition space can clearly be observed to decrease, as the

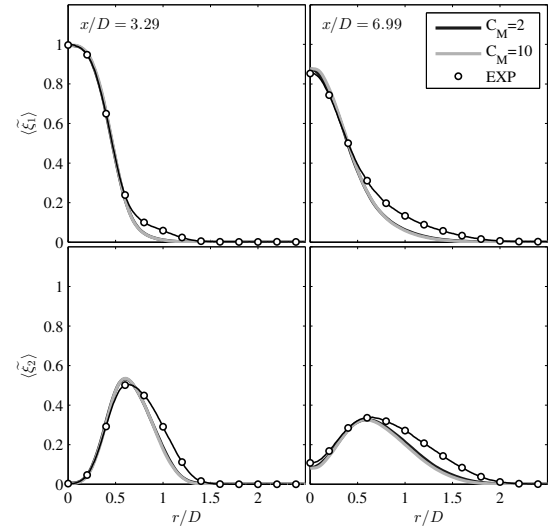

(a)

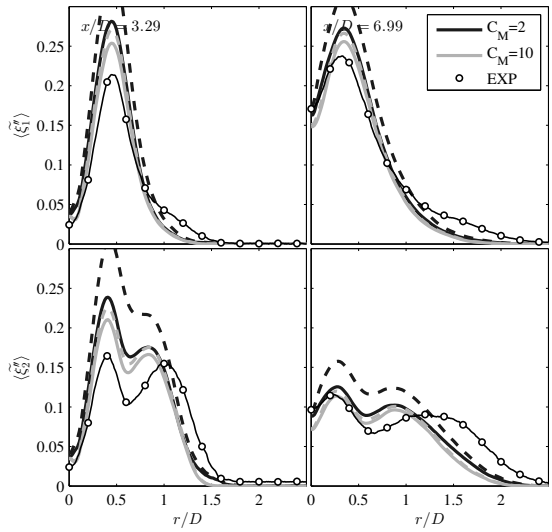

(b)

Figure 4.26: Radial profiles of time-averaged mass-weighted mean (a) and RMS (b) mixture fractions in the LES-PDF calculations for different values of C_M. Dark line: $C_M = 2$; Light line: $C_M = 10$. Solid lines: resolved statistics; Dashed lines: Total statistics; Circles: experimental data [95].

joint PDF comes closer together. In fact, with very small values of C_M, the joint PDF is bimodal at the location shown, which is clearly different from the experimental measurements. The best agreement with the experimentally measured

joint PDF is achieved with C_M of 5 (not shown in Figure 4.27) or 10, and there is indeed a large sensitivity of the joint PDFs to the value of C_M. Increasing C_M directly increases the conditional diffusion, and this is also clear from Figure 4.27.

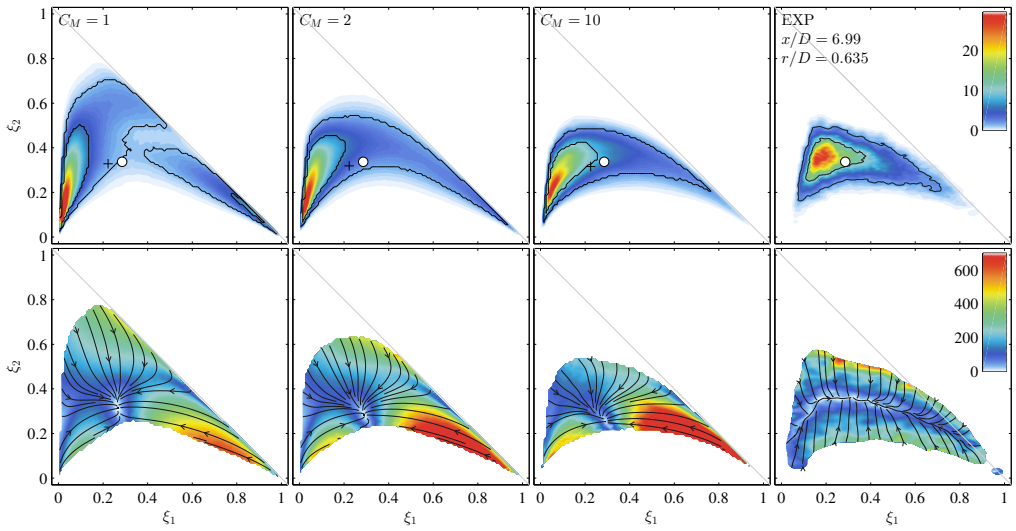

Figure 4.27: Contour plots of the joint PDF of mixture fractions (top) and the magnitude of conditional diffusion (bottom) at $(x/D, r/D) = (6.99, 0.635)$ from the experimental data [95] (right) and LES-PDF calculations on grid G-B using different values of C_M, from left to right: 1, 2, and 10. The circle is the experimental mean, and the plus sign is the mean from the PDF calculation. In the top plots, the two solid lines are isocontours which enclose regions with probability 0.5 and 0.9. In the lower plots, the lines with arrows are streamlines, everywhere parallel to the conditional diffusion vector. Color online only.

In the base case LES-PDF calculations with a value of $\beta = 0$ and the mixing frequency, Ω_M, modeled according to Eq. 4.17, the modeled scalar dissipation rate takes the form

$$\widetilde{\chi}_M = 2C_M \left(\frac{\widetilde{\Gamma} + \Gamma_T}{\Delta^2} \right) V_\phi. \tag{4.27}$$

The modeled scalar dissipation rate in LES-PDF from Eq. 4.27 is consistent with that of the LES (the last term in Eq. 4.8) when $2C_M = C$ and $C_D = 1$. It is noted that in this study, a value of $C_D = 2$ is used, but this difference has very little

affect on the modeled scalar dissipation rate since, in most regions investigated in this flow, the turbulent diffusivity is substantially greater than the molecular diffusivity (typically by a factor of 10 to 100 on the coarse grids). The LES-PDF study of C_M shows that the value of C_M yielding the best agreement with the experimental data is around 5 or 10, which suggests the use of larger values of C than used in the LES study here ($C = 2$ in the base case). This is demonstrated in Figure 4.28, which shows radial profiles of the mean modeled scalar dissipation rate for the LES calculations, and LES-PDF calculations with $C_M = 1$ and $C_M = 5$. As expected, there is close agreement in the modeled scalar dissipation rate among the LES calculations on Grid-A and the LES-PDF calculations on Grid-A with $C_M = 1$, where $2C_M = C$. The agreement between these calculations is very good at $x/D = 6.99$, but slightly worse nearer the exit plane at $x/D = 3.29$, where the error from the time-stepping in LES-PDF is larger. The effect of C_M on the modeled scalar dissipation rate is not entirely obvious from Eq. 4.27. The modeled scalar dissipation rate, $\widetilde{\chi}_M$, is proportional to C_M, but the value of C_M also affects the modeled variance, V_ϕ. As shown in Figure 4.28, as C_M increases, the modeled variance decreases, but not enough to counter the direct effect of C_M on the modeled scalar dissipation rate. The larger dissipation rates observed with $C_M = 5$ yield even greater departures from the relatively small values measured experimentally. The LES-PDF calculations with $C_M = 5$ demonstrate that even larger scalar dissipation rates are necessary in the LES-PDF calculations. As observed in the LES calculations in Figure 4.21, the large, non-physical peak of the scalar dissipation rate at the centerline is present in the LES-PDF calculations as well. This observation gives further reason to work toward improving the numerical and modeling methods in LES.

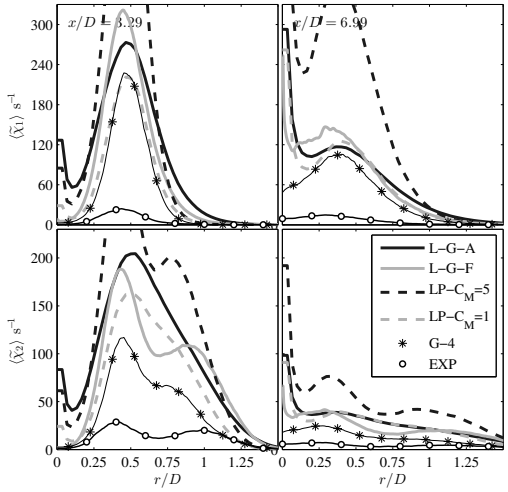

Figure 4.28: Radial profiles of time-averaged mass-weighted mean total modeled scalar dissipation rate for the jet (top) and annulus (bottom) mixture fractions from different calculations. Solid dark line: LES on Grid-A; Solid light line: LES on Grid-F; Dashed dark line: LES-PDF on Grid-A with $C_M = 5$; Dashed light line: LES-PDF on Grid-A with $C_M = 1$; Stars: RANS-PDF; Circles: experimental data [95].

4.5.4 Modeling the molecular and turbulent mixing

The *attenuation of variance production* model as implemented by the *attenuated random walk* described in Sec. 4.5.1 is next assessed in this flow. This part of the work serves only as an introduction to this type of model and implementation, and does not attempt to exhaustively characterize the performance; rather the focus of this part of the current work is to give some general ideas on how to implement the method, examine some possible definitions for value of β, and to compare the results observed here to the experimental measurements for this one flow.

The first value examined is $\beta = 0.2$. The interpretation of this model is that the production of scalar variance from ν_T is counteracted by a dissipation of

20% of the production. A second investigated value for the model constant is one chosen based on the turbulence resolution scale. Here, the choice of $\beta = \widetilde{\nu}/(\nu_T + \widetilde{\nu})$ is used, although this definition is certainly not unique, nor is it necessarily the best. With this value of β, the DNS limit, where the turbulence is fully resolved, yields no production or dissipation due to ν_T. This property is true anyway, as long as ν_T goes to zero at the DNS limit. Where the turbulence resolution scale is large, β tends toward zero. In practice, the values of $\widetilde{\nu}$ are always greater than zero, and the values of ν_T are always finite, so β is always greater than zero; in other words, there is always some amount of dissipation of variance counteracting the production. The logic in using this type of model contains the underlying assumption that where the turbulence is well-resolved, the conditional diffusion is also well-resolved and there is no dissipation or production of the unresolved variance due to ν_T; where the conditional diffusion is poorly-resolved, a small value of β causes the production of the unresolved variance due to ν_T to be large.

Radial profiles of the mean and RMS statistics from LES-PDF calculations with these two models are compared in Figure 4.29. The calculations are conducted on Grid-A with a value of $C_M = 5$. It is clear from Eqs. 4.19 and 4.22–4.23 that the value of β has no direct effect on the mean composition. The small differences that arise in the mean fields, therefore, are due to both the effects of density coupling through the velocity field, and the numerical error in the particle transport. As discussed in Sec. 4.4.3, the LES calculations yield slightly larger values of $\langle\widetilde{\xi}_2\rangle$ than measured experimentally due to the thin-wall modeling assumption. Therefore, the values of $\langle\widetilde{\xi}_2\rangle$ from the two new models are in fact improved from the standard model.

The RMS fields are also affected by the choice of β. The increase in the RMS in the annulus-coflow mixing layer ($1 < r/D$) is attributed mainly to the small changes in the mean in this region. The change in the amount of the RMS which is unresolved (the total minus the resolved) is nearly indiscernible from Figure 4.29. The expected behavior of a positive value of β is to decrease the amount of unresolved scalar fluctuations. Comparing with Figure 4.26, the value of β has a much smaller effect on the unresolved fluctuations than does the value of C_M. For these conditions, the dissipation of the modeled variance is dominated by the molecular mixing term.

4.6 Discussion

As experimental methodologies continue to advance, much more knowledge of the physical processes involved can be brought to light. It is increasingly important to be able to validate these experimental results, as well as to use the experimental results to validate computational models. This work addresses progress in both of these areas. A recently conducted experiment of a turbulent coaxial jet [95] is studied computationally through RANS-PDF, LES, and LES-PDF methodologies, and many detailed statistics from the calculations and experiments are compared.

Since there is little dependence of density feedback in the flow field (especially compared to reacting flows, where the maximum density varies by a factor as large as ten), this flow presents a good test case for the mixing models. Whereas many previous studies of mixing models in RANS-PDF calculations are conducted in reacting flows [8, 9, 46, 79], the work performed here is in an

inert flow; this fact gives an advantage to the comparisons done in this work because any uncertainties associated with modeling the chemistry are removed.

However, when interpreting these results and applying the conclusions to PDF calculations of reacting flows, one must be mindful of the conditions of this flow. In reacting flows, the temperatures are as much as 2000 K larger than the ambient temperature here; furthermore, many species important to ignition (for example, H, OH, and H_2) are substantially lighter than the species measured this flow (C_2H_4 and C_3H_6O). As a consequence of both of these facts, the molecular diffusivities of many species important to chemical reaction can be as much as 10–100 times larger than the molecular diffusivities of the species in this flow. So, it is important to realize that in LES-PDF of reacting flows, the contribution of molecular transport for some important species is much larger than what is observed in this work. LES studies have confirmed that molecular diffusion is indeed important in reacting flows, particularly in the near-field of the flow [109]. Given that most of the uncertainties in comparing the conditional diffusion from the calculations and experiments arises from the relatively large turbulent diffusivity, it is expected that reacting flows would yield less of this type of error; this occurs due a larger portion of the total diffusivity being from the molecular diffusivity, particularly at high temperatures and for light species.

The mean and RMS statistics of the flow field can be calculated with very high accuracy using LES, provided the resolution in the LES is sufficient. For the mean fields, sufficient accuracy is achieved when around 20–40% of the total viscosity is resolved; for the RMS fields, this occurs when around 30–60% of the total viscosity is resolved. For the quantities of scalar dissipation rate

and the conditional diffusion, the LES results provide insight on both the quality of the modeling, and of the interpretation of the experimental results. The LES calculations with resolution even higher than the experimental resolution show that the scalar dissipation rate may not be fully resolved in the experiment, and really ought to be interpreted as a scalar dissipation of the resolved fields. Therefore, when comparing calculations to the experimental measurements, one must keep in the mind the resolution with which both are made. The LES and RANS-PDF modeling of the total scalar dissipation rate suggest a total scalar dissipation rate somewhere between 5–10 times larger than the measure resolved scalar dissipation rates. Nevertheless, one must also take into account the quality of the models used to make these estimates. The fact that that RANS-PDF and LES models for the scalar dissipation rate have as much as 50% variation between them shows that improvements in models for the scalar dissipation rate would be insightful, and that this flow would be a good test for such models.

The LES-PDF calculations yield encouraging results for this new, developing methodology. The excellent agreement with the experimental measurements of the joint PDFs obtained with LES-PDF calculations are one example of such results from this study. When one is interested in higher-order statistics of the composition PDF (for example, in the case of pollutant dispersion, where the probability of a certain pollutant to exceed a certain limit must be quantified), LES-PDF calculations are shown here to be an ideal methodology, as they demonstrate a strong capability to reproduce the observed joint PDF of compositions. Conversely, one must be cautious when using RANS-PDF to make calculations of higher-order statistics, as evident in the comparisons of joint PDFs computed in this work.

The *attenuation of variance production* model in LES-PDF introduced here is valuable because it yields an additional dissipation term in the variance transport equation, which is equal to the production times the factor β. The improvement on the coarse grids is encouraging, though it still needs to be better understood. Since the value of β really has little impact on the mean scalar fields, the results indicate that the improvement is actually caused by reduced numerical error in the particle transport using this method. In many previous LES-PDF studies, total RMS statistics of scalars are not reported; when they are reported, they are often overpredicted [66, 111, 112]. In some cases, improved RMS statistics can be obtained through unreasonably large values of the mixing model constant, C_M [111]. This newly proposed model offers a promising alternative approach to this problem. This work serves only as an introduction to such a model, and more conclusive testing should be done in other flows, the values for β ought to be more thoroughly characterized, and the effects of numerical errors must be better understood.

An important question arising from this work concerns the difference between the conditional diffusion measured experimentally and calculated by LES and LES-PDF. It is observed here that as the LES grid is refined, both the resolved scalar dissipation and resolved conditional diffusion show reasonable agreement with the experimental measurements for similar resolution scales. It is also observed that these statistics are highly dependent on the resolution, and even on the finest LES grid, they show no signs of reaching convergence. A further observation is that the structure of the resolved conditional diffusion in scalar space is relatively similar for all grid sizes, and of a similar form to the structure observed experimentally. It is not until the total conditional diffusion is computed that the structure of the conditional diffusion in scalar space

significantly deviates from the experimentally measured form (as evident from Figures 4.22 and 4.23). Likewise, the LES-PDF results yield a conditional diffusion which is similar to the total conditional diffusion from the LES calculations.

There are two possible reasons for this difference between the experimental and calculated conditional diffusion: (i) the experimental resolution being too low, and (ii) the modeling of the turbulent diffusivity in LES. This could be tested through DNS of this flow, although the Reynolds number, $14,300$ is still somewhat large compared to that of other DNS studies. A second possible way to investigate this is through experiments with a higher imaging resolution, or experiments at a lower Reynolds number, accompanied by DNS study. Through this kind of study, the fully resolved conditional diffusion could be obtained from the DNS and compared to that measured experimentally. The modeling of the turbulent diffusivity is eliminated in this problem, and the effects of the experimental resolution can be explicitly tested by examining the DNS data at the same resolution.

4.7 Conclusions

In summary, this work uses RANS-PDF, LES, and LES-PDF computational methodologies to model a three-stream turbulent coaxial jet studied experimentally in [95]. The major conclusions of this study are as follows:

- RANS-PDF calculations with all mixing models (IEM, MC, and EMST) are capable of yielding mean and RMS fields in good agreement with the experimental measurements; however, the joint PDFs of the two mixture

fractions yielded by each model show a wide variability with each other and with the experimental data.

- The EMST mixing model yields a PDF which lies almost exactly on the slow mixing manifold identified in the experimental work, but entirely lacks the fast manifold. This suggests that the slow mixing manifold exists due to aspects of mixing represented by the model (mixing local in composition space), while the fast manifold is due to physical processes and aspects of mixing which the model does not consider (for example, velocity-conditioned mixing or differential diffusion).
- LES calculations on successively refined grids display excellent convergence toward the experimentally measured mean and RMS fields. The resolution quality of these calculations is carefully assessed. The resolved scalar dissipation rate and resolved conditional diffusion from these calculations are in good agreement with the experimental measurements, but depend strongly on the resolution.
- LES-PDF calculations yield joint PDFs of the mixture fractions in very good agreement with the experiments, much better than any of the RANS-PDF calculations.
- The *attenuation of variance production* model is introduced, implemented through the *attenuated random walk*, and tested in this flow. This model yields an additional dissipation term in the transport equation for scalar variance which counteracts the production caused by the turbulent diffusivity. Results show improved predictions of the mean and RMS fields in LES-PDF on coarse grids, due to reduced numerical error incurred by this model as well as the reduced production of modeled variance.

This work presents a thorough study of a novel multi-stream non-reacting flow using a variety of computational approaches. The behavior of the calculations has been investigated in terms of non-trivial statistics including the scalar dissipation rate and the conditional diffusion. The advances from experimental methodologies in [95] has allowed comparison of these revealing, insightful statistics to actual experimental data, and this work is aimed at using this novel experimental data to assess the quality of the current models and to test new model implementations. Careful work is performed to examine the experimental data of these statistics, and to assess the impact of the resolution at which they are made. The knowledge on multi-scalar mixing can be furthered and models can be refined to predict this physical process with even greater accuracy by (i) working further from the experimental study [95], (ii) utilizing the findings of this study and other detailed comparisons [99], (iii) addressing the remaining questions identified in this work on the role of the turbulent diffusivity on the conditional diffusion, and (iv) examining this process in other flow configurations.

4.8 Acknowledgements

The authors extend their thanks to Prof. Chenning Tong for providing the experimental data and sharing the details of the experimental work. This work was supported in part by NSF Award No. CBET-1033246. This research was made with Government support under and awarded by DoD, Air Force Office of Scientific Research, National Defense Science and Engineering Graduate (NDSEG) Fellowship, 32 CFR 168a.

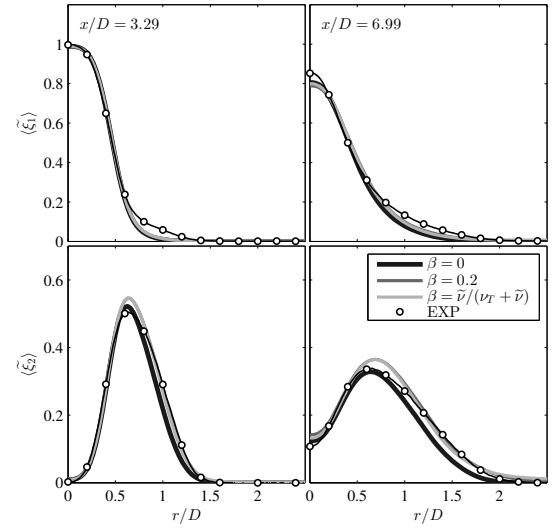

(a)

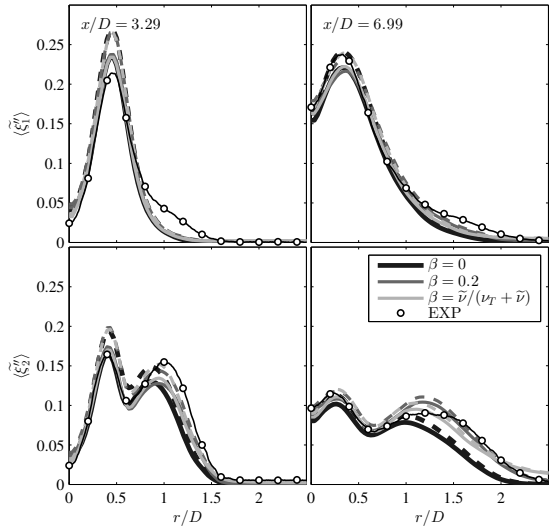

(b)

Figure 4.29: Radial profiles of time-averaged mass-weighted mean (a) and RMS (b) mixture fractions in the LES-PDF calculations for different models for β. Black line: $\beta = 0$; Dark gray line: $\beta = 0.2$; Light gray line: variable β model. Solid lines: resolved statistics; Dashed lines: Total statistics; Circles: experimental data [95].

CHAPTER 5

CONCLUSIONS

In this work, the PDF method is applied to new problems including two challenging jet flows with multiple inflowing streams. These flows have both been developed specifically to test the current computational models. Each flow represents a stringent test especially for PDF methods, in which mixing must be modeled.

In Chapter 2, the first computational study (coincidental with a study done by the experimenting group) of a series of lean, premixed turbulent jet flames is conducted. The main contributions of this study include validating the experimental data, and validating that the calculations do, in fact, overpredict the rate of reaction progress in the flames PM1-150 and PM1-200 (the flames with the largest jet bulk velocity). This work demonstrates that accurate calculations of flames PM1-50 and PM1-100 (the flames with the lowest jet bulk velocity) can be achieved using the standard models. Exploring the nature of combustion occurring in these flames yields the simpler combustion model investigated in 3.2.5.

Chapter 3 builds upon the results from Chapter 2. Four key aspects of the modeling are investigated in greater detail, and the agreement between the new calculations and the experimental data is substantially improved. A simple model for molecular diffusion is tested and implemented into the RANS-PDF calculations; a simplified combustion model based on three scalar variables is tested and implemented; the level of turbulence closure is examined using the recently developed LES-PDF methodology; and lastly, the modeling of molecular diffusion is examined in LES-PDF by considering differential diffusion and

thorough parametric studies of the mixing model parameter, C_M. While many research groups have investigated these flames, the study presented in Chapter 3 is the only one in which accurate mean and RMS profiles of species are obtained 30 jet diameters downstream in flame PM1-150. The work highlights the importance of modeling mixing in premixed combustion, and concurs with the findings of some previous studies of premixed flames, in that larger values of C_M (or a different formulation for mixing) are necessary in these types of calculations. For the accurate prediction of the near-field of the jet, the most important aspects of the modeling are molecular diffusion and the temperature specified at the inlet boundary condition. Farther downstream, the calculations are most affected by the modeling of mixing.

In Chapter 4, a non-reacting turbulent jet with multiple streams is investigated using a variety of approaches. The intricate experimental measurements on which this flow is based present the unique opportunity to compare statistics including the scalar dissipation rate and conditional diffusion. With RANS-PDF modeling, the EMST mixing model is the only mixing model that produces compositions which lie on the slow mixing manifold identified experimentally. Using LES, the resolved scalar dissipation rate are predicted in good agreement with the measurements at the appropriate grid resolution; however, the calculations are found to be very sensitive to the grid resolution even when the resolution is finer than that of the experiment. This observation is highly suggestive that the experimental measurements are under-resolved. The LES-PDF calculations yield much more accurate joint-PDF's of the composition than the RANS-PDF calculations. The *attenuation of variance production* model is proposed here, which yields an additional dissipation term for the scalar variance. This new method demonstrates improved calculations on coarse grids due to both the

additional dissipation of scalar variance, and the smaller numerical error it produces in this configuration. It is valuable to consider because, although this type of modeling has been proposed and used in LES, this is the first time it has been suggested and implemented in LES-PDF methods.

Both RANS and LES based PDF approaches have their own merits (for example, RANS being computationally efficient and accurate in statistically stationary flows of simple geometry, and LES being more accurate in flows of complex geometry and in unsteady flows). Chapter 3 concludes that in this flow geometry, there is limited benefit for using LES-PDF over RANS-PDF for the investigated mean and RMS statistics. But Chapter 4, which considers a flow geometry very similar to that of Chapters 2 and 3, shows that when comparing higher-order statistics (or the entire PDF), LES-PDF yields much more accurate calculations. This work shows that for calculations of flows where higher-order statistics are important (for example, in pollutant dispersion), LES-PDF is a better choice. More work toward the development of mixing models is the most promising way to improve the RANS-PDF calculations for these statistics.

All of the work here shows the PDF method to be a robust way for calculating a variety of turbulent flows. Modeling molecular mixing is by far the single largest contributor of modeling error in the method, and this is demonstrated in all three sections of this work. A first step toward improving the mixing models is the DNS comparison suggested in Sec. 4.6, which would build from the work done here, as well as from the experimental study. Additionally, recently developed mixing models, such as the PSP [75, 77] and IECM [99–102] models show promise as more accurate mixing models in PDF methods. The flows and computational procedures examined in this work provide excellent (albeit

challenging) tests in which these new models ought to be examined.

In order to continue making progress toward a complete computational model for combustion devices, there are a number of remaining computational and modeling challenges. In LES, there is much room for improvement in terms of the current turbulent viscosity models and grid resolution criteria. Modeling of other physical processes, such as liquid atomization and evaporation, soot formation, and acoustics must be improved, as most current models rely strongly upon experimental correlations and tuning constants. Real fuels must also be considered in the models. There is currently much work being done to reduce the complexity of large chemical mechanisms, which is a promising way of being able to include more realistic fuels in these calculations. Lastly, extension of these methodologies to realistic geometries is mainly a computational issue, and as computer power continues to increases, more realistic geometries ought to receive more attention in modeling studies.

Modeling turbulent combustion is an extremely challenging problem, for reasons both computational and modeling-related. The studies presented here apply the PDF method to several very challenging problems to investigate the nature of the physical phenomena, to test the strength of the models in challenging scenarios, and to assess the performance of several new models. This work represents but a small step toward the complete computational model for realistic combustion devices. Building off this work as well as the important contributions of so many others will ultimately lead to the computer-driven design of optimized combustion devices. Through continued progress in combustion research, optimized devices can be developed for a more efficient, cleaner, and safer future.

APPENDIX A

MIXING MODELS

In PDF methods, the effect of molecular diffusion on the composition must be modeled. These mixing models represent one of the largest sources of modeling uncertainty in PDF methods and must be evaluated carefully. In this work, three classical mixing models have been considered, and they are each overviewed here. In the notation used in this section, ϕ_i and ϕ_j refer to the compositions of particles i and j, respectively, while $\phi(t)$ and $\phi(t + \Delta t)$ refer to the compositions of a particle at the beginning and end of a time step, respectively.

A.1 Interaction by Exchange with the Mean (IEM)

In the IEM model [29, 30], particles within a cell relax toward the cell mean value. Specifically, particle i evolves over one time step according to

$$\phi_i(t + \Delta t) = \phi_i(t) - \left(1 - e^{-0.5 C_\phi \omega}\right)\left(\phi_i(t) - \widetilde{\phi}\right), \tag{A.1}$$

where C_ϕ is the mechanical-to-scalar time scale ratio, ω is the turbulence frequency (or $1/\omega$ is the time scale of the turbulence), and $\widetilde{\phi}$ is the mass-weighted cell mean composition.

A.2 Modified Curl (MC)

In the MC mixing model [27, 28], mixing occurs between pairs of particles selected randomly within a cell. In general, the particle selection is weighted toward the mass of each particle. But to illustrate the simpler case with uniform

particle mass, the number of particle pairs selected to mix within one cell at a given time step, N_p, is given by

$$N_p = \left(1.5 C_\phi \omega \Delta t\right) N \tag{A.2}$$

where N is the total number of particles in that cell, C_ϕ is the mechanical-to-scalar time scale ratio, ω is the turbulence frequency, and Δt is the time step. For each selected pair of particles, the composition is moved toward the pair mean composition proportional to a uniform random number, ξ. The composition of the pair of particles i and j is given by

$$\phi_i(t + \Delta t) = (1 - \xi)\,\phi_i(t) + \xi \frac{\phi_i(t) m_i + \phi_j(t) m_j}{m_i + m_j} \tag{A.3}$$

$$\phi_j(t + \Delta t) = (1 - \xi)\,\phi_j(t) + \xi \frac{\phi_i(t) m_i + \phi_j(t) m_j}{m_i + m_j} \tag{A.4}$$

where m_i and m_j are the masses of particles i and j, respectively.

A.3 Euclidean Minimum Spanning Tree (EMST)

A disadvantage of both the IEM and MC models is that mixing does not occur locally in composition space. This can lead to non-physical behavior such as the mixing between products and reactants. The EMST mixing model [19] was developed to remedy this problem by mixing locally in composition space. In this model, an EMST is formed within each cell at each mixing step. This is the minimum length set of edges connecting all the particles to at least one other particle. Particles mix only with their neighbors in the EMST, which causes the mixing to be local in composition space.

BIBLIOGRAPHY

[1] U.S. Energy Information Administration, *International Energy Outlook*, Washington D.C., DOE/EIA-0484 (2011).

[2] S.B. Pope, *PDF methods for turbulent reactive flows*, Prog. Energy Combust. Sci. 11 (1985), pp. 119–192.

[3] J.Y. Chen, W. Kollmann, R.W. Dibble, *PDF modeling of turbulent nonpremixed methane jet flames*, Combust. Sci. Technol. 64 (1989), pp. 315–346.

[4] V. Saxena, S.B. Pope, *PDF simulations of turbulent combustion incorporating detailed chemistry*, Combust. Flame 117 (1999), pp. 340–350.

[5] R.P. Lindstedt, S.A. Louloudi, E.M. Váos, *Joint scalar probability density function modeling of pollutant formation in piloted turbulent jet diffusion flames with comprehensive chemistry*, Proc. Combust. Inst. 28 (2000), pp. 149–156.

[6] J. Xu, S.B. Pope, *PDF calculations of turbulent nonpremixed ames with local extinction*, Combust. Flame 123 (2000), pp. 281–307.

[7] R.P. Lindstedt, S.A. Louloudi, *Joint scalar transported probability density function modeling of turbulent methanol jet diffusion flames*, Proc. Combust. Inst. 29 (2002), pp. 2147–2154.

[8] R.R. Cao, S.B. Pope, A.R. Masri, *Turbulent lifted flames in a vitiated coflow investigated using joint PDF calculations*, Combust. Flame 142 (2005), pp. 438–453.

[9] R.R. Cao, H. Wang, S.B. Pope, *The effect of mixing models in PDF calculations of piloted jet flames*, Proc. Combust. Inst. 31 (2007), pp. 1543–1550.

[10] T. Hůlek, R.P. Lindstedt, *Computations of steady-state and transient premixed turbulent flames using pdf methods*, Combust. Flame 104 (1996), pp. 481–504.

[11] R.P. Lindstedt, E.M. Váos, *Transported PDF modeling of high-Reynolds-number premixed turbulent flames*, Combust. Flame 145 (2006), pp. 495–511.

[12] M.J. Dunn, A.R. Masri, R.W. Bilger, *A new piloted premixed jet burner to study strong finite-rate chemistry effects*, Combust. Flame 151 (2007), pp. 46–60.

[13] M.J. Dunn, A.R. Masri, R.W. Bilger, R.S. Barlow, G.H. Wang, *The compositional structure of highly turbulent piloted premixed flames issuing into a hot coflow*, Proc. Combust. Inst. 32 (2009), pp. 1779–1786.

[14] M.J. Dunn, A.R. Masri, R.W. Bilger, R.S. Barlow, *Finite rate chemistry effects in highly sheared turbulent premixed flames*, Flow Turbulence and Combust. 1386-6184 (2010), pp. 1–28.

[15] G.A. Richards, M.M. McMillian, R.S. Gemmen, W.A. Rogers, S. R. Cully, *Issues for low-emission, fuel-flexible power systems*, Prog. Energy Combust. Sci. 27 (2001), pp. 141–169.

[16] S.B. Pope, *Turbulent Flows*, Cambridge University Press, Cambridge, 2000.

[17] D.C. Haworth, S.B. Pope, *A generalized Langevin model for turbulent flows*, Phys. Fluids 29 (1986), pp. 387–405.

[18] P.R. Van Slooten, Jayesh, S.B. Pope, *Advances in PDF modeling for inhomogeneous turbulent flows*, Phys. Fluids 10 (1998), pp. 246–265.

[19] S. Subramaniam, S.B. Pope, *A mixing model for turbulent reactive ows based on Euclidean minimum spanning trees*, Combust. Flame 115 (1998), pp. 487–514.

[20] S.B. Pope, *Computationally efficient implementation of combustion chemistry using in situ adaptive tabulation*, Combust. Theory Modelling 1 (1997), pp. 41–63.

[21] L. Lu, S.B. Pope, *An improved algorithm for in situ adaptive tabulation*, J. Comp. Phys. 228 (2009), pp. 361–386.

[22] P. Jenny, M. Muradoglu, K. Liu, S.B. Pope, D. A. Caughey, *PDF simulations of a bluff-body stabilized flow*, J. Comp. Phys. 169 (2001), pp. 1–23.

[23] M. Muradoglu, S.B. Pope, D.A. Caughey, *The hybrid method for the PDF equations of turbulent reactive flows: consistency conditions and correction algorithms*, J. Comp. Phys. 172 (2001), pp. 841–878.

[24] M. Muradoglu, K. Liu, S.B. Pope, *PDF modeling of a bluff-body stabilized turbulent flame*, Combust. Flame 132 (2003), pp. 115–137.

[25] J. Xu, S.B. Pope, *Assessment of numerical accuracy of PDF/Monte Carlo methods for turbulent reactive flows*, J. Comp. Phys. 152 (1999), pp. 192–230.

[26] C.J. Sung, C.K. Law, J.Y. Chen, *An augmented reduced mechanism for methane oxidation with comprehensive global parametric validation*, Proc. Combust. Inst. 27 (1998), pp. 295–304.

[27] R.L. Curl, *Dispersed phase mixing-theory and effects in simple reactors*, AICHE J. 9 (1963), pp. 175–181.

[28] J. Janicka, W. Kolbe, W. Kollmann, *Closure of the Transport Equation for the Probability Density Function of Turbulent Scalar Fields*, J. Non-Equilib. Thermodyn. 4 (1979), pp. 47–66.

[29] J. Villermaux, J.C. Devillon, *Representation de la coalescence et de la redispersion des domaines de segregation dans un fluide par un modele d'interaction phenomenologique*, in *Proc. Second Int. Symp. On Chemical Reaction Engineering*, New York, Elsevier, 1972.

[30] C. Dopazo, E.E. O'Brien, *An approach to the autoignition of a turbulent mixture*, Acta Astronaut. 1 (1974), pp. 1239–1266.

[31] V.V. Lissianski, Z. Qin, available at *http://www.me.berkeley.edu/gri-mech*.

[32] F.A. Williams, available at *http://maeweb.ucsd.edu/combustion/cermech*.

[33] H.Wang, X. You, A.V. Joshi, S.G. Davis, A. Laskin, F. Egolfopoulos, and C.K. Law, *USC Mech Version II. High-Temperature Combustion Reaction Model of H_2/CO/C_1-C_4 Compounds*, May 2007, available at *http* : *//ignis.usc.edu/USC$_M$ech$_I$I.htm*.

[34] A. Kazakov, M. Frenklach, available at *http://www.me.berkeley.edu/drm/*.

[35] M.D. Smooke, V. Giovangigli, *Reduced Kinetic Mechanisms and Asymptotic Approximations for Methane-Air Flames*, Lect. Notes Physics 384 (1991), pp. 1–47.

[36] S.M. Correa, *A review of NOx formation under gas-turbine combustion conditions*, Comb. Flame 93 (1993), pp. 41–60.

[37] G. Dixon-Lewis, *Structure of laminar flames*, Proc. Combust. Inst. 23 (1990), pp. 305–324.

[38] R.S. Barlow, G.H. Wang, P. Anselmo-Filho, M.S. Sweeney, S. Hochgrebb,

Application of Raman/Rayleigh/LIF diagnostics in turbulent stratified flames, Proc. Combust. Inst. 32 (2009), pp. 945–953.

[39] M. Stollinger, S. Heinz, *Evaluation of scalar mixing and time scale models in PDF simulations of a turbulent premixed flame*, Combust. Flame 157 (2010), pp. 1671–1685.

[40] R.S. Barlow, J.H. Frank, *Effects of turbulence on species mass fractions in methane-air jet flames*, Proc. Combust. Inst. 27 (1998), pp. 1087–1095.

[41] G. Yu, C.K. Law, C.K. Wu, *Laminar flame speeds of hydrocarbon+air mixtures with hydrogen addition*, Combust. Flame 63 (1986), pp. 339–347.

[42] J.Y. Ren, W. Qin, F.N. Egolfopoulos, T.T. Tsotsis, *Strain-rate effects on hydrogen-enhanced lean premixed combustion*, Combust. Flame 124 (2001), pp. 717–720.

[43] Y. Huang V. Yang, *Dynamics and stability of lean-premixed swirl-stabilized combustion*, Prog. Energy Combust. Sci. 35 (2009), pp. 293–364.

[44] T. Lieuwen, H. Torres, C. Johnson, B.T. Zinn, *A mechanism of combustion instability in lean premixed gas turbine combustors*, J. Eng. Gas Turb. Power 123 (2001), pp. 182–189.

[45] S. Ducruix, T. Schuller, D. Durox, S. Candel, *Combustion dynamics and instabilities: elementary coupling and driving mechanisms*, J. Propul. Power 19 (2003), pp. 722–734.

[46] D.H. Rowinski, S.B. Pope, *PDF calculations of piloted premixed jet flames*, Combust. Theory Model. 15 (2011), pp. 245–266.

[47] H. Wang, S.B. Pope, *Lagrangian investigation of local extinction, re-ignition and auto-ignition in turbulent flames*, Combust. Theory Model. 12 (2008), pp. 857–882.

[48] C. Duwig, K.J. Nogenmyr, C.K. Chan, M.J. Dunn, *Large Eddy Simulations of a piloted lean premix jet flame using finite-rate chemistry*, Combust. Theory Model. 15 (2011), pp. 537–568.

[49] S. Amzin, N. Swaminathan, J.W. Rogerson, *Conditional moment closure for turbulent premixed flames, 23rd International Colloquium on the Dynamics of Explosions and Reactive Systems*, July 24–29, 2011.

[50] V.N. Prasad, K.H. Luo, W.P. Jones, *LES-PDF simulation of a highly sheared turbulent piloted premixed flame*, 7th Mediterranean Combustion Symposium, September 11-15, 2011.

[51] Y. Chen, M. Ihme, *Flame Characterization of a Piloted Premixed Jet Burner*, Spring Technical Meeting of the Central States Section of the Combustion Institute, April 22-24, 2012.

[52] S.B. Pope, *Stochastic Lagrangian models for turbulence*, Annual Rev. Fluid Mech. 26 (1994), pp. 23–63.

[53] R. Cao, H. Wang, S.B. Pope, *The effect of mixing models in PDF calculations of piloted jet flames*, Proc. Combust. Inst. 31 (2007), pp. 1543–1550.

[54] R. Cabra, T. Myhrvold, J.Y. Chen, R.W. Dibble, A.N. Karpetis, R.W. Barlow, *Simultaneous laser Raman-Rayleigh-LIF measurements and numerical modeling results of a lifted turbulent H_2/N_2 jet flame in a vitiated coflow*, Proc. Combust. Inst. 29 (2002), pp. 1881–1888.

[55] A.R. Masri, R. Cao, S.B. Pope, G.M. Goldin, *PDF calculations of turbulent lifted flames of H_2/N_2 fuel issuing into a vitiated co-flow*, Combust. Theory Model. 8 (2004), pp. 1–22.

[56] R.L. Gordon, A.R. Masri, S.B. Pope, G.M. Goldin, *A numerical study of auto-ignition in turbulent lifted flames issuing into a vitiated co-flow*, Combust. Theory Model. 11 (2007), pp. 351–376.

[57] R. McDermott, S.B. Pope, *A particle formulation for treating differential diffusion in filtered density function methods*, J. Comp. Phys. 226 (2007), pp. 947–993.

[58] S. Viswanathan, H. Wang, S.B. Pope, *Numerical implementation of mixing and molecular transport in LES/PDF studies of turbulent reacting flows*, J. Comp. Phys. 230 (2011), pp. 6916–6957.

[59] J.A. Van Oijen, L.P.H. de Goey, *Modelling of premixed laminar flames using flamelet-generated manifolds*, Combust. Sci. Tech. 161 (2000), pp. 113–137.

[60] J.A. Van Oijen, F.A. Lammers, L.P.H. de Goey, *Modeling of complex premixed burner systems by using flamelet-generated manifolds*, Combust. Flame 127 (2001), pp. 2124–2134.

[61] P.J. Colucci, F.A. Jaberi, P. Givi, S.B. Pope, *Filtered density function for large eddy simulation of turbulent reacting flows*, Phys. Fluids 10 (1998), pp. 499–515.

[62] V. Raman, H. Pitsch, R.O. Fox, *Hybrid large-eddy simulation/Lagrangian filtered-density-function approach for simulating turbulent combustion*, Combust. Flame 143 (2005), pp. 56–78.

[63] S. James, J. Zhu, M.S. Anand, *Large eddy simulations of turbulent flames using the filtered density function model*, Proc. Combust. Inst. 31 (2007), pp. 1737–1745.

[64] W.P. Jones, V.N. Prasad, *LES-PDF simulation of a spark ignited turbulent methane jet*, Proc. Combust. Inst. 33 (2011), pp. 1355–1363.

[65] M.B. Nik, S.L. Yilmaz, P. Givi, M.R.H. Sheikhi, S.B. Pope, *Simulation of Sandia Flame D using velocity-scalar filtered density function*, AIAA J. 48 (2010), pp. 1513–1522.

[66] H. Wang, M. Juddoo, S.H. Starner, A.R. Masri, S.B. Pope, *A novel transient turbulent jet flame for studying turbulent combustion*, Proc. Combust. Inst. (2012), (accepted).

[67] Y. Yang, H. Wang, S.B. Pope, J.H. Chen, *Large-eddy simulation/probability density function modeling of a nonpremixed CO/H_2 temporally evolving jet flame*, Proc. Combust. Inst. (2012), (accepted).

[68] S.B. Pope, *Self-conditioned fields for large-eddy simulations of turbulent flows*, J. Fluid Mech. 652 (2010), pp. 139–169.

[69] H. Wang, P.P. Popov, S.B. Pope, *Weak second-order splitting schemes for Lagrangian Monte Carlo particle methods for the composition PDF/FDF transport equations*, J. Comp. Phys. 229 (2010), pp. 1852–1878.

[70] H. Wang, S.B. Pope, *Large eddy simulation/probability density function modeling of a turbulent $CH_4/H_2/N_2$ jet flame*, Proc. Combust. Inst. 33 (2011), pp. 1319–1330.

[71] C.D. Pierce, P. Moin, *Progress-variable approach for large-eddy simulation of non-premixed turbulent combustion*, J. Fluid Mech. 504 (2004), pp. 73–97.

[72] A.W. Vreman, *An eddy-viscosity subgrid-scale model for turbulent shear flow: algebraic theory and applications*, Phys. Fluids 16 (2004), pp. 3670–3681.

[73] P.P. Popov, S. Viswanathan, H. Wang, S.B. Pope, 7th US National Technical Meeting of the Combustion Institute, March, 2011, pp. 1C16.

[74] D.C. Haworth, *Progress in probability density function methods for turbulent reacting flows*, Prog. Energy Combust. Sci. 36 (2010), pp. 168–259.

[75] D.W. Meyer, P. Jenny, *A mixing model for turbulent flows based on parameterized scalar profiles*, Phys. Fluids 18 (2006), pp. 035105.

[76] D.W. Meyer, P. Jenny, *Micromixing models for turbulent flows*, J. Comput. Phys. 228 (2009), pp. 1275–1293.

[77] D.W. Meyer, A new particle interaction mixing model for turbulent dispersion and turbulent reactive flows, Phys. Fluids 22, (2010), pp. 035103.

[78] K. Gkagkas, R.P. Lindstedt. *The impact of reduced chemistry on auto-ignition of H_2 in turbulent flows*, Combust. Theory Model. 13 (2009), pp. 607–643.

[79] K. Liu, S.B. Pope, D.A. Caughey, *Calculations of bluff-body stabilized flames using a joint-PDF model with detailed chemistry*, Combust. Flame 141 (2005), pp. 89–117.

[80] D. Geyer, A. Dreizler, J. Janicka, A.D. Permana, J.Y. Chen, *Finite-rate chemistry effects in turbulent opposed flows: comparison of Raman/Rayleigh measurements and Monte Carlo PDF simulations*, Proc. Combust. Inst. 30 (2005), pp. 711–718.

[81] F. Bisetti, J.Y. Chen, E.R. Hawkes, J.H. Chen, *Probability density function treatment of turbulence/chemistry interactions during the ignition of a temperature-stratified mixture for application to HCCI engine modeling*, Combust. Flame 155 (2008), pp. 571–584.

[82] Z. Warhaft, J.L. Lumley, *An experimental study of the decay of temperature fluctuations in grid-generated turbulence*, J. Fluid Mech. 88 (1978), pp. 659–684.

[83] C. Beguier, I. Dekeyser, B.E. Launder, *Ratio of scalar and velocity dissipation time scales in shear flow turbulence*, Phys. Fluids 21 (1978), pp. 307.

[84] B. Ma, Z. Warhaft, *Some aspects of the thermal mixing layer in grid turbulence*, Phys. Fluids 29 (1986), pp. 3114–3120.

[85] W.J.A. Dahm, P.E. Dimotakis, *Mixing at large Schmidt number in the self-similar far field of turbulent jets*, J. Fluid Mech. 217 (1990), pp. 299–330.

[86] D.R. Dowling, P.E. Dimotakis, *Similarity of concentration field of gas-phase turbulent jets*, J. Fluid Mech. 218 (1990), pp. 109.

[87] Jayesh, Z. Warhaft, *Probability distribution, conditional dissipation, and transport of passive temperature fluctuations in grid-generated turbulence*, Phys. Fluids A4 (1992), pp. 2292–2307.

[88] N.R. Panchapakesan, J.L. Lumley, *Turbulence measurements in axisymmetric jets of air and helium. Part 2. Helium jet*, J. Fluid Mech. 246 (1993), pp. 225.

[89] V. Eswaran, S.B. Pope, *Direct numerical simulations of the turbulent mixing of a passive scalar*, Phys. Fluids 31 (1988), pp. 506–520.

[90] E.E. OBrien, T.L. Jiang, *The conditional dissipation rate of an initially binary scalar in homogeneous turbulence*, Phys. Fluids A3 (1991), pp. 3121–3123.

[91] M.R. Overholt, S.B. Pope, *Direct numerical simulation of a passive scalar with imposed mean gradient in isotropic turbulence*, Phys. Fluids 8 (1996), pp. 3128–3148.

[92] P.K. Yeung, X. Shuyi Xu, K.R. Sreenivasan. *Schmidt number effects on turbulent transport with uniform mean scalar gradient*, Phys. Fluids 14 (2002), pp. 4178–4191.

[93] P.K. Yeung, D.A. Donzis, K.R. Sreenivasan. *High-Reynolds-number simulation of turbulent mixing*, Phys. Fluids 17 (2005), pp. 081703.

[94] C. Tong, Z. Warhaft, *Scalar dispersion and mixing in a jet*, J. Fluid Mech. 292 (1995), pp. 1–38.

[95] J.Cai, M.J. Dinger, W. Li, C.D. Carter, M.D. Ryan, C. Tong, *Experimental study of three-scalar mixing in a turbulent coaxial jet*, J. Fluid Mech. 685 (2011), pp. 495–531.

[96] A. Juneja, S.B. Pope, *A DNS study of turbulent mixing of two passive scalars*, Phys. Fluids 8 (1996), pp. 2161–2184.

[97] P.K. Yeung, *Correlations and conditional statistics in differential diffusion: scalars with uniform mean gradients*, Phys. Fluids 10 (1998), pp. 2621–2635.

[98] B.L. Sawford, S.M. de Bruyn Kops, *Direct numerical simulation and Lagrangian modeling of joint scalar statistics in ternary mixing*, Phys. Fluids 20 (2008), pp. 095106.

[99] D.W. Meyer, R. Deb, *Modeling molecular mixing in a spatially inhomogeneous turbulent flow*, Phys. Fluids 24 (2012), pp. 025103-1–15.

[100] S.B. Pope, *On the relationship between stochastic Lagrangian models of turbulence and second-moment closures*, Phys. Fluids 6 (1994), pp. 973.

[101] R.O. Fox, *On velocity-conditioned scalar mixing in homogeneous turbulence*, Phys. Fluids 8 (1996), pp. 2678.

[102] S.B. Pope, *The vanishing effect of molecular diffusivity on turbulent dispersion: Implications for turbulent mixing and the scalar flux*, J. Fluid Mech. 359 (1998), pp. 299.

[103] P. Domingo, L. Vervisch, D. Veynante, *Large eddy simulation of a lifted jet flame in a vitiated coflow*, Combust. Flame 152 (2008), pp. 415.

[104] K.A. Kemenov, H. Wang, S.B. Pope *Modeling effects of subgrid-scale mixture fraction variance in LES of a piloted diffusion flame*, Combust. Theory and Model. 16 (2012), pp. 611–638.

[105] M. Germano, U. Piomelli, P. Moin, W.H. Cabot, *A dynamic subgrid-scale eddy viscosity model*, Phys. Fluids A3 (1991), pp. 1760.

[106] D.K. Lilly, *A proposed modification of the Germano subgrid-scale closure method*, Phys. Fluids A4 (1992), pp. 633.

[107] H. Pitsch, H. Steiner, *Large-eddy simulation of a turbulent piloted methane/air diffusion flame (Sandia flame D)*, Phys. Fluids 12 (2000), pp. 2541–2554.

[108] M. Ihme, H. Pitsch, *Prediction of extinction and reignition in nonpremixed turbulent flames using a flamelet/progress variable model 2. Application in LES of Sandia flames D and E*, Combust. Flame 155 (2008), pp. 90.

[109] K.A. Kemenov, S.B. Pope, *Molecular diffusion effects in LES of a piloted methane-air flame*, Combust. Flame 158 (2011), pp. 240–254.

[110] H. Pitsch, *Large-eddy simulation of turbulent combustion*, Annu. Rev. Fluid Mech. 38 (2006), pp. 453–482.

[111] D.H. Rowinski, S.B. Pope, *Computational Study of Lean Premixed Turbulent Jet Flames using RANS-PDF and LES-PDF methods*, Combust. Theory Model. (submitted).

[112] M.R.H. Sheikhi, T.G. Drozda, P. Givi, F.A. Jaberi, S.B. Pope, *Large eddy simulation of a turbulent nonpremixed piloted methane jet flame (Sandia Flame D)*, Proc. Combust. Inst. 30 (2005), pp. 549–556.